MEASUREMENTS OF DYNAMIC PROPERTIES OF MATERIALS

Volume III

6061-T6 ALUMINUM
FINAL REPORT

by
D. R. Christman
W. M. Isbell
S. G. Babcock
A. R. McMillan
S. J. Green

Materials and Structures Laboratory
Manufacturing Development, General Motors Corporation
General Motors Technical Center, Warren, Michigan 48090

THIS DOCUMENT CONTAINED
BLANK PAGES THAT HAVE
BEEN DELETED

DOCUMENT CONTROL DATA - R & D

(Security classification of title, body of abstract and indexing annotation must be entered when the overall report is classified)

1. ORIGINATING ACTIVITY (Corporate author) Manufacturing Development, General Motors Corporation, General Motors Technical Center, Warren, Michigan 48093	2a. REPORT SECURITY CLASSIFICATION UNCLASSIFIED 2b. GROUP

3. REPORT TITLE

Final Report Measurements of Dynamic Properties of Materials
Volume III: 6061-T6 Aluminum

4. DESCRIPTIVE NOTES *(Type of report and inclusive dates)*

Final Report (in Six Volumes)

5. AUTHOR(S) *(First name, middle initial, last name)*

Douglas R. Christman, William M. Isbell, Stephen G. Babcock,
Allen R. McMillan, Sidney J. Green

6. REPORT DATE 1971 November	7a. TOTAL NO. OF PAGES 156	7b. NO. OF REFS 98

8a. CONTRACT OR GRANT NO. DASA-01-68-C-0114	9a. ORIGINATOR'S REPORT NUMBER(S)
b. PROJECT NO. NWER XAXA	MSL-70-23, Vol. III
c. Task & Subtask-A106	9b. OTHER REPORT NO(S) (Any other numbers that may be assigned this report)
d. Work Unit-07	DASA-2501-3

10. DISTRIBUTION STATEMENT

Approved for public release; distribution unlimited.

11. SUPPLEMENTARY NOTES	12. SPONSORING MILITARY ACTIVITY Director Defense Nuclear Agency Washington, D. C. 20305

13. ABSTRACT

Results of an experimental study on the dynamic properties of 6061-T6 aluminum are presented. Areas studied included stress-strain-strain rate and reverse loading behavior, elastic constants, equation of state, compressive and release wave characteristics, and spall fracture. The material showed approximately elastic-perfectly plastic behavior under uniaxial stress compression (0.005 to 1000/sec strain rates). Strain-rate sensitivity was very low at 20°C, but increased at temperatures of 150, 204, and 288°C. Longitudinal and shear wave velocities at 20°C were 6.368 and 3.197 mm/μsec, and temperature and pressure dependence was also measured and various elastic constants were calculated. The shock wave equation of state (EOS) up to 200 kbar was determined as $\sigma_H = 1.0 + 140.4 u_p + 37.7 u_p^2$. The EOS was also calculated from the elastic constants and comparisons made with the shock wave EOS. Compressive wave tests showed a well-defined elastic precursor with a steady-state value of $\sim$5 kbar. The yield level from shock wave profile measurements was approximately the same as that determined from uniaxial stress and EOS tests. The impact velocity required for spall fracture was found to increase with decreasing pulse width, and to decrease with increasing temperature.

DD FORM 1473
I NOV 65

C155

14. KEY WORDS	LINK A		LINK B		LINK C	
	ROLE	WT	ROLE	WT	ROLE	WT
Stress-strain-strain rate						
Reverse loading behavior						
Elastic constants						
Equation of state						
Compressive and release wave characteristics						
Spall fracture						

MEASUREMENTS OF DYNAMIC PROPERTIES OF MATERIALS

Volume III

6061-T6 ALUMINUM

FINAL REPORT

" This work was supported by the Defense Nuclear Agency under NWER Subtask AA 106-07"

by

D. R. Christman
W. M. Isbell *
S. G. Babcock
A. R. McMillan
S. J. Green†

Materials and Structures Laboratory
Manufacturing Development, General Motors Corporation
General Motors Technical Center, Warren, Michigan 48090

* Presently with Lawrence Livermore Laboratory, Livermore, California
† Presently with Terra Tek. Inc. 815 East 4th. South, Salt Lake City, Utah 48102

COPY No._____

ABSTRACT

Results of an experimental study on the dynamic properties
of 6061-T6 aluminum are presented. Areas studied included
stress-strain-strain rate and reverse loading behavior, elas-
tic constants, equation of state, compressive and release
wave characteristics, and spall fracture. The material showed
approximately elastic-perfectly plastic behavior under uni-
axial stress compression (0.005 to 1000/sec strain rates).
Strain-rate sensitivity was very low at 20°C, but increased
at temperatures of 150, 204, and 288°C. Longitudinal and
shear wave velocities at 20°C were 6.368 and 3.197 mm/μsec,
and temperature and pressure dependence was also measured and
various elastic constants were calculated. The shock wave
equation of state (EOS) up to 200 kbar was determined as
$\sigma_H = 1.0 + 140.4\ u_p + 37.7\ u_p^2$. The EOS was also calculated
from the elastic constants and comparisons made with the shock
wave EOS. Compressive wave tests showed a well-defined elastic
precursor with a steady-state value of ∿ 5 kbar. The yield
level from shock wave profile measurements was approximately
the same as that determined from uniaxial stress and EOS tests.
The impact velocity required for spall fracture was found to
increase with decreasing pulse width, and to decrease with in-
creasing temperature.

FOREWORD

The prediction of reentry vehicle response to impulsive loading
resulting from energy deposition has been studied extensively
during the last decade. Analytical models and computer routines
have been developed to assess the vulnerability of such vehicles
to the initial loading phase, in which stress waves are gener-
ated and propagated through the structure, and to subsequent
phases, where elastic vibration, plastic deformation and/or frac-
ture may occur.

A Defense Atomic Support Agency (DASA) program was initiated
with the objective of improving computer codes for the predic-
tion of damage induced by X-rays (PREDIX). The PREDIX metals
program has combined the efforts of several contractors under
the direction of DASA. The primary contributions of each con-
tractor can be summarized as follows:

General Motors Corporation--Measurement of material
properties, including stress-strain-strain rate be-
havior, elastic constants, equations of state, shock
wave profiles and spall fracture.

Effects Technology Inc.--Spall fracture tests and
analysis (exploding foil) and underground testing.

KMS Technology Center--Constitutive modeling.

Physics International Company--Energy deposition and
spall fracture studies (electron beam).

Systems, Science and Software--Energy deposition and
front surface phenomena, constitutive modeling and
code development, and underground testing.

TABLE OF CONTENTS

TABLE OF CONTENTS (Continued)

LIST OF ILLUSTRATIONS

LIST OF ILLUSTRATIONS (Continued)

LIST OF ILLUSTRATIONS (Continued)

LIST OF TABLES

LIST OF SYMBOLS

C_B	Bulk Wave Velocity, mm/μsec
C_L	Longitudinal Wave Velocity, mm/μsec
C_S	Shear Wave Velocity, mm/μsec
c_p	Specific Heat, cal/g
G	Shear Modulus, kbar
K	Bulk Modulus, kbar
P_H	Mean Pressure, Hydrostat, kbar
P_S	Mean Pressure, Adiabat, kbar
P_T	Mean Pressure, Isotherm, kbar
T	Temperature, °C
U_S	Shock Wave Velocity, mm/μsec
u_p	Particle Velocity, mm/μsec
v	Specific Volume, cc/g
V_I	Impact Velocity, mm/μsec
X	Target Thickness, mm
X_O	Impactor Thickness, mm
X^S	Adiabatic Modulus, kbar
X^T	Isothermal Modulus, kbar
$X_{OS}^{S'}, X_{OS}^{T'}$	Adiabatic Pressure Derivative @ Zero Pressure $\left(= \left(\frac{\partial X^S}{\partial P} \right) S \big|_{P=0} \right)$
$X_{OT}^{T'}, X_{OT}^{S'}$	Isothermal Pressure Derivative @ Zero Pressure $\left(= \left(\frac{\partial X^T}{\partial P} \right) T \big|_{P=0} \right)$
β	Volume Coefficient of Expansion,/°C $= - \frac{1}{\rho} \left(\frac{\partial \rho}{\partial T} \right)_{P=0}$
γ	Gruneisen Parameter
μ	Compression ($= v_O/v - 1$)
ν	Poisson's Ratio
ρ	Density, g/cc
σ_H	Stress, Hugoniot, kbar

INTRODUCTION

This report is one of a series of six giving results of a study
of dynamic properties of four metals. The principle objectives
of this study were:

- Provide measurements of dynamic properties of
  materials to be used as inputs to model develop-
  ment for shock wave propagation and dynamic
  fracture.

- Provide data to establish accuracy of computer
  code predictions.

- Provide physical interpretation of experimentally
  observed material response to dynamic test condi-
  tions.

The primary areas studied included: (1) Stress-strain-strain
rate behavior in uniaxial stress, including Bauschinger effect;
(2) Elastic constants, including temperature and pressure
dependence; (3) Hugoniot equation of state; (4) Compressive
and release wave profiles, including elastic precursor decay
and wave attenuation; and (5) Spall fracture studies, including
pulse width dependence. The six reports in this series are:

Vol.   I: Summary of Results, DASA 2501-1 (AD712847)
Vol. II: Experimental Methods and Techniques,
            DASA 2501-2
Vol. III: 6061-T6 Aluminum, DASA 2501-3
Vol. IV: Alpha Titanium, DASA 2501-4
Vol.   V: OFHC Copper, DASA 2501-5
Vol. VI: Tantalum, DASA 2501-6

The experimental techniques utilized in this study are reviewed
in Vol. II (DASA 2501-2). Briefly, the principal techniques
applied were:

Stress-strain Studies--A laboratory-type universal
testing machine was used for rates < 0.1/sec, a
medium strain rate machine for rates of 10^{-3}/sec
to 10^2/sec, and a Hopkinson bar device for rates
of about 10^2 to 5×10^3/sec.

Elastic Constants--The pulse superposition method was
used for measuring longitudinal and shear wave velo-
cities as functions of temperature and hydrostatic
pressure.

Equation of State--Gun-launched, flat-plate impact
techniques were used to generate uniaxial strain
conditions. Velocities up to 0.6 mm/µsec were
achieved with 63.5 mm and 102 mm single-stage com-
pressed-gas guns, and velocities of 0.3 to 2 mm/µsec
were achieved with a 64 mm single-stage powder gun.
Hugoniot data were obtained with x-cut quartz gage
and streak camera techniques.

Wave Propagation and Spall Fracture--Flat-plate impact
techniques were also used. Wave profiles were measured
with x-cut quartz gages and a laser velocity interfero-
meter.

A literature search on dynamic properties of materials was
carried out under the PREDIX program and a listing of recent
publications (including abstracts) on dynamic properties of
materials is given in Reference 1.

SECTION I

MATERIAL PROPERTIES

Aluminum has a face-centered-cubic structure and the 6061 type
on which the tests discussed in this report were carried out
is a heat-treatable wrought alloy. This material has nominally
3% alloying constituents (primarily magnesium, silicon and iron)
and results of chemical analysis are given in Table I. The
alloy is solution-heat-treated and precipitation-hardened to
the '-T6' temper, as outlined in Table I. The material was
purchased as sheet and plate stock in thicknesses of 1.6, 3.2,
6.4, 12.7 and 50.8 mm. Although all material was ordered to
the same specifications, there were slight differences in yield
and flow stress behavior for the different thicknesses. Hard-
ness of the various thicknesses was:

Thickness (mm)	Measured R_B	Estimated Bhn (500 kg)
1.6	∿ 50	83
3.2	51	84
6.4	57	91
12.7	59	94
50.8	59	94

All stock thicknesses showed the same degree of grain structur-
ing, although there was some variation in grain size with the
thinner stock having smaller grains. Photomicrographs showing
the grain structure in the 3.2 mm and 12.7 mm stock are shown
in Figure 1.

TABLE I

6061 ALUMINUM CHARACTERISTICS

COMPOSITION (WEIGHT %):

Element	Maximum (Ref. 2)	Measured (12.7 mm Plate)
Silicon	0.80	0.63
Iron	0.70	0.41
Copper	0.40	0.20
Manganese	0.15	0.06
Magnesium	1.20	0.84
Zinc	0.25	0.09
Chromium	0.35	0.20
Titanium	0.15	0.06

PROCESSING (REF. 2):

    A. SOLUTION HEAT TREATMENT, -T4 TEMPER

        1. 970°F for 0.2-1 hours in molten salt.

        2. Quench in cold water with minimum delay.

    B. PRECIPITATION HEAT TREATMENT, -T6 TEMPER

        1. 350°F for 6-10 hours.

        2. Cooling rate unimportant (not too slow).

    C. STRESS-RELIEVED BY STRETCHING, -T651 TEMPER (OPTIONAL)

        1. 1 1/2-3% permanent set after B.

12.7mm Stock

ROLLING
DIRECTION

250μm

3.2mm Stock

ROLLING
DIRECTION

250μm
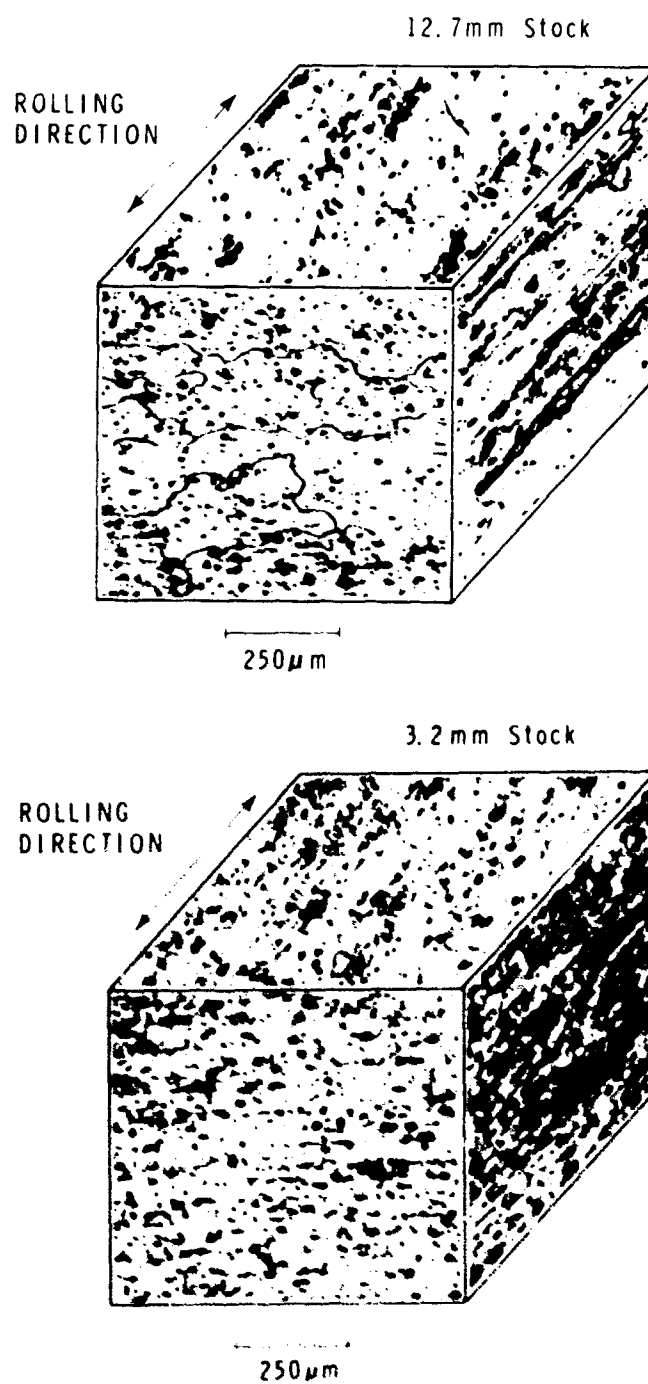
Figure 1   6061-T6 Aluminum, As-Received Material

The average measured density was 2.703 g/cc (0.0976 lb/in^3).
For use in equation of state and energy deposition calculations,
several physical constants were compiled from the literature[3-7]
and are listed below:

Volume coefficient of thermal expansion, β:

$$67.0 \times 10^{-6} + 0.06 \times 10^{-6} \; T \; /°C$$

Specific heat, c_p:

$$0.220 + 0.00015 \times T \; cal/g-°C$$

Solidus temperature: 616°C

Liquidus temperature: 651°C

Boiling temperature: $\sim$ 2450°C

Latent heat of fusion: $\sim$ 93 cal/g

Latent he t of vaporization: $\sim$ 2510 cal/g

(T in °C)

No change in the microstructure of 6061-T6 aluminum was ob-
served for shock stresses up to 30 kbar, i.e., there was
no visual evidence of twinning or grain deformation. Photo-
micrographs of as-received and shocked material are compared
in Figure 2.
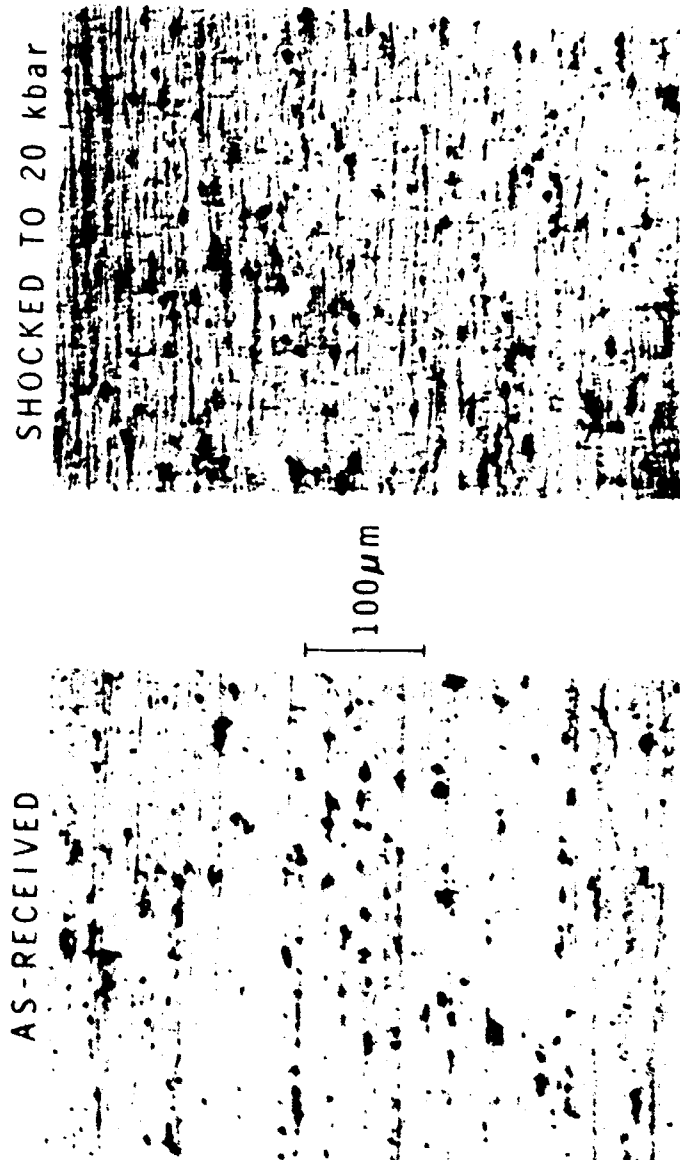
Figure 2   6061-T6 Aluminum, As-Received and
            Shocked Material

SECTION II

STRESS-STRAIN STUDIES

Shock wave and structural response code input requirements in-
clude constitutive equations relating stress to strain, strain
rate and temperature. To obtain these, measurements are made
of uniaxial compressive stress vs. strain at various strain
rates and temperatures. These tests give yield and flow
stress behavior, strain rate sensitivity and work hardening
characteristics. Although it is recognized that heating rate
and time-at-temperature, as well as final temperature, are
important in assessing material properties under short-time
($< 10^{-6}$ sec) energy deposition conditions, most stress-strain
data reported here are for relatively long heating times only.
Bauchinger effect tests were conducted to provide information
on unloading and subsequent yield.

UNIAXIAL STRESS TESTS

Results of compressive stress-strain tests on 6061-T6 are
shown in Figures 3 and 4 for strain rates of 0.005/sec to
10^3/sec and test temperatures of 20° to 288°C, with each
curve the average of several tests. At 20°C, strain rate
sensitivity is negligible (within normal material scatter
and test errors), but increasing the temperature above 150°C
results in an increase in rate sensitivity. Yield stress and
work hardening decrease with increasing temperature.

Figure 3   Compressive Stress vs. Strain, 6061

Figure 4   Compressive Yield Stress vs. Log Strain Rate, 6061

The temperature data in Figures 3 and 4 were obtained for a heating rate of ～ 0.5°C/sec and it has been found that yield and flow stress at elevated temperatures are a function of h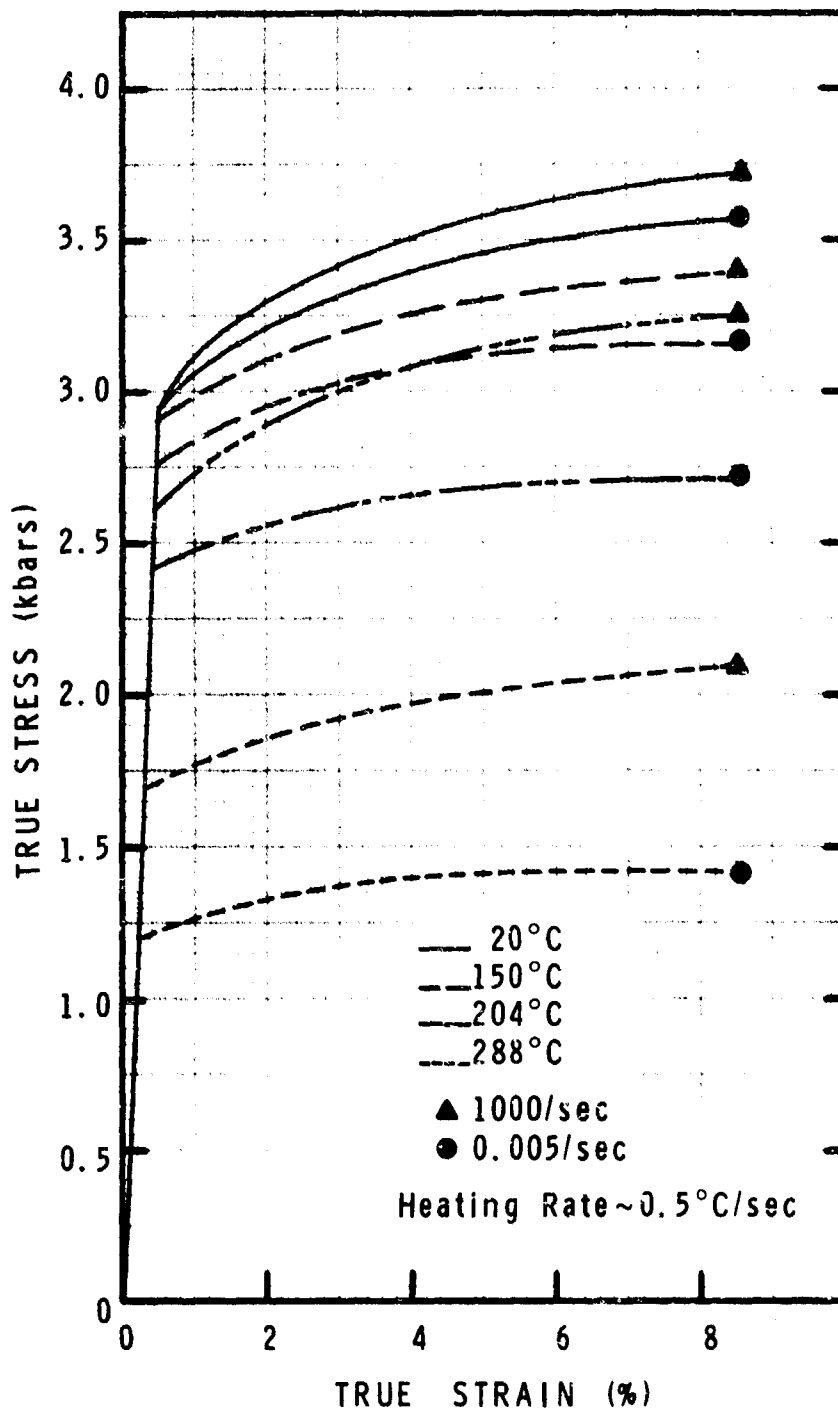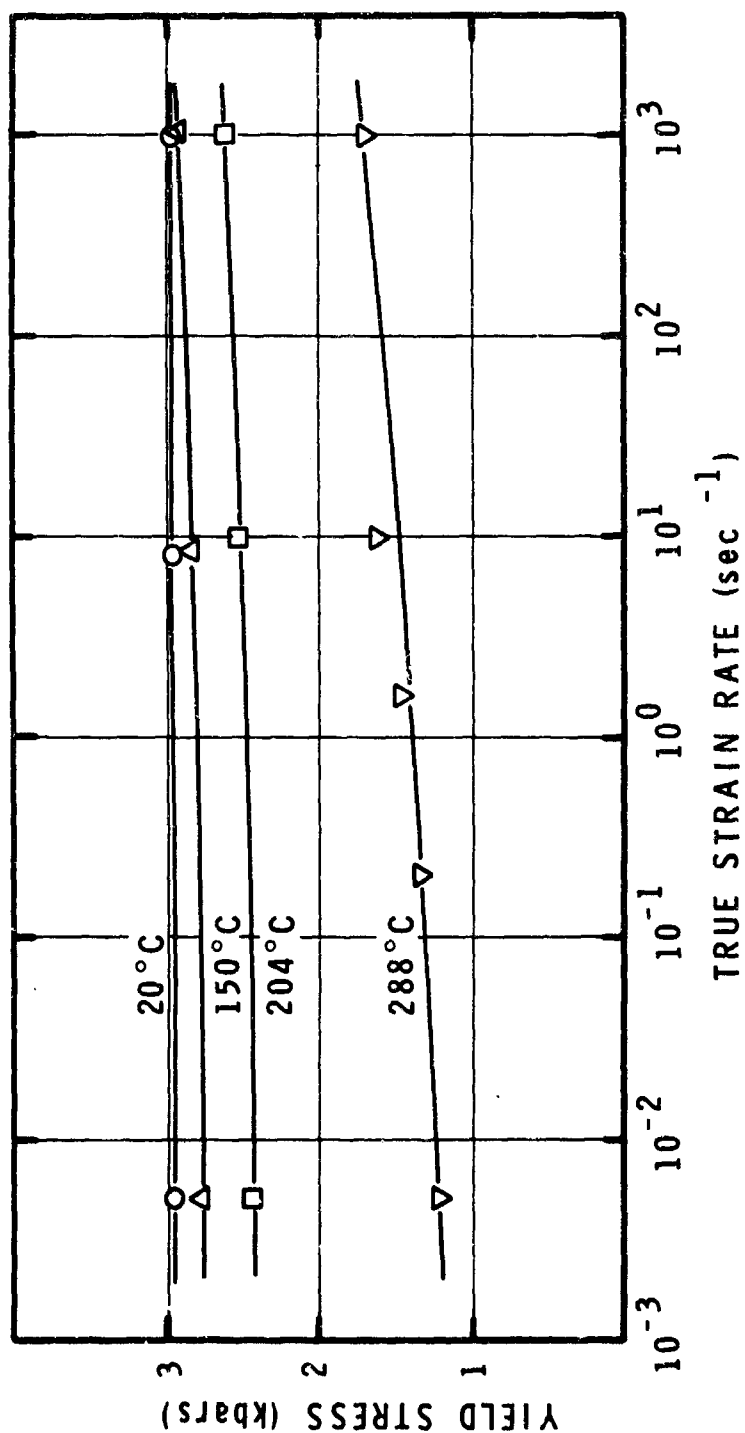eating rate and time-at-temperature.[8] For example, the tensile yield stress in 6061-T651 is shown in Figure 5 as a function of heating rate for two final temperatures. The data indicate that degradation of yield at elevated temperature has three distinct regimes. At high heating rates (> 1°C/sec for 260°C) the yield shows little dependence on heating rate, suggesting an almost instantaneous decrease in yield as temperature increases. At intermediate rates (10^{-4} to 1°C/sec) a time-dependent softening occurs and the yield decreases with decreasing heating rate due to overageing or precipitate coarsening. At low heating rates (< 10^{-4}°C/sec) the yield reaches a constant value. Although the data in Figure 5 are presented in terms of heating rate, the conclusions would be qualitatively the same if discussed as a function of time-at-temperature. All tests were performed at constant strain rate and the observed response may be rate dependent.

There was a slight variation in yield and flow stress for test specimens taken from stock of different thicknesses, as shown in Figure 6. This variation is comparable to that due to scatter from one plate alone and to rate sensitivity at 20°C.

REVERSE LOADING TESTS

The reverse loading behavior or Bauschinger effect* was studied by performing uniaxial tensile stress tests after the material had been prestrained in the opposite (compressive) sense.

---

* The Bauschinger effect can be defined as the reduction in stress at a given strain in the reverse direction compared to that in the original loading direction.

11
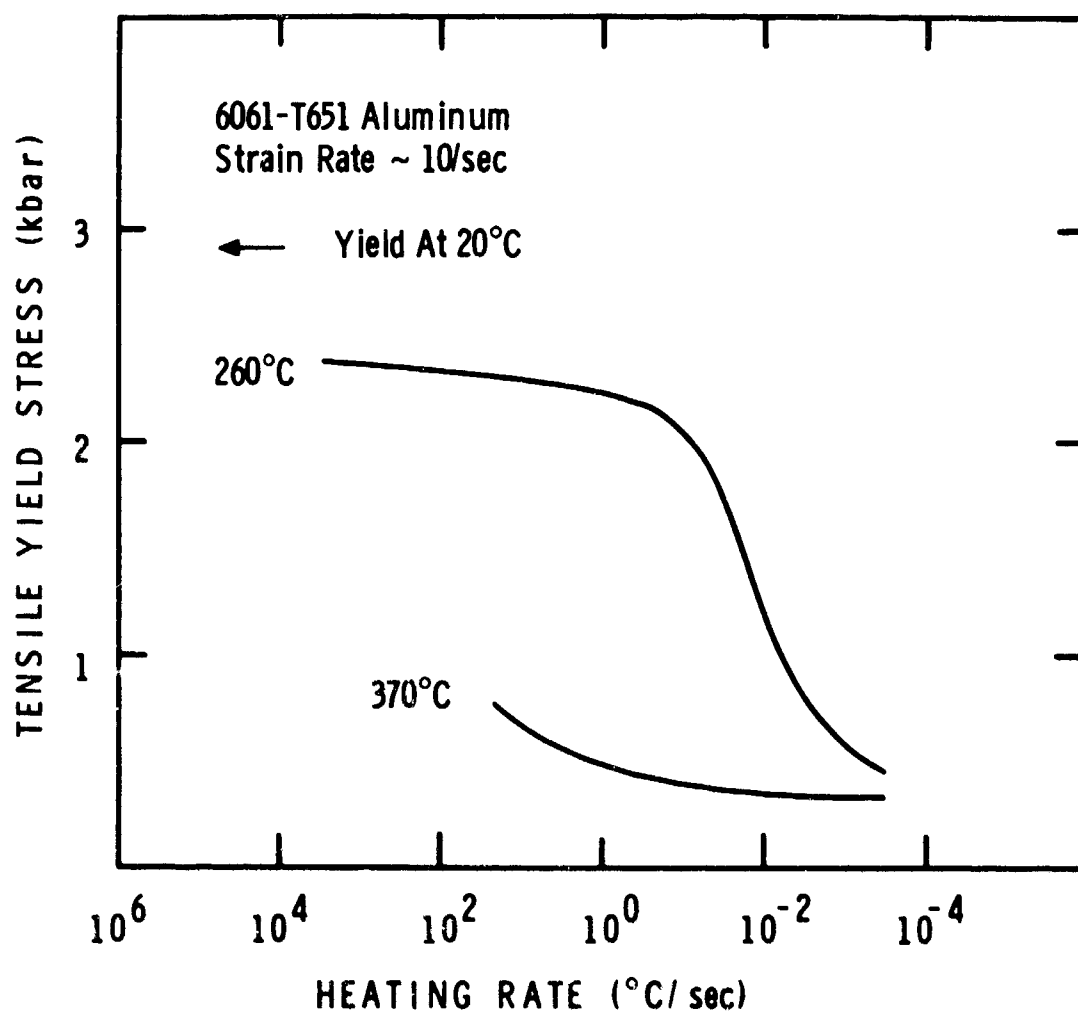
Figure 5   Tensile Yield Stress vs. Log
            Heating Rate, 6061
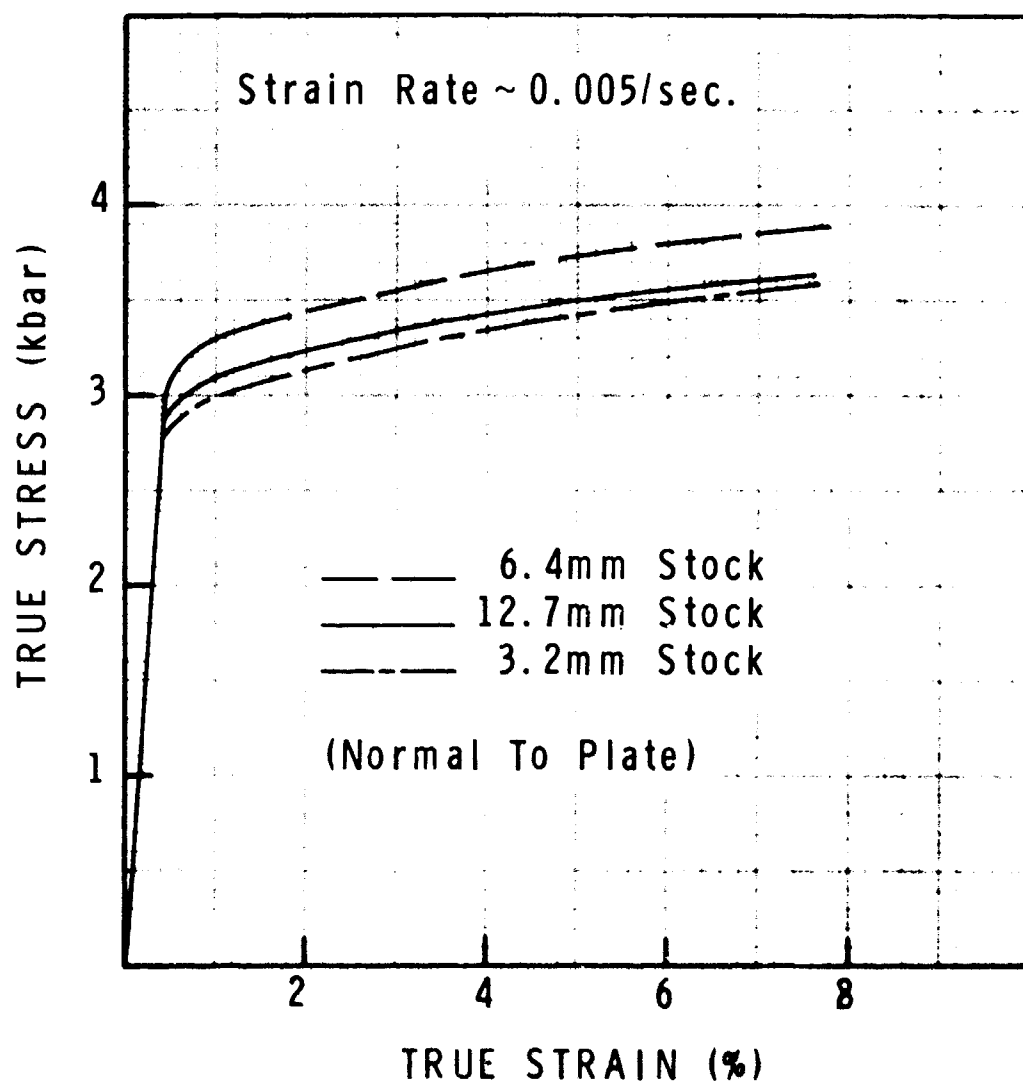
Figure 6   Compressive Stress vs. Strain,
Material Effect, 6061-T6

Specimens were loaded in compression to strains of 0.5 to 3.0%, unloaded to zero stress, and then immediately loaded in tension. The Bauschinger effect can be evaluated in terms of the ratio of yield stress in tension (reload) to the yield stress in compression or to the maximum preload stress. Care must be taken in interpreting data from tests where small (< 0.2%) values of strain are measured. Choosing a definition such as the first deviation from a linear elastic behavior, or stress at a given offset strain, will result in various interpretations of the Bauschinger effect. Reverse loading test results are shown in Figure 7 and the data is cross-plotted in Figure 8 where two definitions of the Bauschinger effect are plotted against plastic prestrain.

Following Milligan, Koo and Davidson[9], a Bauschinger effect factor (BEF) can be defined in two ways:

(1) The ratio of yield stress upon reverse loading to the initial yield stress (see Figure 8 for symbol definition)

$$BEF = \frac{\sigma_C}{\sigma_A}$$

(2) The ratio of yield stress during reloading to the maximum stress upon loading

$$BEF = \frac{\sigma_C}{\sigma_B}$$

This latter definition takes into account strain hardening. All stresses were defined at a 0.1% offset strain. From Figure 8 it appears that the Bauschinger effect factor decreases (Bauschinger effect increases) up to about
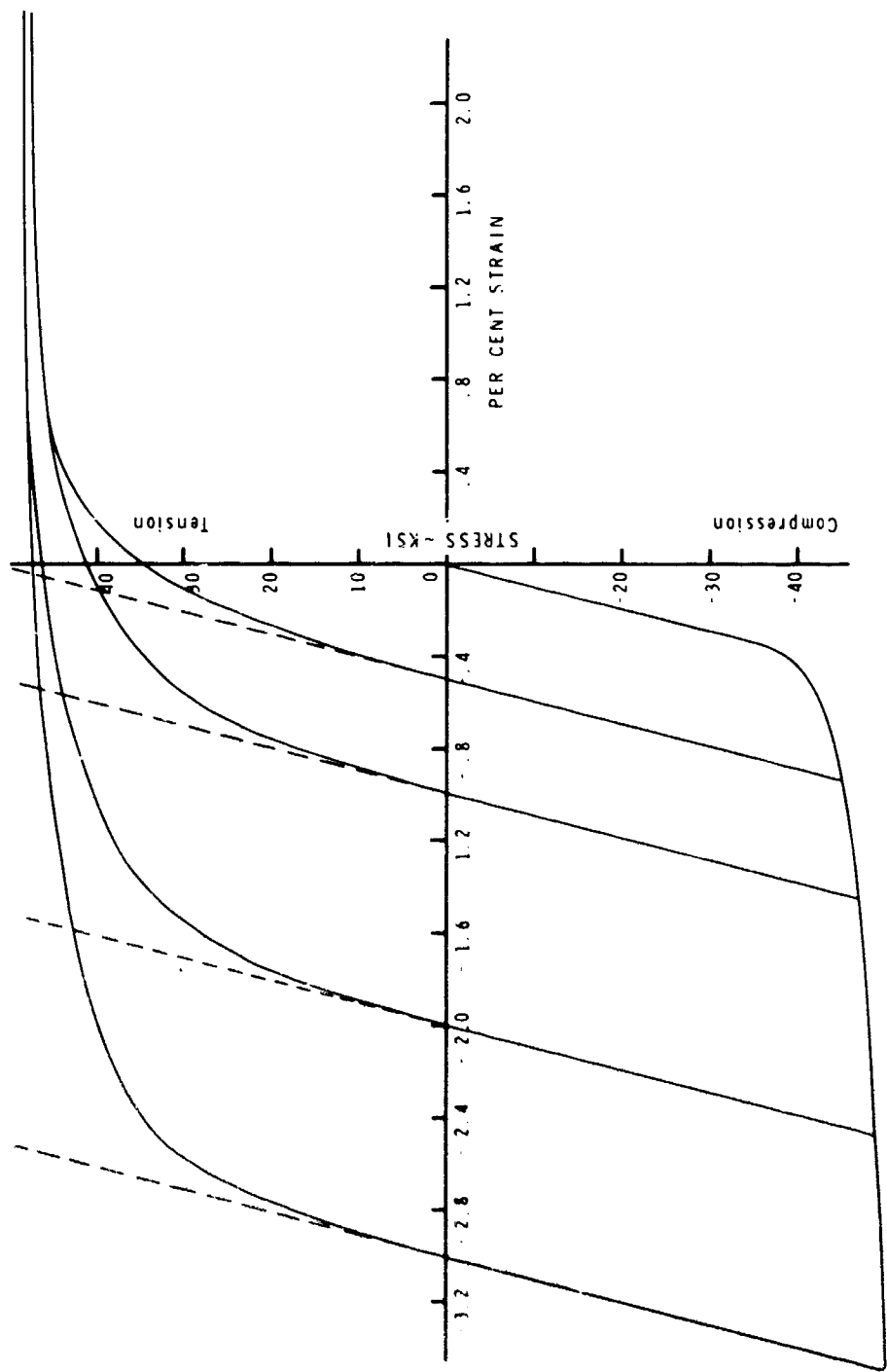
Figure 7   Reverse Loading Behavior, 6061-T6
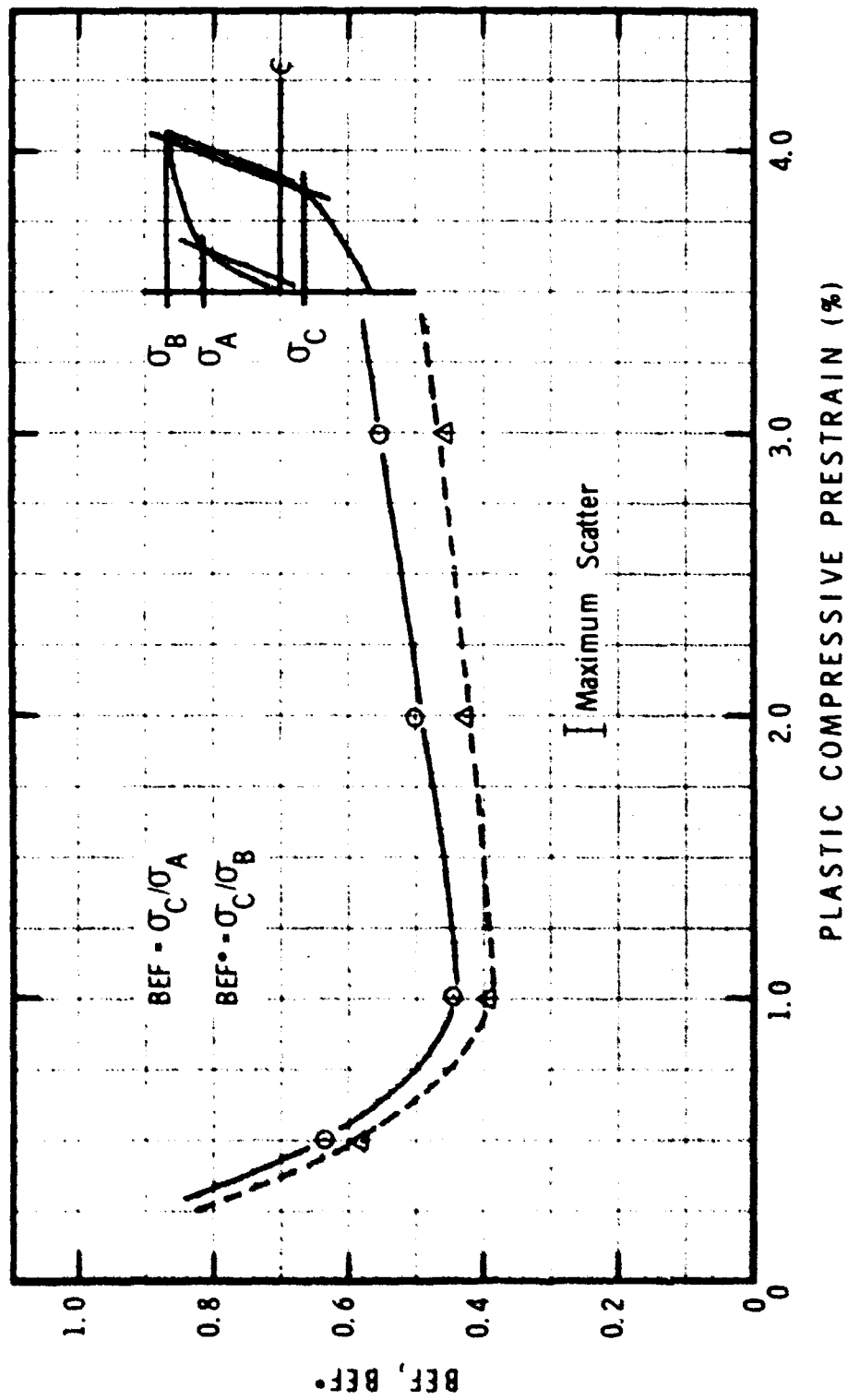
Figure 8   Bauschinger Effect Data, 6061-T6

1.0 - 1.5% plastic strain. Then, with increasing prestrain, the BEF from both definitions appears to increase in magnitude. These results are quantitatively similar to the results on 6061-T6 plate-stock aluminum[10] and modified high-strength steel[9] reported by Milligan, et al., although the preload was in tension rather than compression. The probable cause for the increase in BEF after reaching a minimum at low strains has been attributed to strain-hardening effects.[10,11] Figure 9 shows results from a set of cyclic compression-tension tests on 6061-T6 aluminum. The primary conclusion to be drawn from this data is the type of hardening mechanism for this material. At a strain of approximately 0.5%, kinematic hardening predominates.[8]

BIAXIAL STRESS TESTS

Tubular specimens machined from 6061-T6 bar stock were tested under biaxial stress conditions to determine the yield locus (or surface). A 0.25% strain offset technique in the octahedral shear stress-strain plane was used to determine yield. Results are given in Figure 10 and show that both the von Mises and the Tresca yield theories provide reasonable fits to the data.

(Stress-strain tests of 6061-T6 have been conducted under a number of other programs at General Motors Corporation. The reader is referred to previously published reports and papers for additional details in such areas as uniaxial stress testing[12-14], biaxial stress testing[8,15,16], heating rate effects[8,17,18], and preshocking and prestraining effects[19].)
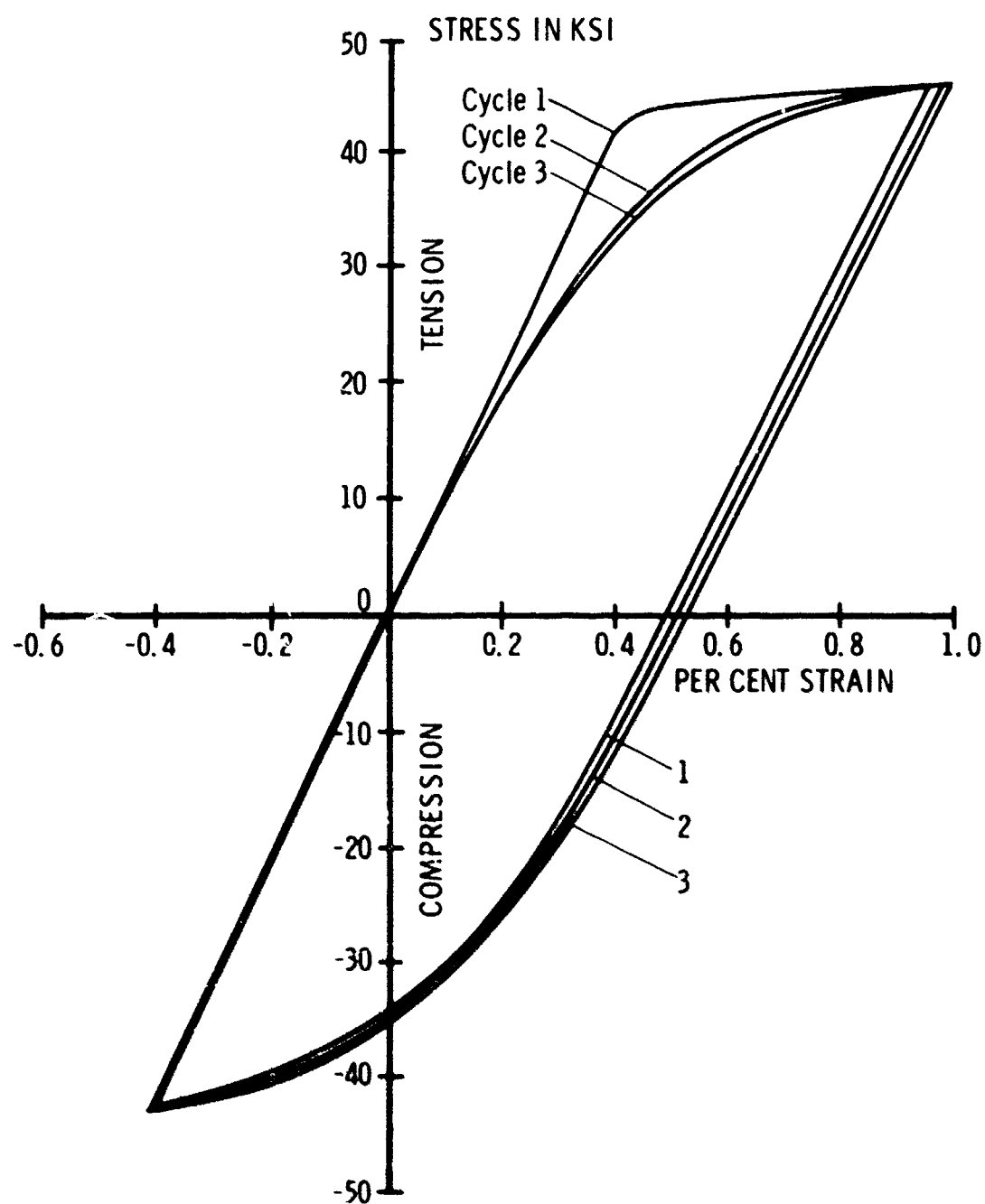
Figure 9   Cyclic Loading Behavior, 6061-T6
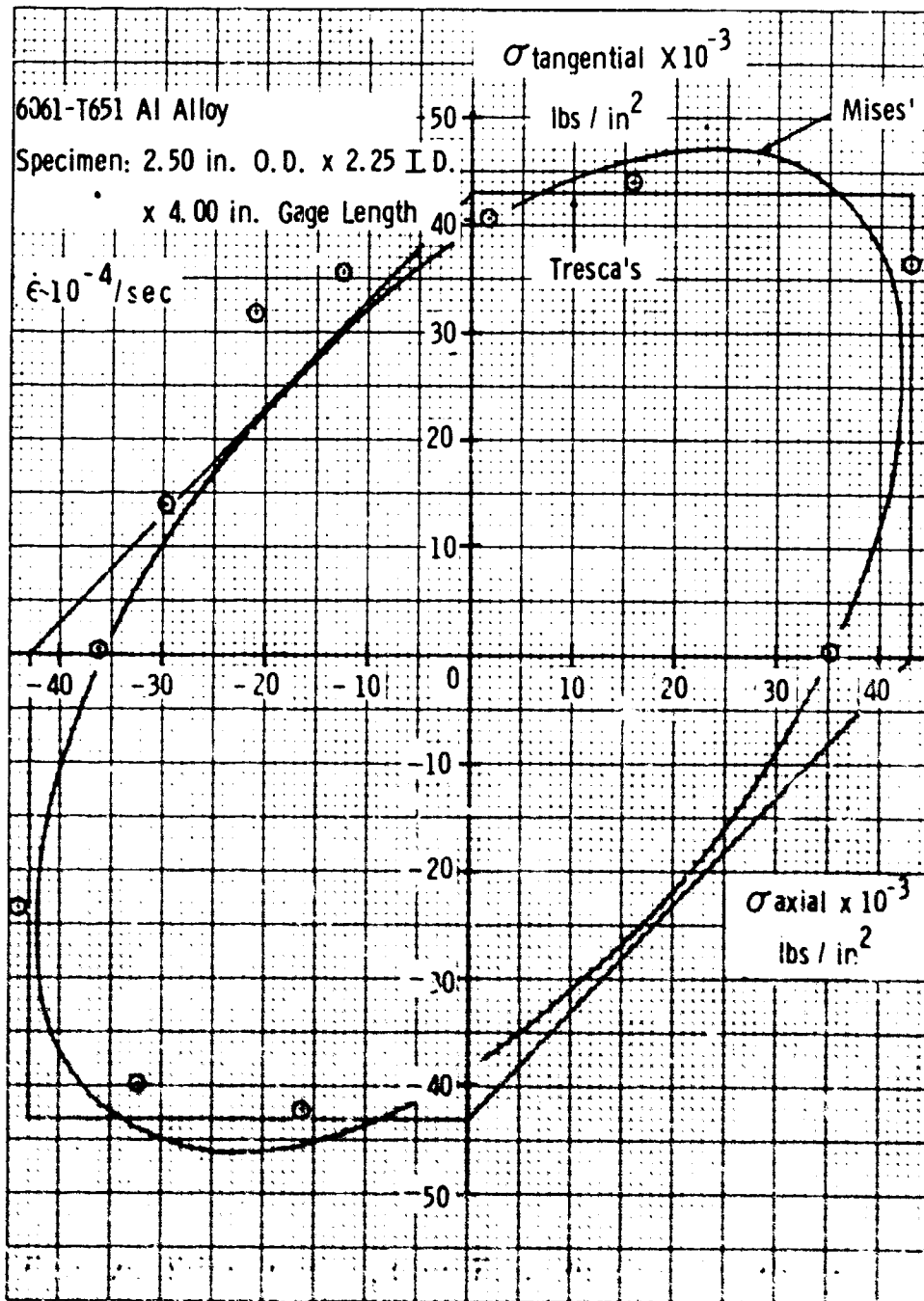
Figure 10   Biaxial Stress Behavior

SECTION III

ELASTIC BEHAVIOR

Measurement of elastic constants provides additional inputs to
the study of material response. The three basic measurements
are density, longitudinal (dilatational) wave velocity and
shear (transverse) wave velocity. Values obtained at standard
temperature and pressure (20°C and atmospheric pressure) estab-
lish the parameters used in first-order (temperature and pres-
sure independent) calculations of material response. Measure-
ments of temperature and pressure dependence permit more exact
calculations to be made and, in particular, lead to prediction
of pressure-compression isotherms, adiabats and hydrostats. If
these measurements are made with sufficient accuracy ($< 0.1\%$),
the calculated pressure-compression behavior can frequently
be extrapolated with reasonable confidence to higher pressures
than covered in the actual measurements.

WAVE VELOCITY MEASUREMENTS

Initial measurements of longitudinal and shear wave velocities
were made at 20°C and atmospheric pressure (i.e., P = 0).
Values obtained were:

$$C_L = 6.368 \pm 0.006 \text{ mm/}\mu\text{sec}$$

$$C_S = 3.197 \pm 0.003 \text{ mm/}\mu\text{sec}$$

Although the accuracy of these measurements is estimated to be about ± 0.1%, it should be noted that C_L and C_S may vary significantly depending on the structural form of the material (i.e., plate, bar, etc.), thermal and mechanical history, and the measurement direction relative to any structural anisotropy. A review of the literature on elastic wave velocities in 6061-T6 gave values of C_L ranging from 6.34 to 6.48 mm/μsec and C_S ranging from 3.04 to 3.26 mm/μsec. [20-23] These variations may be partly due to differences in experimental technique but seem to be primarily the result of differences in composition, structure, texture, and orientation. For example, with 50.8 mm plate stock, C_L normal to the plate was about 0.5% less than C_L in the plane of th plate.

Measurements were also made of the temperature and hydrostatic pressure dependence of the wave velocities. Correction of the data for thermal expansion and hydrostatic compression gave the following:

Temperature Dependence, 0-100°C, P = 0

$$C_L = 6.387 - (0.00093\ T)\ \text{mm/μsec}$$
$$C_S = 3.214 - (0.00084\ T)\ \text{mm/μsec}$$

(T in °C)

Pressure Dependence, 0-9 kbar, T = 20°C

$$C_L = 6.368 + (0.0180\ P) - (0.0001\ P^2)\ \text{mm/μsec}$$
$$C_S = 3.197 + (0.0108\ P) - (0.00005\ P^2)\ \text{mm/μsec}$$

(P in kbar)

For comparison, Asay, et al.[21], reported the temperature dependence of C_L and C_S in 6061-T6 as $C_L = 6.428 - 0.00091 \times T$ and $C_S = 3.199 - 0.00086 \times T$. They also determined the third-order elastic constants at 25°C using a uniaxial stress technique and obtained $\nu_1 = -3010$ kbar, $\nu_2 = -1310$ kbars and $\nu_3 = 1410$ kbar, where ν_1, ν_2, and ν_3 are the third-order Lamé constants for an isotropic elastic body.[24]

ELASTIC CONSTANTS

Assuming the material is isotropic* (C_L and C_S are independent of direction of measurement in a polycrystalline specimen), wave velocity data are used to calculate various elastic constants (see, e.g., Refs. 28-31). At 20°C and zero pressure, the following adiabatic constants were obtained (see Appendix A):

   Bulk wave velocity, $C_B = 5.19$ mm/μsec
   Sound wave velocity, $C_E = 5.22$ mm/μsec
   Rayleigh wave velocity, $C_R = 2.99$ mm/μsec
   Poisson's ratio, $\nu = 0.331$
   Bulk modulus, $K = 728$ kbar
   Shear modulus, $G = 276$ kbar
   Elastic modulus, $E = 735$ kbar
   Lamé's parameter, $\lambda = 544$ kbar

---

* A cubic material is elastically isotropic when $\dfrac{2C_{44}}{C_{11} - C_{12}} = 1$, where C_{44}, C_{11} and C_{12} are elastic stiffness constants. Single-crystal aluminum (99.95%) is only slightly anisotropic with $\dfrac{2C_{44}}{C_{11} - C_{12}} \simeq 1.2$ at 20°C.[25-27]

The bulk and shear moduli are used in the development of the ultrasonic equation of state. They were obtained first as functions of T and P from the following:

$$K = \rho \left(c_L^2 - \frac{4}{3} c_S^2 \right) \tag{1}$$

$$G = \rho c_S^2 \tag{2}$$

This gave:

Temperature dependence, P = 0

$$K = 732 - (0.176\ T)\ \text{kbar}$$

$$G_S = 279 - (0.165\ T)\ \text{kbar}$$

Pressure dependence, T = 20°C

$$K_S = 728 + (4.75\ P) - (0.01\ P^2)\ \text{kbar}$$

$$G_S = 276 + (2.25\ P) - (0.006\ P^2)\ \text{kbar}$$

where the superscript S indicates adiabatic.

Finally, isothermal values of K and G as well as adiabatic and isothermal pressure and temperature derivatives at 20°C and zero pressure were calculated using the equations given in Appendix A. Results are given in Table II. Use of these constants in calculating the isotherm, adiabat and hydrostat is discussed in the section on Ultrasonic Equation of State.

GRUNEISEN PARAMETER

The Gruneisen ratio γ is a parameter originally given by Gruneisen in a solid equation of state relating pressure to

TABLE II

ELASTIC CONSTANTS FOR 6061-T6 ALUMINUM

(P = 0, T = 20°C)

PARAMETER	VALUE
K^S	728 kbar
$(\frac{\partial K^S}{\partial P})_T = K_{0T}^{S'}$	4.75
$(\frac{\partial K^S}{\partial T})_P$	-0.175 kbar/°C
$(\frac{\partial K^S}{\partial P})_S = K_{0S}^{S'}$	4.60
$(\frac{\partial K^S}{\partial T})_S$	5.71 kbar/°C
K^T	700 kbar
$(\frac{\partial K^T}{\partial P})_T = K_{0T}^{T'}$	4.87
$(\frac{\partial K^T}{\partial T})_P$	-0.281 kbar/°C
$(\frac{\partial K^T}{\partial P})_S = K_{0S}^{T'}$	4.64
$(\frac{\partial K^T}{\partial T})_S$	5.75 kbar/°C
$G^S = G^T$	276 kbar
$(\frac{\partial G}{\partial P})_T = G_{0T}'$	2.25
$(\frac{\partial G}{\partial T})_P$	-0.164 kbar/°C
$(\frac{\partial G}{\partial P})_S = G_{0S}'$	2.12
$(\frac{\partial G}{\partial T})_S$	2.64 kbar/°C

volume and energy, $\gamma = V (\partial P/\partial E)_V$ (see, e.g., Refs. 32-34). This parameter can be defined thermodynamically as:

$$\gamma = - \frac{1}{\rho c_p} \left(\frac{\partial V}{\partial T} \right)_P \left(\frac{\partial P}{\partial V} \right)_S = \frac{\beta K^S}{\rho c_p} \tag{3}$$

For an isotropic elastic solid, this can be expressed as

$$\gamma = \frac{\beta}{c_p} \left(c_L^2 - \frac{4}{3} c_S^2 \right) \tag{4}$$

where C_L and C_S are measured under adiabatic conditions.

At $20°C$ and zero pressure this gave

$$\gamma_0 = 1.97$$

The zero-pressure Gruneisen parameter can also be estimated by several other methods, including those of Slater[35], Dugdale and MacDonald[36], Anderson and Dienes[37,38] and Schuele and Smith[37,39]. These methods are discussed in Appendix B.

An estimate of the temperature dependence of the Gruneisen parameter can be obtained by differentiating Equation 3 with respect to temperature. At constant pressure ($P = 0$, $T = 20°C$):

$$\left(\frac{\partial \gamma}{\partial T} \right)_P = \gamma_0 \left[\frac{1}{\beta} \left(\frac{\partial \beta}{\partial T} \right)_P + \frac{1}{K^S} \left(\frac{\partial K^S}{\partial T} \right)_P - \frac{1}{\rho} \left(\frac{\partial \rho}{\partial T} \right)_P \right.$$
$$\left. - \frac{1}{c_p} \left(\frac{\partial c_p}{\partial T} \right)_P \right] = -0.000051/°C \tag{5}$$

The pressure dependence can be estimated by differentiating with respect to pressure (see Appendix C). At constant temperature (T = 20°C, P = 0):

$$\left(\frac{\partial \gamma}{\partial P}\right)_T = \frac{\gamma_0}{K^S}\left[\left(\frac{\partial K^S}{\partial P}\right)_T + \frac{1}{\beta K^T}\left(\frac{\partial K^S}{\partial T}\right)_P - 1 - \gamma - T\left(\frac{\partial \gamma}{\partial T}\right)_P\right] = -0.0051/\text{kbar} \tag{6}$$

Another approach is to assume γ/V constant, which permits $(\partial \gamma/\partial P)_T$ to be estimated directly from the bulk modulus data (see Appendix C). At constant temperature (20°C):

$$\left(\frac{\partial \gamma}{\partial P}\right)_T = \frac{-\gamma_0}{\left(\frac{1}{K_0^T}\right)^{\left(1/K_{0T}^{T'}\right)}\left(K_0^T + K_{0T}^{T'}P\right)^{\left(1+K_{0T}^{T'}\right)/K_{0T}^{T'}}} \tag{7}$$

$$= \frac{-7.57}{(700 + 4.87P)^{1.205}}$$

$$= -0.0028/\text{kbar} @ P = 0$$

$$= -0.0015/\text{kbar} @ P = 100 \text{ kbar}$$

DEBYE TEMPERATURE

The Debye temperature θ is a parameter related to the maximum oscillation frequency a system assumed to be an elastic continuum can support. It is an important parameter in thermal energy calculations and indicates the temperature above which variations due to temperature for some thermodynamic

parameters such as specific heat, thermal expansion and Gruneisen ratio become small. There are a number of methods for calculating the Debye temperature[33,40-42], and one approximation suitable for use with elastic wave velocity data for polycrystalline metals is:

$$\theta = \frac{h}{k} \left(\frac{9N}{4\pi V}\right)^{1/3} \left(\frac{1}{c_L{}^3} + \frac{2}{c_S{}^3}\right)^{-1/3}$$

where h is Planck's constant, k is Boltzmann's constant, N is number of mass points and V is sample volume.

At 20°C, the elastically-determined Debye temperature for 6061-T6 is:

$$\theta = 4.3 \times 10^{-5} \left(\frac{N}{V}\right)^{1/3} \left(\frac{1}{c_L{}^3} + \frac{2}{c_S{}^3}\right)^{-1/3} \tag{8}$$

$$\theta = 420°K$$

for N = 4 (atoms per unit cell), V = $(4.04 \times 10^{-7}$ mm$)^3$ (lattice constant), c_L = 6.368 mm/μsec and c_S = 3.197 mm/μsec.

Sutton[43] reported a Debye temperature for single-crystal aluminum (99.93%) of 407°K at 20°C.
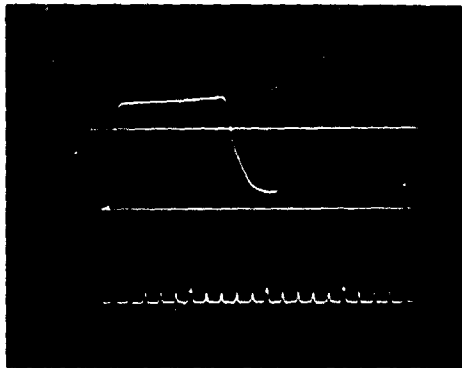
SECTION IV

EQUATION OF STATE

The development of material response models and computational
codes requires extensive data on material behavior under uni-
axial strain conditions, including equation of state, wave
propagation and spall fracture. Most data are used directly
in developing models of material behavior, although independent
check data (attenuated wave shapes and spall wave profiles) are
necessary to determine accuracy of the calculations. This sec-
tion presents the equation of state analysis, and the following
two sections cover wave propagation and spall fracture.

SHOCK WAVE EQUATION OF STATE

The hugoniot equation of state is the locus of equilibrium
states reached after shocking of a material, and data are
usually obtained either as stress-particle velocity points or
as shock velocity-particle velocity points (see, e.g., Refs.
44-49). The shock wave hugoniot data for 6061-T6 presented
in this report were obtained with x-cut quartz gages and op-
tical techniques. Representative quartz gage records for
direct impact and transmitted wave tests are shown in Figure 11.
The buffered direct impact method (tungsten carbide buffer plate
on front of the quartz) permitted stresses up to 65 kbar in the
aluminum while keeping the stress in the quartz at an acceptable
level. The use of quartz gages for transmitted wave tests was
primarily for the study of compressive wave development and
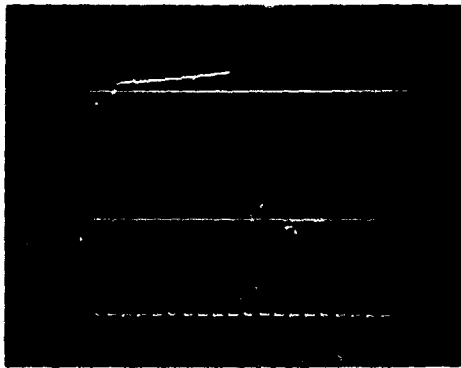elastic precursor decay, and results are discussed in the Wave

DIRECT IMPACT

$AI \rightarrow Q$

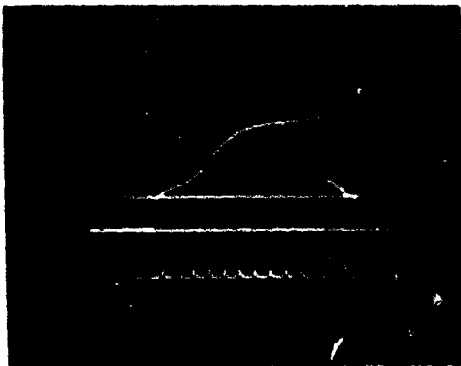$V_I = 0.139 \text{ mm}/\mu s$

$\sigma_H = 10.8 \text{ kbar}$

DIRECT IMPACT, BUFFERED

$AI \rightarrow WC/Q$

$V_I = 0.460 \text{ mm}/\mu s$

$\sigma_H = 64.0 \text{ kbar}$

TRANSMITTED WAVE

$AI \rightarrow AI/Q$

$V_I = 0.173 \text{ mm}/\mu s$

$\sigma_H = 13.4 \text{ kbar}$

Figure 11   Quartz Gage Records

Propagation section. The direct impac' records, which gave a
stress-particle velocity point since the hugoniot of quartz is
known, showed a rise-time of less than 10 nsec. The slight round-
ing at the front of the direct impact records in Figure 11 is due
to impact tilt, and the ramped peak stress region results from
finite-strain effects in the quartz which are corrected in the
data analysis.[50]

Hugoniot data at stresses of 70 to 160 kbar were obtained by
using a steak camera and a target in the form of a two-step
cylinder ("hat" configuration). A schematic of the technique
and a sample record are shown in Figure 12. The two surfaces
of the target are viewed through the camera slit and shock ar-
rival is observed as a change in surface reflectance. The
average shock velocity is obtained from the record, and par-
ticle velocity is assumed to be $1/2\ V_I$ (impact velocity) since
impactor and target are the same material.

The hugoniot may be expressed in several forms. A convenient
form for experimental work is that established by a least-squares
stress and particle velocity, as established by a least-squares
fit to the data in the stress-particle velocity ($\sigma_H - u_p$) plane.
Transformation of the hugoniot into various planes, such as
shock velocity-particle velocity ($U_S - u_p$) and stress-volume
($\sigma_H - v$), is performed by assuming a material model. This was
done by assuming an ideal elastic-plastic wave structure with
equilibrium initial and final states and applying the mass and
momentum conservation equations. This leads to:

$$\sigma_H = \sigma_e + \rho_e\ (U_S - u_e)\ (u_p - u_e) \tag{9}$$

and

$$v = v_o \left(1 - \frac{u_e}{C_L} \right) \left(\frac{U_S - u_p}{U_S - u_e} \right) \qquad (10)$$

where ρ_e and u_e are density and particle
velocity at the elastic limit σ_e.
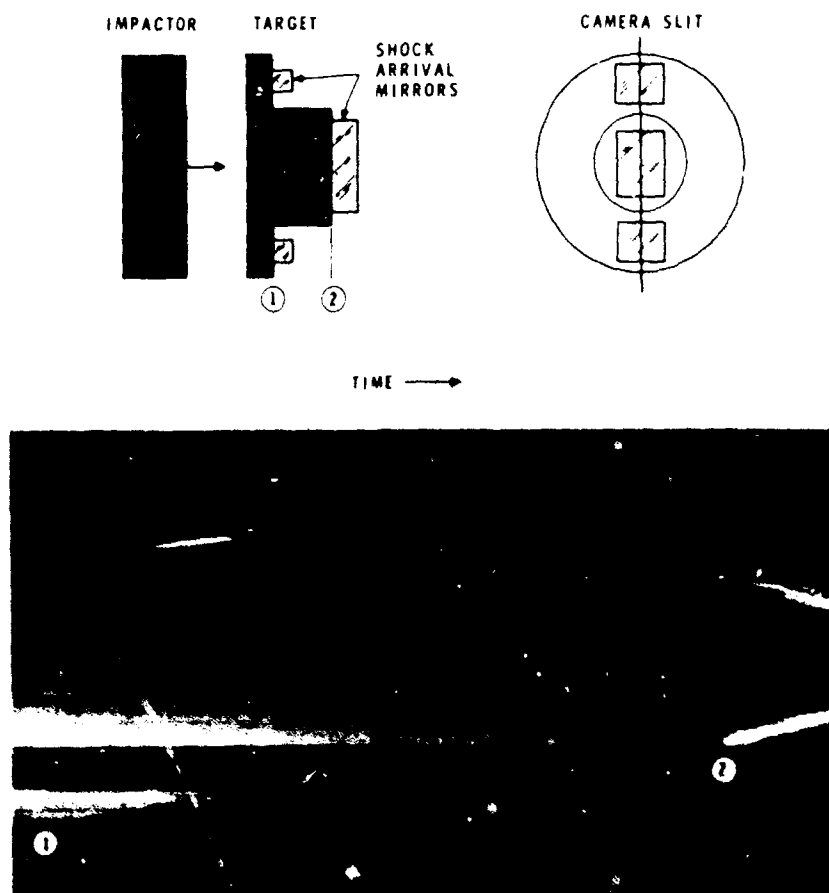
Figure 12   Streak Camera Record, "Hat" Target

Therefore, when either $\sigma_H - u_p$ or $U_S - u_p$ relations are established and σ_e, ρ_e, u_e and C_L are known, σ_H, U_S, u_p and v are uniquely determined. The resulting equations of state for aluminum at 20°C are given in Figures 13, 14 and 15 and are listed below:

$$\sigma_H = 1.0 + 140.4\ u_p + 37.7\ u_p^2 \quad \text{(Std. Error 0.2 kbar)}$$
$$\sigma_H = 2.3 + 708\ \mu + 1607\ \mu^2$$
$$P_H = 708\ \mu + 1607\ \mu^2 \quad \text{(Hydrostat)} \tag{11}$$
$$U_S = 5.24 + 1.40\ u_p$$

where $\mu = (v_o/v)$

These equations of state are based on the measurements indicated by the symbols in Figure 13 and on $\sigma_e = 5.7$ kbar, and are considered to be valid over the stress range of 8 to 200 kbar. Accuracy of the data points is estimated to be ± 2% for σ_H and ± 1% for u_p.

The hydrostat ($P_H-\mu$) was obtained by subtracting the stress-axis intercept value from the $\sigma_H-\mu$ equation. This approach satisfies the requirement that the $P_H-\mu$ function pass through the origin and assumes the deviatoric stress (σ_D) is constant at 2.3 kbar (no strain hardening). Alternative ways of estimating σ_D are discussed in Appendix D.

The low-pressure hugoniot of 6061-T6 was reported previously by Lundergan and Herrmann[51], who used the flat-plate impact technique and free-surface velocity measurements to determine the
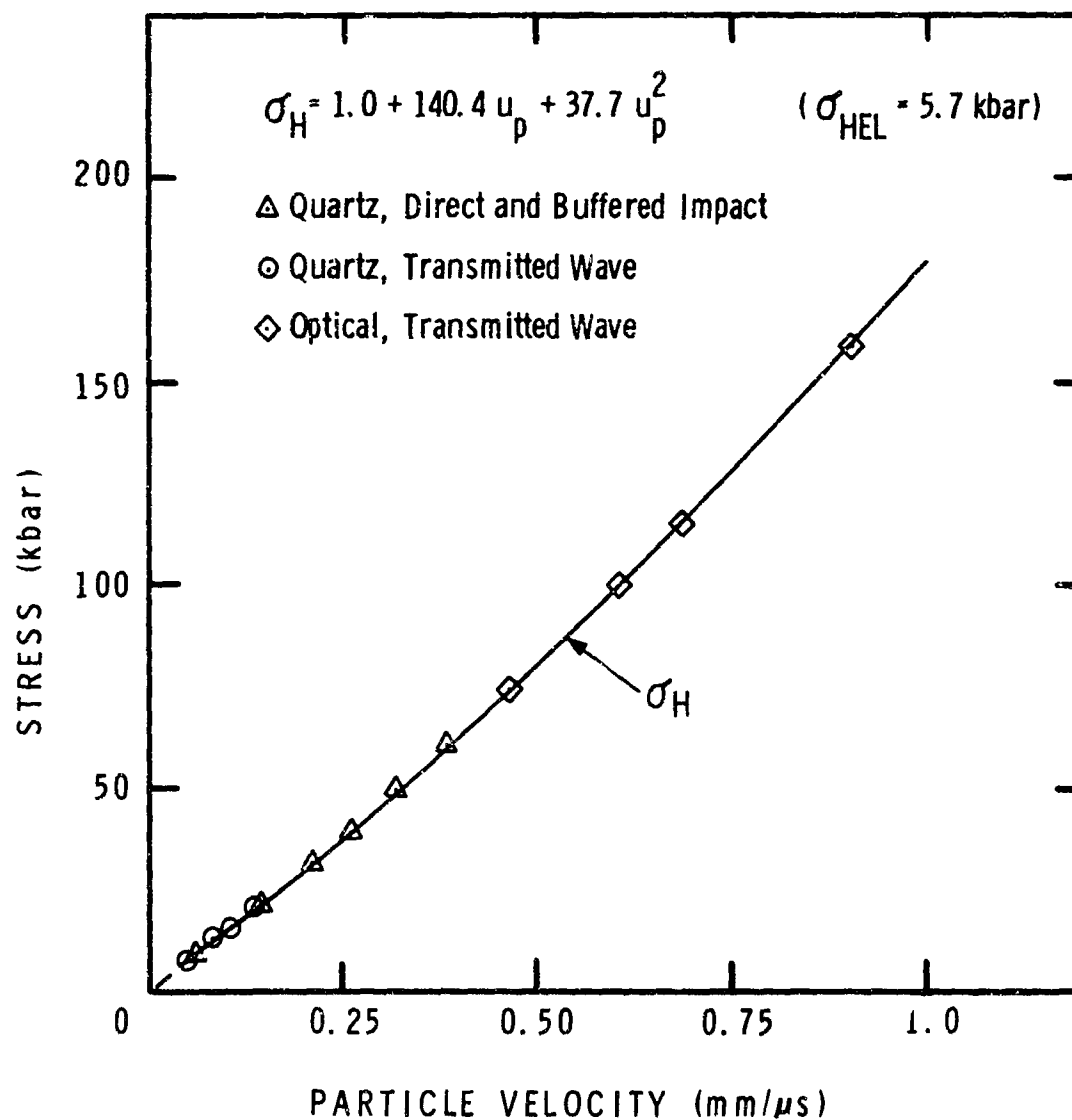
Figure 13   Stress-Particle Velocity
Hugoniot, 6061-T6
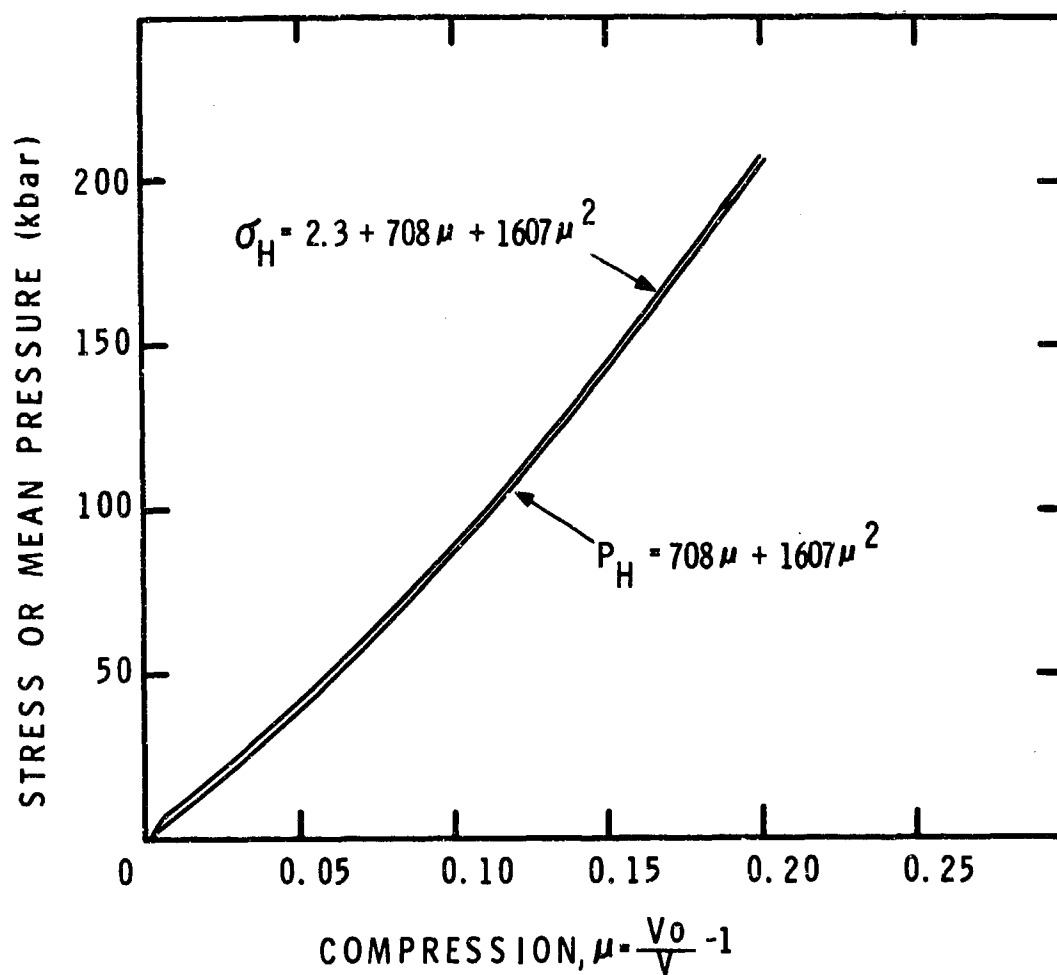
Figure 14   Stress or Mean Pressure-Compression
Hugoniot, 6061-T6
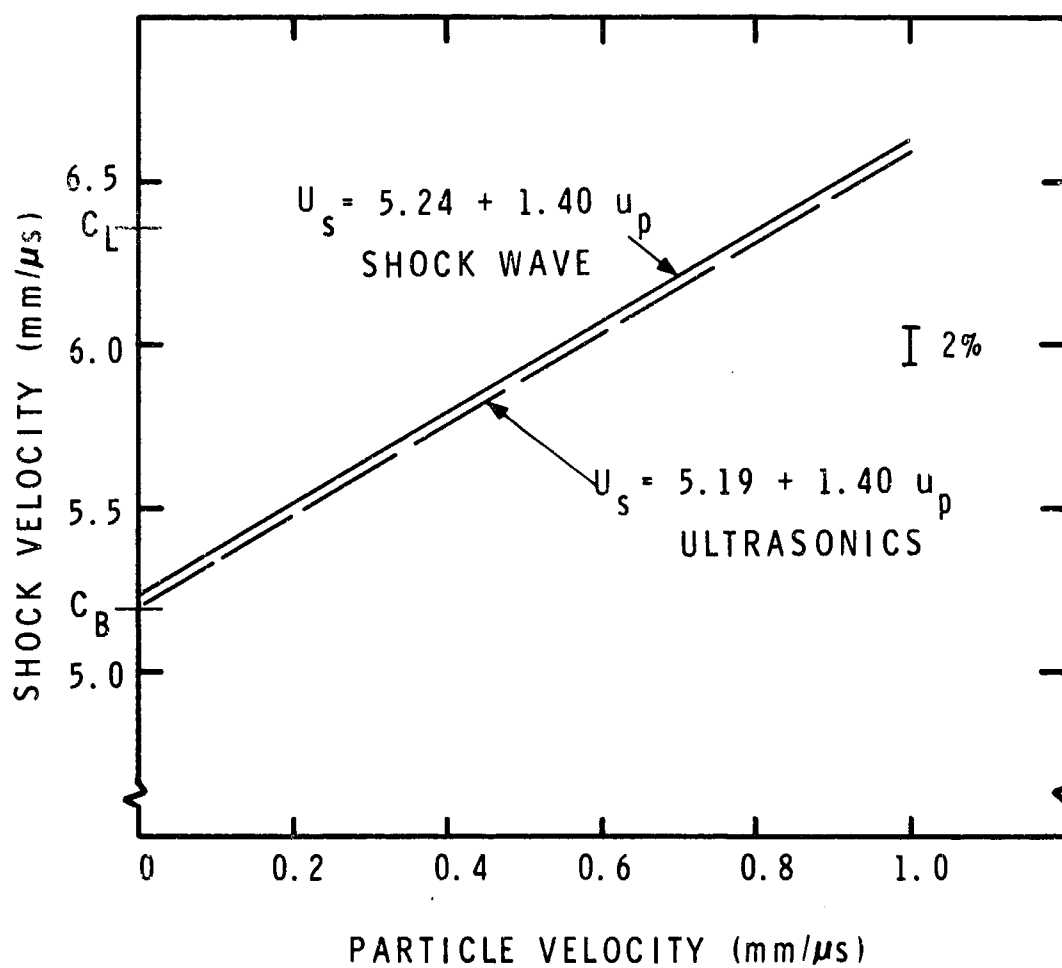
Figure 15   Shock Velocity-Particle Velocity
Hugoniot, 6061-T6

equation of state up to 31 kbars. Results were given as a linear elastic portion (σ_H = 1044 ($\mu/1+\mu$)) up to 6.4 kbar and a linear plastic portion from 6.4 to 31 kbar represented by:

$$\sigma_H = 1.6 + 794 \ (\mu/1+\mu) \tag{12}$$

Comparing this with the hugoniot obtained in the present study gives:

μ	σ_H (Eq. 11) kbar	σ_H (Eq. 12) kbar
0.01	9.5	9.5
0.02	17.1	17.2
0.03	25.0	24.7
0.04	33.2	32.1

The agreement is good over the stress range reported by Lundergan and Herrmann.

The temperature dependence of the hugoniot for 6061[*] was determined using x-cut quartz gages[52]. Measurements were made at 300° and 550°C and results are given in Figure 16. The stress-particle velocity hugoniots are given by:

---

[*] Although the starting material was 6061-T6, the heating times were long enough such that diffusion processes were irreversibly changing material properties and the "-T6" designation is no longer applicable.
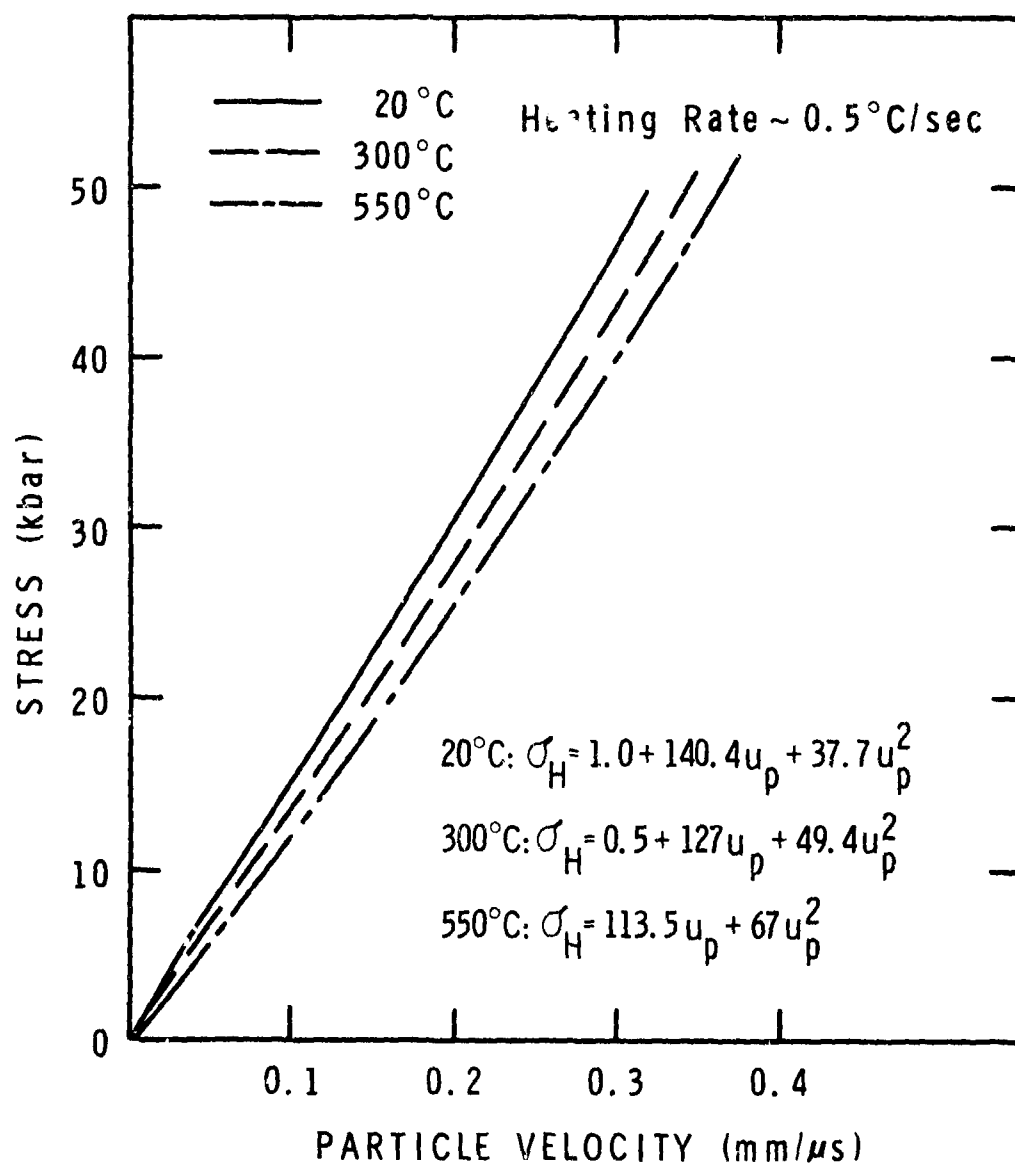
Figure 16   Stress-Particle Velocity Hugoniot,
             Temperature Dependence, 6061

$$300°C: \quad \sigma_H = 0.5 + 127\,u_p + 49.4\,u_p^2$$

(Six data points)

$$550°C: \quad \sigma_H = 113.5\,u_p + 67\,u_p^2$$

(Five data points)

$(\sigma_H < 50 \text{ kbar})$

ULTRASONIC EQUATIONS OF STATE

The equation of state can also be determined from ultrasonics
measurements (see, e.g., Refs. 53-57). The very accurate mea-
surement of elastic wave velocities (and, therefore, bulk modu-
lus) as a function of hydrostatic pressure makes it possible
to directly estimate shock wave compression behavior or to com-
bine ultrasonics data with shock wave data to predict very high
pressure response. Numerous analytical and empirical relations
have been developed for relating pressure, volume and bulk modu-
lus, including those of Birch[58,59], Murnaghan[60] and
Keane[61,62]. The use of these relations is discussed in
Appendix E and results are summarized below:

Birch EOS

$$P_T = 1050 \left[(1+\mu)^{7/3} - (1+\mu)^{5/3} \right] \left[1+0.653 \left\{ (1+\mu)^{2/3} -1 \right\} \right] \quad (13)$$

Murnaghan EOS, Isotherm

$$P_T = 143.7 \left[(1+\mu)^{4.87} -1 \right] \quad (14)$$

38

Murnaghan EOS, Adiabat

$$P_S = 158.3 \left[(1+\mu)^{4.60} - 1 \right] \tag{15}$$

Keane EOS, $K_\infty^{S'} = 1.93$

$$P_S = 896 \left[(1+\mu)^{1.93} - 1 \right] - 1004 \ln(1+\mu) \tag{16}$$

In the above equations, subscripts T and S indicate isothermal and isentropic, respectively.

Duvall gives a correction for the change in entropy across a shock front based on the Murnaghan equation of state:[56,63]

$$P_H = P_S + \frac{\gamma_0 K_0^S}{12} \left(K_{0S}^{S'} + 1 \right) \left(\frac{\mu}{1+\mu} \right)^3$$

$$P_H = P_S + 676 \left(\frac{\mu}{1+\mu} \right)^3 \tag{17}$$

Zel'dovich gives an expression relating P_S and P_T, assuming γ/v is constant:[56,64]

$$P_S = P_T + \beta T_0 K_0^T \left[\exp \left\{ \gamma_0 \left(\frac{\mu}{1+\mu} \right) \right\} - (1+\mu) \right]$$

$$P_S = P_T + 14.2 \left[\exp \left\{ 1.97 \left(\frac{\mu}{1+\mu} \right) \right\} - (1+\mu) \right] \tag{18}$$

The above equations of state are compared to the shock wave
EOS in Table III. The entropy correction based on the Murnaghan
equation has been applied to the Birch and Keane equations as
well. The ultrasonic equations of state show good agreement
with each other and with the shock wave hydrostat, with the
maximum deviation being less than ± 2% up to 115 kbars.

The shock velocity-particle velocity relationship can also be
determined from ultrasonic data. Following the method of
Ruoff[65] one obtains:

$$U_S = C_B + S u_p + A u_p^2 \tag{19}$$

$$\text{where} \quad C_B = \left(\frac{K_0^S}{10 \rho_0} \right)^{1/2}$$

$$S = 1/4 \left(K_{0S}^{S'} + 1 \right) \tag{20}$$

$$A = \frac{1}{24 \, C_B} \left[S \left(7 - K_{0S}^{S'} + 4\gamma_0 \right) + 2 K_0^S K_{0S}^{S''} \right]$$

For aluminum:

$$U_S = 5.19 + 1.40 \, u_p - 0.12 \, u_p^2$$

The u_p^2 coefficient (A = -0.12) was calculated for $K_{0S}^{S''} = -0.02$.
If one assumed $K_{0S}^{S''} = 0$, then A = + 0.12. Since the uncertainty
in $K_{0S}^{S''}$ is $\sim \pm 0.02$, the 'A' coefficient will be taken as zero,
which gives:

$$U_S = 5.19 + 1.40 \, u_p \tag{21}$$

TABLE III

EQUATIONS OF STATE COMPARISON-HYDROSTAT, 6061-T6 ALUMINUM

P_H, HUGONIOT MEAN PRESSURE (kbar)

$\mu = \dfrac{v_0}{v} - 1$	BIRCH EQ. 13	MURNAGHAN EQ. 14	EQ. 15	KEANE EQ. 16	SHOCK WAVE EQ. 11
0.025	18.7	18.7	19.0	18.9	18.7
0.050	39.3	39.3	39.9	39.6	39.4
0.075	61.6	61.9	62.7	61.8	62.1
0.100	86.1	86.8	87.6	85.7	86.9
0.125	112.5	113.9	114.7	111.3	113.6

This is compared with the linear U_S - u_p relation obtained from low-pressure shock wave data in Figure 15.

Vaidya and Kennedy measured the hydrostatic compressibility of 6061-T6 aluminum up to 45 kbar.[66] Results were given as:

$$- \frac{\Delta V}{V_o} = \frac{\mu}{1+\mu} = 1.2281 \times 10^{-3} P_T - 8.793 \times 10^{-6} P_T^2 \\ + 0.10266 \times 10^{-6} P_T^3 \qquad (22)$$

Comparing this with the shock wave and ultrasonic results presented in this report gives:

μ	P_T(Eq. 11)* kbar	P_T(Eq. 14) kbar	P_T(Eq. 22) kbar
0.0125	8.9	9.0	10.8
0.0250	18.4	18.4	22.5
0.0375	28.2	28.2	34.5
0.0500	38.6	38.5	45.7

* Corrected for isothermal conditions.

The hydrostatic data of Vaidya and Kennedy are $\sim$ 20% above (P_T - μ plane) the shock wave and ultrasonic data. The reason for this large difference is not known.

YIELD BEHAVIOR

A complete description of the low-pressure equation of state requires consideration of yield behavior or the hugoniot elastic limit. Values of compressive yield were obtained by three independent methods.

A. Uniaxial Stress

The yield level was determined in uniaxial stress
(σ_σ) as a function of strain rate and then con-
verted to uniaxial strain using:

$$\sigma_e = \sigma_\sigma \left(\frac{1-\nu}{1-2\nu} \right) \qquad (23)$$

Strain Rate sec^{-1}	σ_e kbar
10^3	5.8
10^{-3}	5.7

B. Wave Profiles

The elastic precursor level was measured as a function
of propagation distance using quartz gages. These
profiles are discussed in the section on Wave Pro-
pagation.

Propagation Distance mm	(12.7 mm Stock) σ_e kbar
2	7.5
12	5.5

C. Hugoniots

The yield level in uniaxial strain was inferred by
comparison of the elastic ($\rho_0 C_L$) and plastic
(σ_H vs. u_p) hugoniots, i.e., by defining the elastic

limit as the intersection of the elastic response
line and the curve-fit to the stress-particle velocity
data

$$10 \ \rho_0 C_L u_e = A + B u_e + C u_e^2 \left(= \sigma_e \right) \tag{24}$$

Solving for u_e gives

$$u_e = 0.033 \text{ mm/}\mu\text{sec}$$

$$\therefore \sigma_e = 5.7 \text{ kbar}$$

For an isotropic, polycrystalline metal with elastic-perfectly
plastic behavior and no strain-rate or time-dependent effects,
one would expect the same yield to be obtained by each method.
Although not strain-rate sensitive in the uniaxial stress tests,
6061-T6 does show relaxation of the elastic wave in uniaxial
strain. However, the elastic wave approaches an "equilibrium"
yield of 5-6 kbar which is essentially the same as the yield
obtained from uniaxial stress or hugoniot data. An average
value of 5.7 kbar was used in determining the $\sigma_H - \mu$ and
$U_S - u_p$ equations given above (Equation 11) for 6061-T6 in
the low-pressure region.

SECTION V

WAVE PROPAGATION

Compressive wave development and elastic precursor decay are
used as basic input data for material response models, while
a complete understanding of shock wave propagation requires
inclusion of release wave behavior (see, e.g., Refs. 23,
67-70). Profiles of shock waves propagated through a specimen
are obtained as stress-time or velocity-time histories. Pro-
files may be used in this form directly for comparison with
calculated or predicted material response. When it is neces-
sary to transform the data to obtain material stress from
transducer stress or particle velocity from interface velocity,
an impedance matching technique is applied, utilizing the con-
servation relations and assuming time-independent behavior.
The implications of this assumption must be considered when
utilizing the transformed data. All wave profiles obtained
(quartz gage and velocity interferometer) are given in Appen-
dix F for reference.

COMPRESSIVE WAVE BEHAVIOR

Structure in the compressive wave in 6061-T6 is shown in the
quartz gage data in Figure 17.[*] The wave front is character-
ized by an elastic portion and a transition to a spreading

---

[*] In this and subsequent figures containing quartz gage data,
tilt refers to the time required for a step-input to sweep
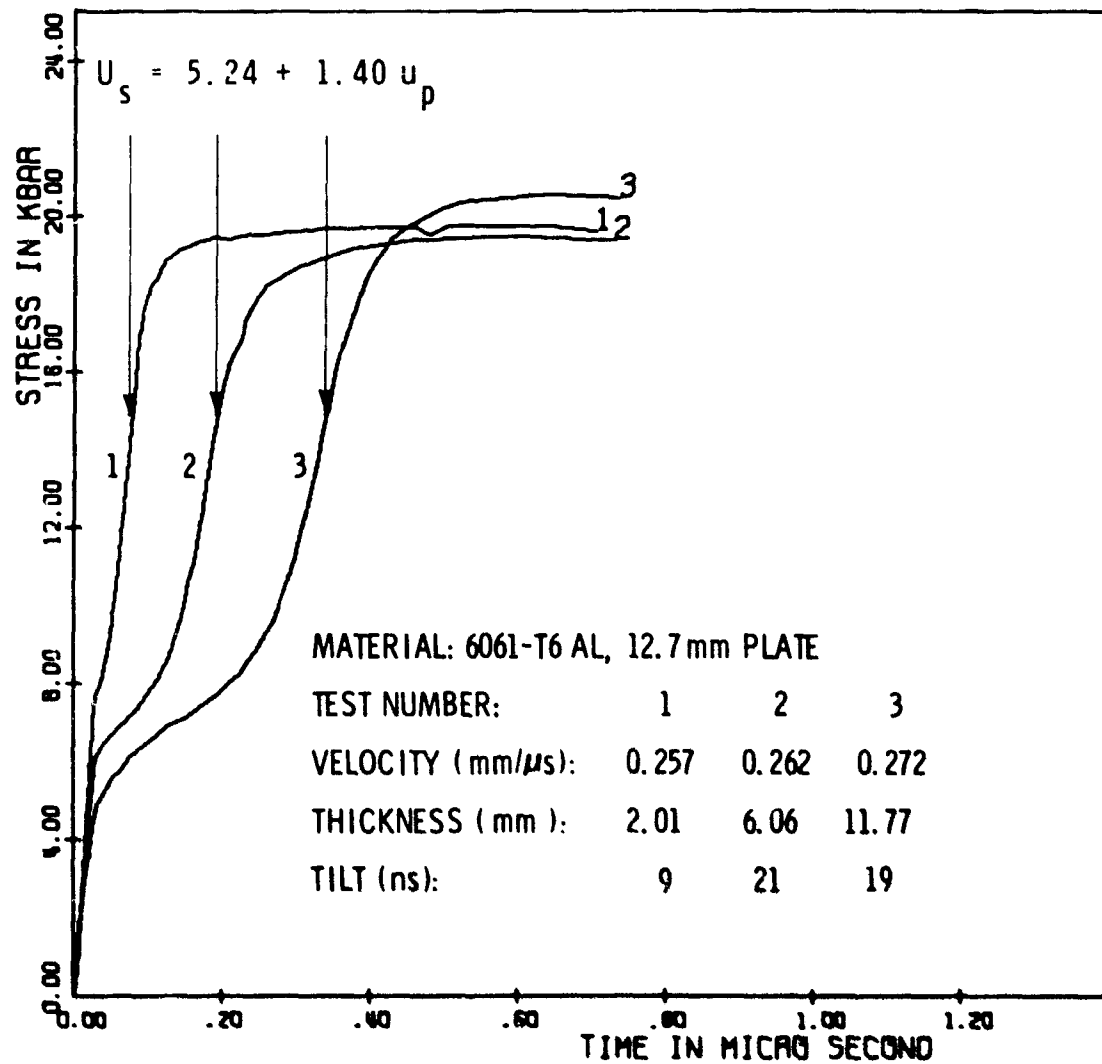across the gage electrode diameter.

Figure 17   Compressive Waves, Propagation
             Distance Dependence

plastic wave (nominal final stress of 20 kbar). (The elastic
wave would be overdriven by the plastic wave at $\sim$ 140 kbar.)
The elastic portion is not appreciably influenced by peak
stress, at least for stresses up to 4 times the elastic limit,
as shown in Figure 18. Also shown in Figures 17 and 18 are
shock velocities as calculated from the shock wave hugoniot
(Equation 11). Although there is qualitative agreement in
that the predicted plastic wave velocity lies within the rise-
time of the measured wave, the plastic wave cannot be considered
to have a unique velocity for a given stress level, at least
for stresses below $\sim$ 25 kbar. This means that transformation
of the hugoniot from the $\sigma_H - u_p$ plane to $\sigma_H - \mu$ or $U_S - u_p$
by assuming ideal elastic-plastic wave structure and steady-
state conditions may lead to some uncertainty at lower stresses.

Stress-particle velocity paths were calculated from quartz gage
transmitted wave profiles and are compared to the hugoniot in
Figure 19. The calculations were made using QZ, a program which
assumes steady-state behavior and applies the hugoniot jump
conditions incrementally to the wave profile by an impedance
matching technique.[50] The dynamic paths generally lie above
the equilibrium hugoniot with only the end points or final states
approaching the equilibrium values. This deviation is due to
time-dependent effects.

The conditions for development of steady-state plastic waves in
6061-T6 were studied by conducting a series of velocity inter-
ferometer tests and combining the results with similar data
reported by Johnson and Barker.[33] In an elastic-plastic wave
system, the effects of time-dependency and non-linearity in-
itially can cause the plastic portion to spread as it propa-
gates. Eventually, however, the plastic portion may achieve
a stable condition and propagate relatively unchanged (provided
conditions of uniaxial strain are maintained and the wave front
is not overtaken by a release wave).

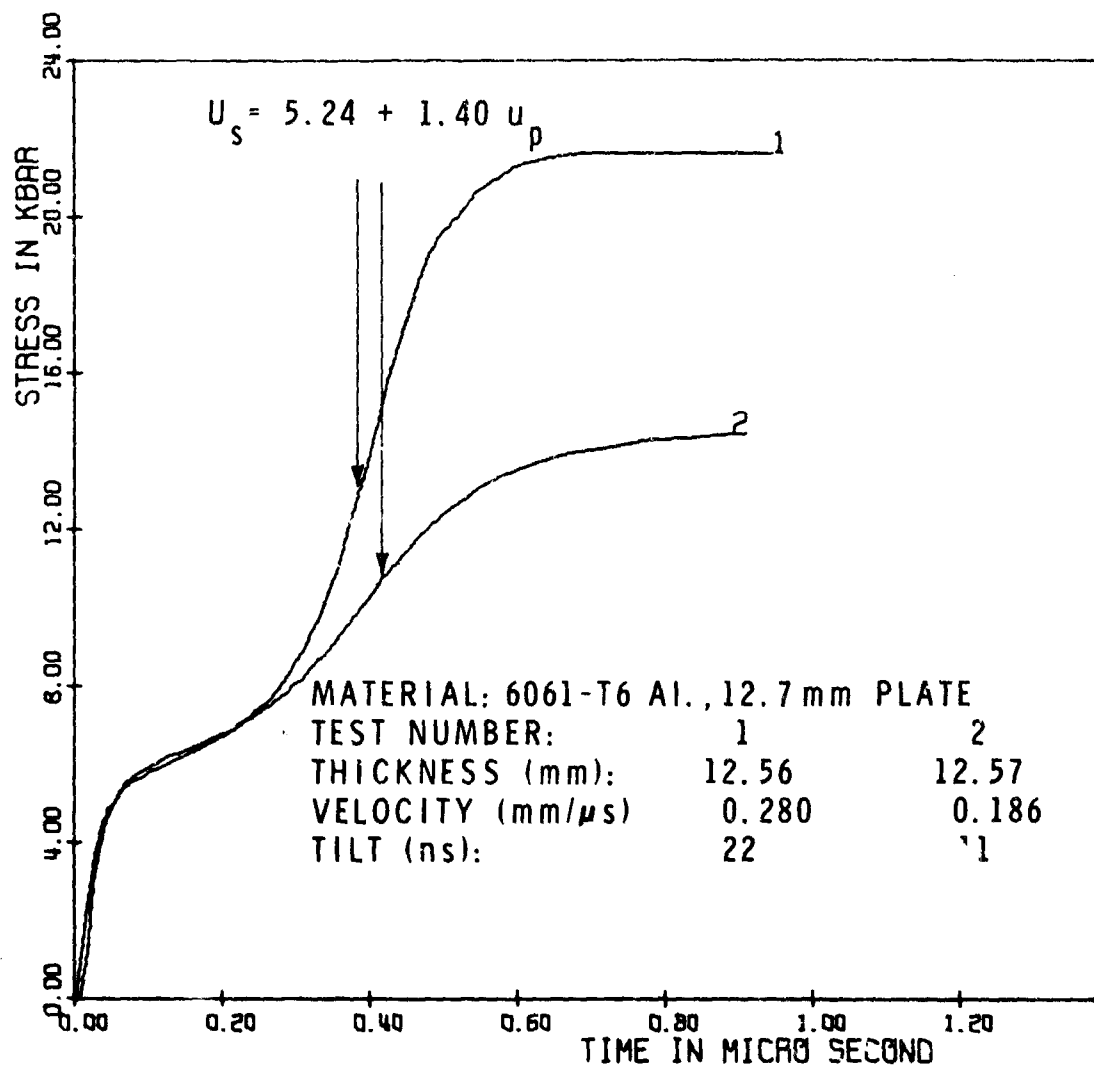Figure 18   Compressive Waves, Peak Stress Dependence
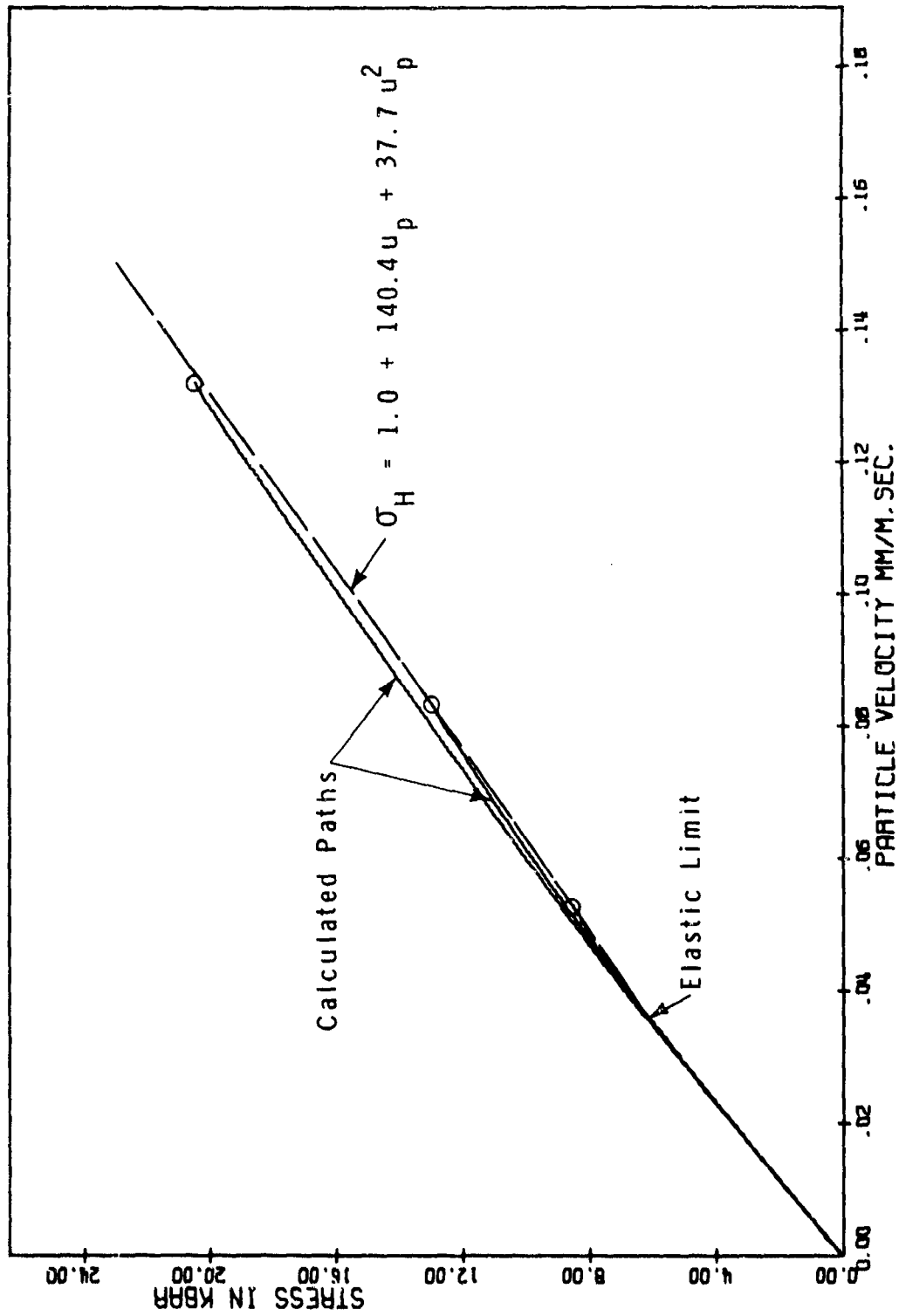
Figure 19   Calculated Stress-Particle Velocity Paths, 6061-T6

Compressive wave profiles are shown in Figure 20 for two series
of tests using the velocity interferometer: varying peak stress
at constant propagation distance, and varying propagation dis-
tance at constant peak stress. (Test conditions for velocity
interferometer data discussed in this report are listed in
Table IV. The test numbers correspond to those listed next to
each wave profile in subsequent figures.) At ∿ 26 kbar the
rise-time in the plastic wave increases between 3 and 12 mm,
but wave stability is achieved by 20 mm. The series at 3 mm
thickness shows a steepening plastic wave with increasing peak
stress. A more complete mapping of the formation of steady-
state waves is given in Figure 21.[*] Tests at a given stress
which showed steady-state behavior in the plastic wave are
shown by solid symbols. The shaded area shows the indistinct
border between non-steady-state and steady-state behavior.

Dislocation models for predicting compressive wave development
utilize measurements of elastic precursor decay to evaluate
various constants related to dislocation density and multipli-
cation.[69-72] Unfortunately, it is very difficult to obtain
accurate elastic precursor level data at propagation distances
less than ∿ 2 mm and it is in this region (0 to 2 mm) that most
of the precursor decay occurs for many metals of interest.
Also, even at larger distances there is always some uncertainty
in the precursor level due to both material scatter and disper-
sion characteristics and to experimental errors (particularly
tilt). The result is that much of the data presently available,
when given realistic uncertainty bars, can be used to support
a number of different models of precursor attenuation. The

---

[*] Steady-state conditions were studied by comparing rise-times
in the plastic wave at approximately 20 to 80% stress levels
above the elastic limit.

precursor decay data for 6061-T6 is summarized in Figure 22.
The calculated initial <u>elastic</u> impact stress was 23 kbar for
these tests and the precursor level has dropped ∿ 70% in
2 mm of travel. Over the range of propagation distance studied,
the precursor level in 12.7 mm stock was ∿ 1 kbar greater than
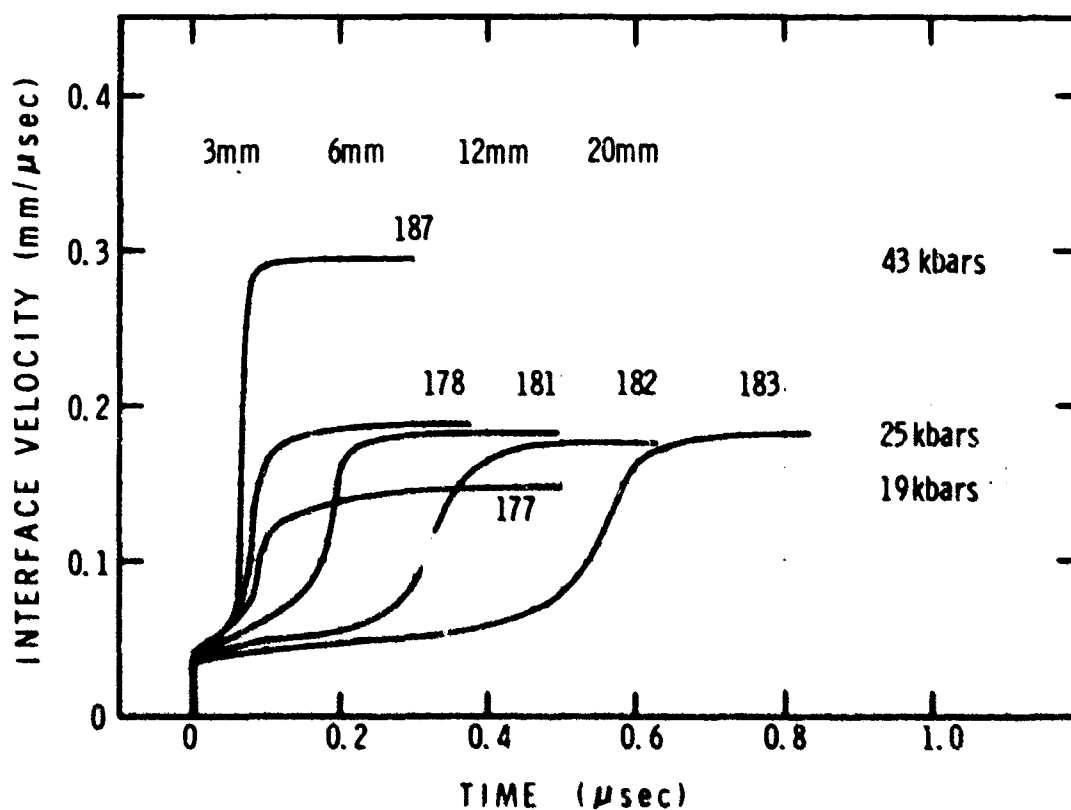in the 3.2 or 6.4 mm stock.

Figure 20   Compressive Wave Development, 6061-T6

TABLE IV

VELOCITY INTERFEROMETER TEST DATA, 6061-T6 ALUMINUM

Test No.	V_I Impact Velocity (mm/μs)	σ Max. Stress (kbar)	X_0 Impactor Thickness (mm)	X Target Thickness (mm)	X/X_0	Stock (mm)	Config.[1]
15	0.269	21	1.879	3.124	1.66	3.2	Al-Al
50	0.222	17	1.552	3.081	1.99	3.2	Al-Al
52	0.252	19	1.587	12.220	7.70	12.7	Al-Al
53	0.284	22	1.440	18.192	12.63	50.8	Al-Al
61[2]	0.510	39	1.580	3.106	1.97	3.2	Al-Al/FQ
63	0.193	15	1.570	3.058	1.95	3 2	Al-Al
73[2]	1.242	103	0.269	2.520	9.37	3.2	Al-Al/FQ
74[2]	1.238	102	0.252	5.067	20.15	6.4	Al-Al/FQ
79[2]	1.235	102	0.252	1.029	4.09	1.6	Al-Al/FQ
83	0.261	20	0.475	1.181	2.49	3.2	Al-Al
104	0.255	19	.590	3.080	1.94	3.2	Al-Al
108	0.263	20	1.562	2.776	1.78	3.2	Al-Al
109	0.340	26	0.431	3.985	9.23	6.4	Al-Al
110	0.418	32	0.419	3.970	9.47	6.4	Al-Al
133	0.265	20	1.600	3.073	1.92	3.2	Al-Al
135	0.247	19	1.598	3.178[3]	1.99	1.6	Al-Al
143	0.306	23	0.904	3.061	3.39	3.2	Al-Al
177	0.275	19	2.982	3.249	1.09	50.8	FQ-Al/FQ
178	0.373	25	3.058	2.972	0.97	50.8	FQ-Al/FQ
181	0.358	24	3.018	6.033	2.00	50.8	FQ-Al/FQ
182	0.354	24	3.061	12.141	3.97	50.8	FQ-Al/FQ
183	0.329	25	12.649	20.259	1.60	50.8	Al-Al/FQ
187	0.489	43	3.157	2.977	0.94	50.8	FQ-Al/FQ

1. e.g., Al-Al is aluminum impactor into aluminum target with free rear surface (FQ is fused quartz window).

2. Plexiglas – backed impactor.
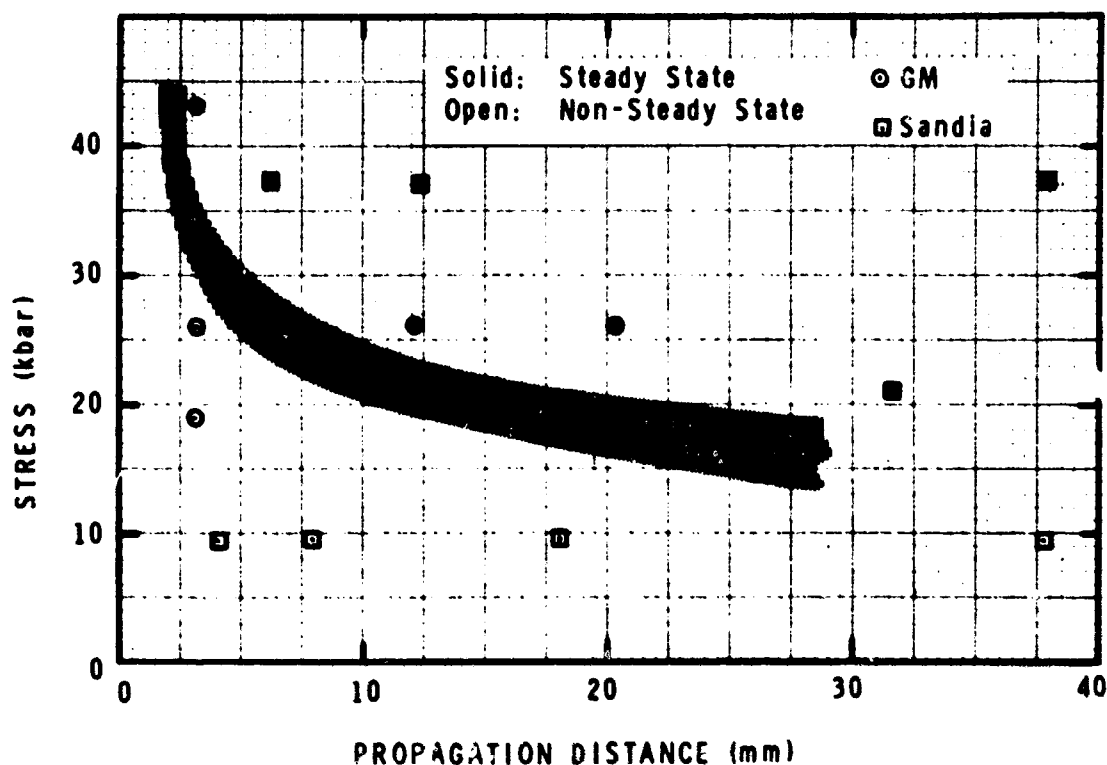
3. Artificial spall plane at X/2.

Figure 21   Steady State Wave Conditions, 6061-T6

The uncertainty bars in Figure 22 reflect the dispersion and
rounding at the elastic front. This spreading is due to at
least two factors. First, since the quartz gage averages stress
over the electrode area, small differences in wave front arrival
times at the specimen/gage interface would give a finite rise-
time rather than an instantaneous stress jump. These small
differences in arrival times may be due to wave reflections and
dispersion at grain boundaries and to slight differences in
local wave velocity arising from grain anisotropy. Second, the
influence of shock wave tilt on a finite-area gage is to smooth

out abrupt changes in stress level as well as to increase re-
cording rise-time in the wave front. This becomes particularly
severe at short propagation distances where separation of the
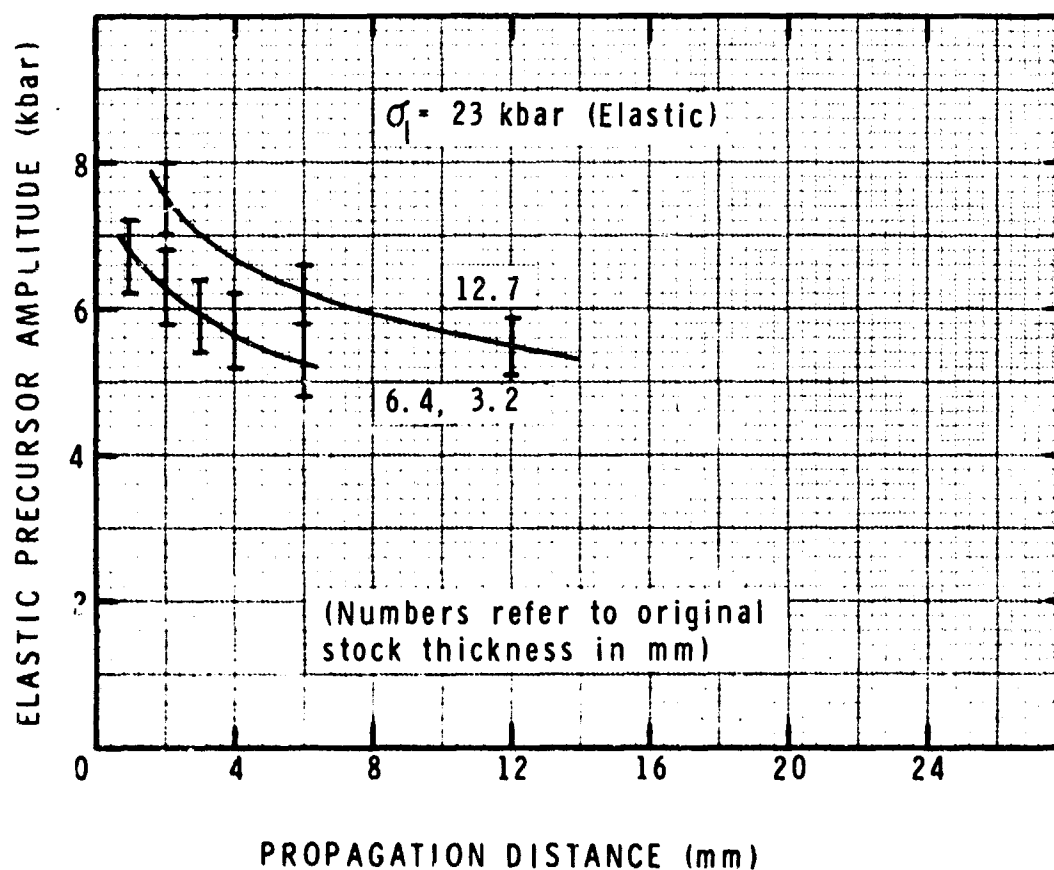elastic and plastic waves is only on the order of tens of nano-
seconds.

Figure 22   Elastic Precursor Decay, 6061-T6

Of about 15 quartz gage transmitted wave tests conducted with
6061-T6, only one showed relaxation behind the elastic precursor,
as shown in Figures 23 and 24. This relaxation was observed for
a propagation distance of 11.25 mm with 50.8 mm stock, but was
not observed for propagation distances of 6 or 20 mm in targets
machined from the same plate. Tilt was slightly higher for the
6 mm test (23 nsec), which may have smeared the wave front such
that relaxation could not be resolved. For the 20 mm test, which
had a tilt of 16 nsec, the precursor "spike" may have relaxed
completely. Material variability could also have influenced
the results.

12.7 mm PLATE   50.8 mm PLATE

$Al \rightarrow Al/Q$ $Al \rightarrow Al/Q$

$V_1 = 0.272$ mm/μs $V_1 = 0.271$ mm/μs

$\sigma_s = 20.8$ kbar $\sigma_s = 20.7$ kbar
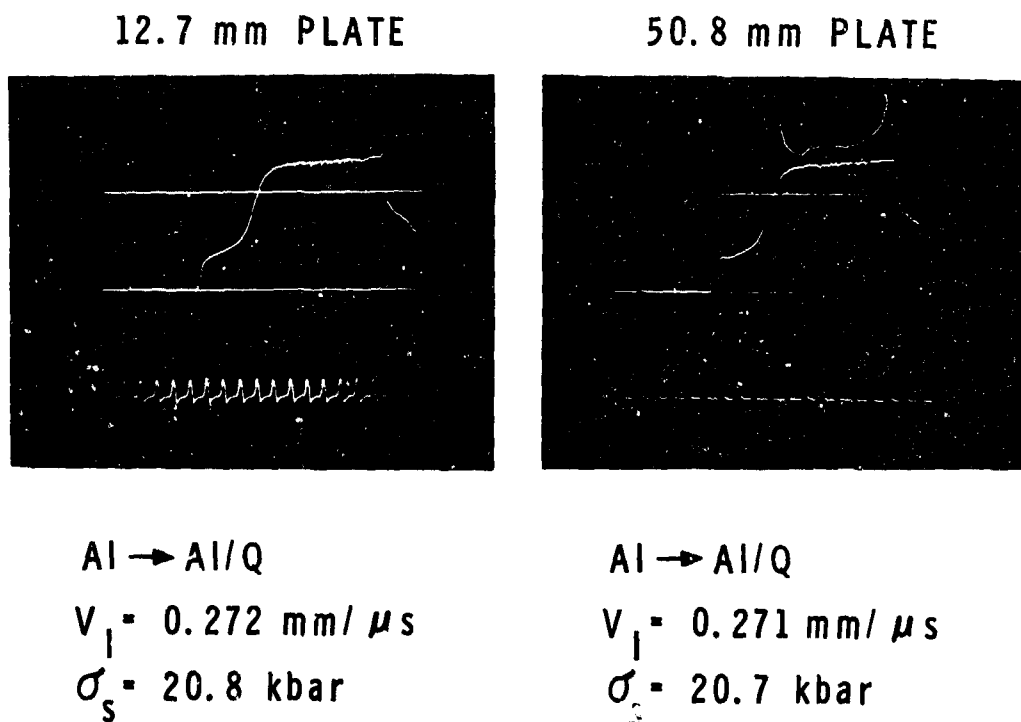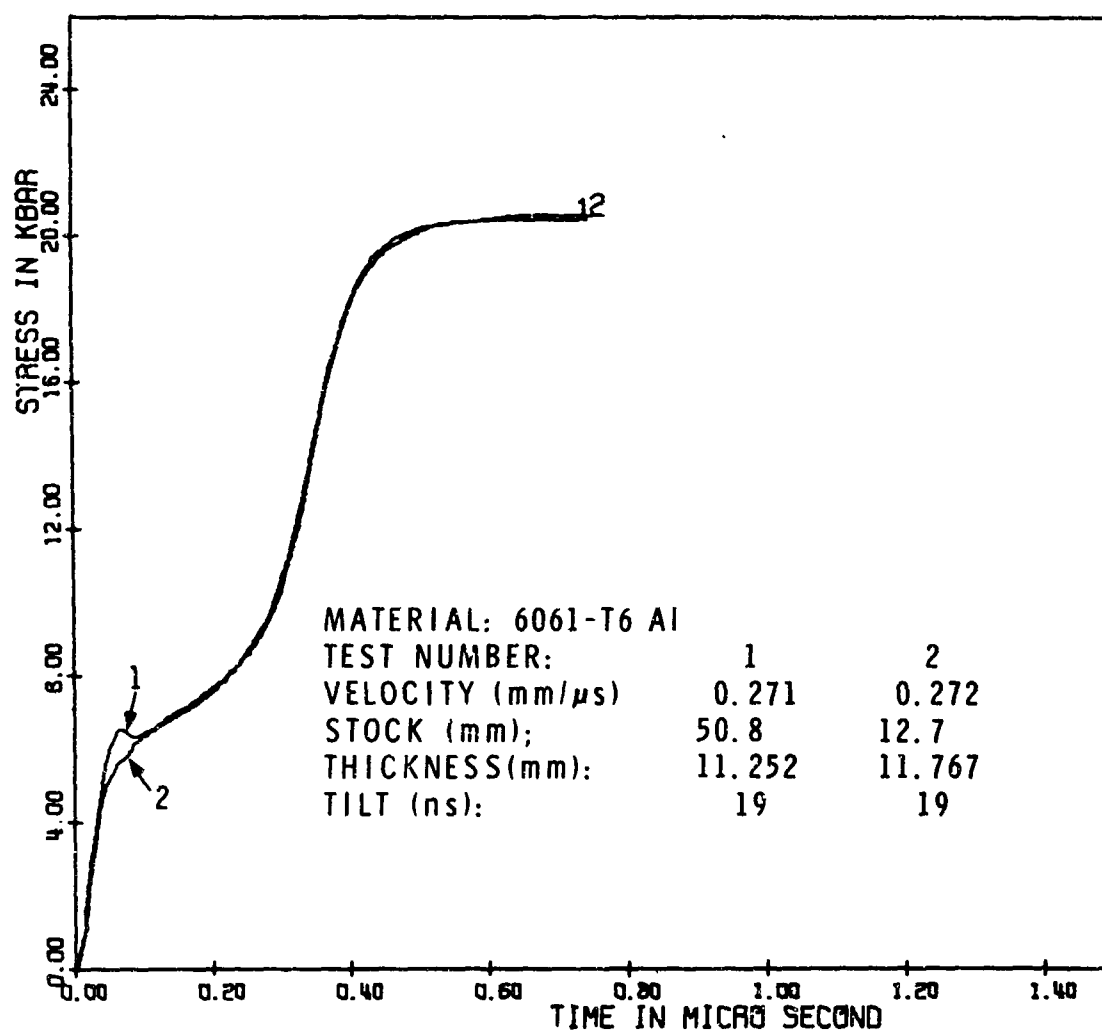
Figure 23   Quartz Gage Transmitted Wave
             Records, 6061-T6

Figure 24   Compressive Waves, Material Differences

Compressive wave structure was also measured in annealed 6061, and is compared with 6061-T6 in Figure 25. The elastic limit has decreased to $\sim$ 1 kbar for this propagation distance (3.1 mm).

MATERIAL: 6061 AL, 3.2mm PLATE

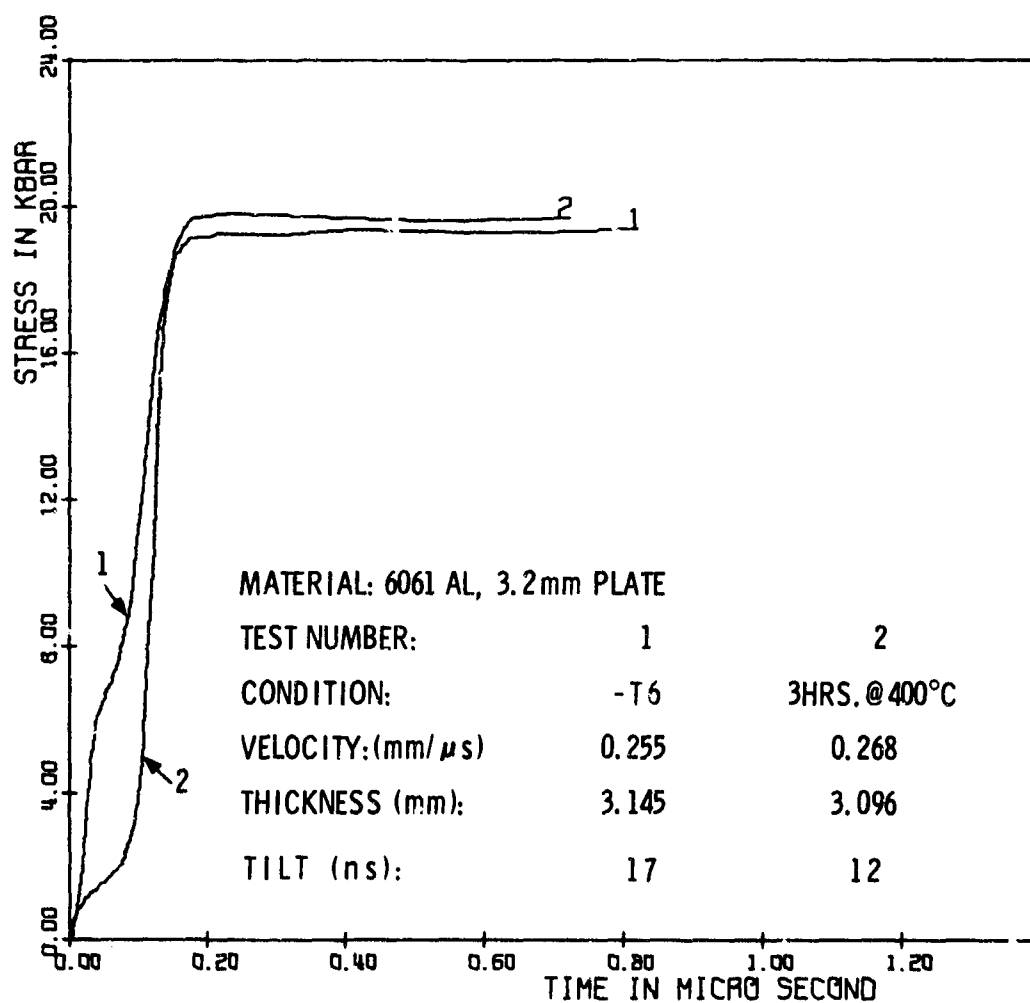| TEST NUMBER:	1	2
CONDITION:	-T6	3HRS.@400°C
VELOCITY:(mm/μs)	0.255	0.268
THICKNESS (mm):	3.145	3.096
TILT (ns):	17	12

Figure 25   Compressive Waves, Annealing Effect

RELEASE WAVES AND WAVE ATTENUATION

Release waves in 6061-T6 were studied by using relatively thin
impactors and measuring the complete wave profile with the
laser velocity interferometer. After impact, elastic and
plastic waves propagate from the impact surface into both im-
pactor and target. The waves that reach the impactor rear
surface reflect as rarefaction waves, unloading the material.
These unloading waves propagate across the impact surface into
the target and are recorded at the target rear surface after
arrival of the compressive wave.

Three unattenuated wave profiles for 6061-T6 are shown in
Figure 26, one with a 6061-T6 impactor and two with fused
quartz impactors. (Additional impact data are given in Table IV).
All three targets had fused quartz windows on the rear face to
reduce the magnitude of unloading due to reflection of the com-
pressive wave. This prevents spall fracture in the target.
The 6061-T6 impactor for test 61 was backed by Plexiglas to
prevent bowing during launch and this accounts for the wave not
releasing completely. Also, the measured interface velocity for
these tests is slightly higher than particle velocity in the tar-
get since the impedance of 6061-T6 is slightly greater than fused
quartz. Structure is evident in the release wave for all three
tests, however, the development of this structure for test 61
with a 6061-T6 impactor is more complex than for tests with fused
quartz impactors. This is because elastic and plastic waves
spread in the 6061-T6 impactor such that all the unloading does
not occur at the same time, i.e., the release wave does not
start out as an abrupt pressure drop. The fused quartz impactor
gives a "square" input wave to the target, with a nearly instan-
taneous release at the impactor-target interface. Therefore,
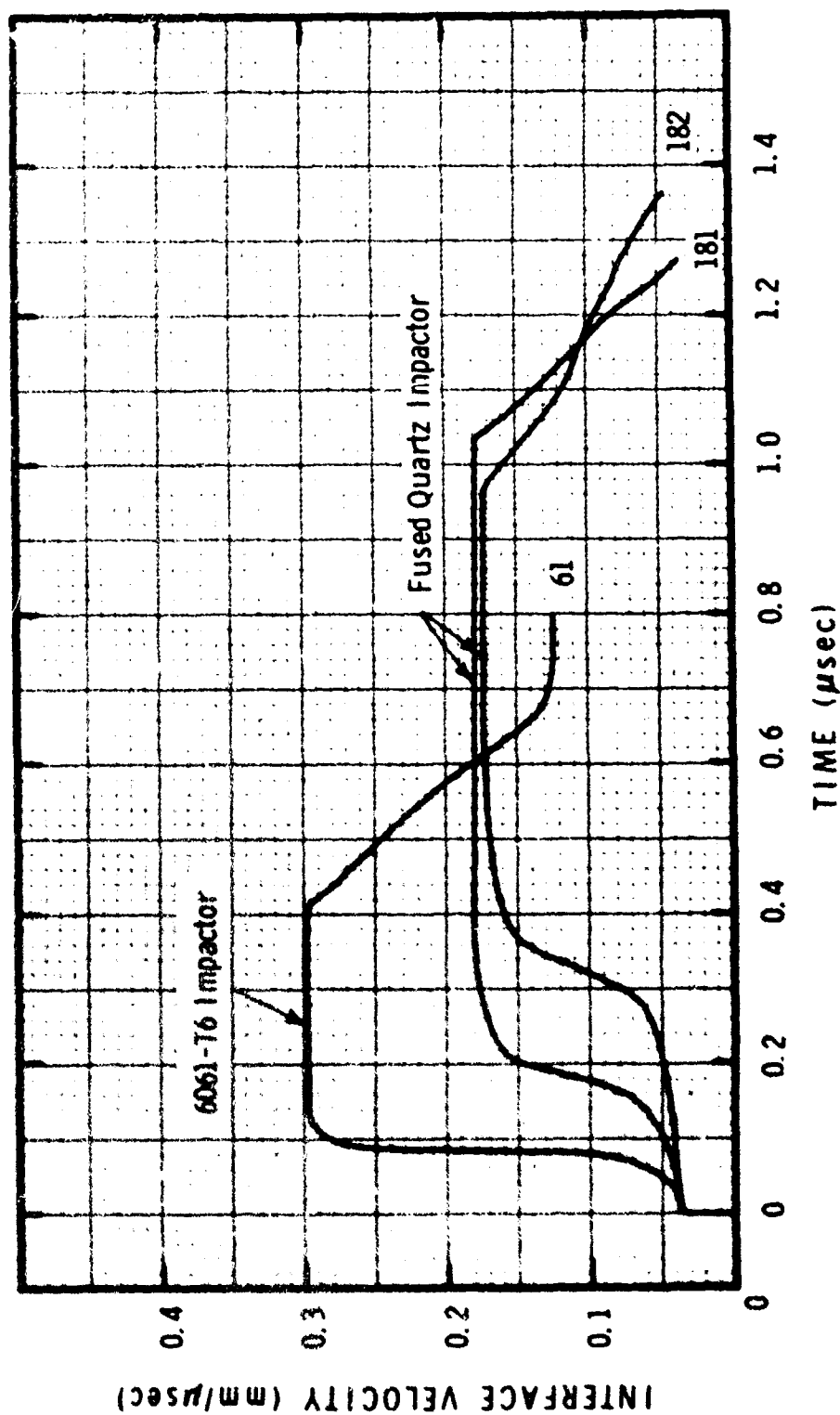
Figure 26   Complete Wave Profiles, 6061-T6

the structure in the release waves for tests 181 and 182 should
be due to elastic-plastic unloading in the target material only.
A shock wave attenuation study by McMillan, Isbell and Jones
indicated that the initial pressure release in 6061-T6 is elas-
tic even at pressures up to 1 mbar and the elastic release wave
amplitude increases with increasing peak pressure.[73]

If target thickness is great enough compared to impactor thick-
ness, the release wave will overtake the compressive wav_ and
attenuate the peak stress. Wave attenuation is shown in Fig-
ure 27 for an initial stress of 20 kbar and in Figure 28 for
an initial stress of 102 kbar. At the higher stress level, the
impactors were backed by Plexiglas so the stress wave was not
released to zero. The attenuation results are shown in Fig-
ure 29 in terms of decrease in peak stress vs. X/X_0. Also shown
are calculated overtaking points assuming ideal elastic-plastic
compression and release waves. This is given by:

$$\frac{X}{X_0} \approx \frac{\dfrac{1}{C_L} + \dfrac{1-u_p/U_S}{C_L^1 - u_p}}{\dfrac{1}{U_S} - \dfrac{1-u_p/U_S}{C_L^1 + u_p}} \tag{25}$$

where C_L^1 is elastic release wave velocity (6.5 mm/us
for 20 kbar and 7.0 mm/us for 102 kbar[73]).

The experimental results for 102 kbar are consistent with
the calculated overtaking point, but the results for 20 kbar
show attenuation much sooner than calculated. This can be
attributed to the ramped plastic compressive wave at this

stress. If the velocity ($\sim$ 4.65 mm/μs) of the trailing por-
tion of the plastic wave at 20 kbar is used for U_S rather the
value (5.43 mm/μs) obtained from Equation 11, then the calcu-
lated overtaking point is $X/X_0 = 4.5$. This value is consistent
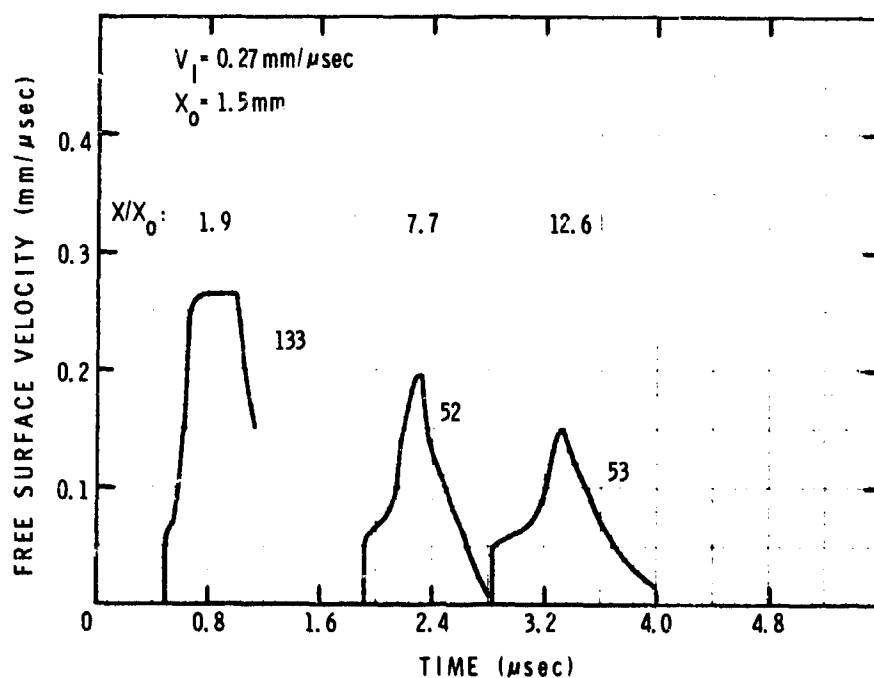with the experimental results for 20 kbar.
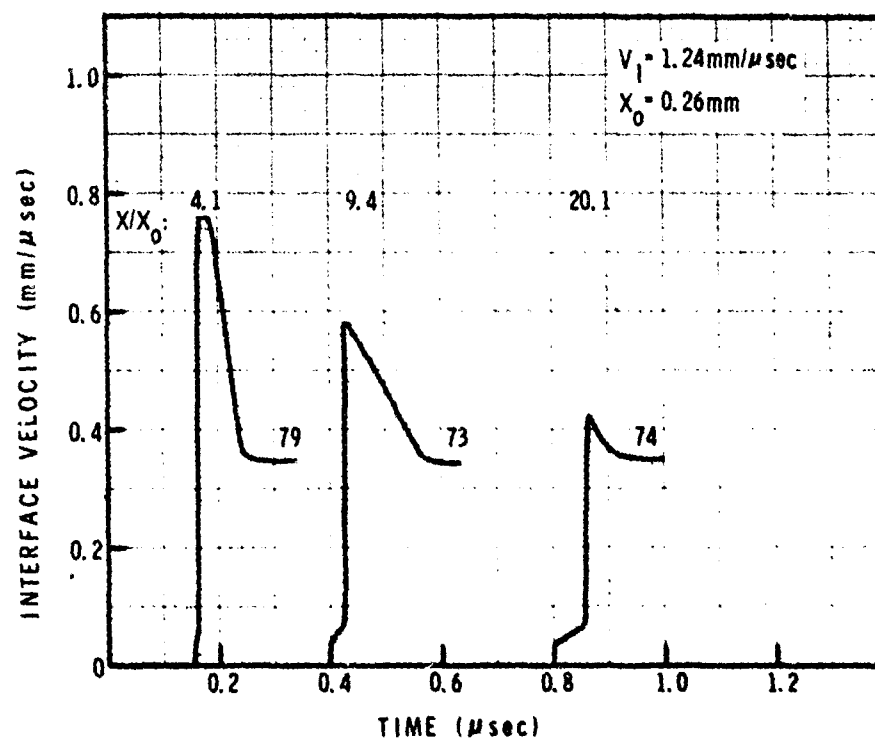

Figure 27   Wave Attenuation, Low Pressure, 6061-T6

Figure 28   Wave Attenuation, High Pressure, 6061-T6
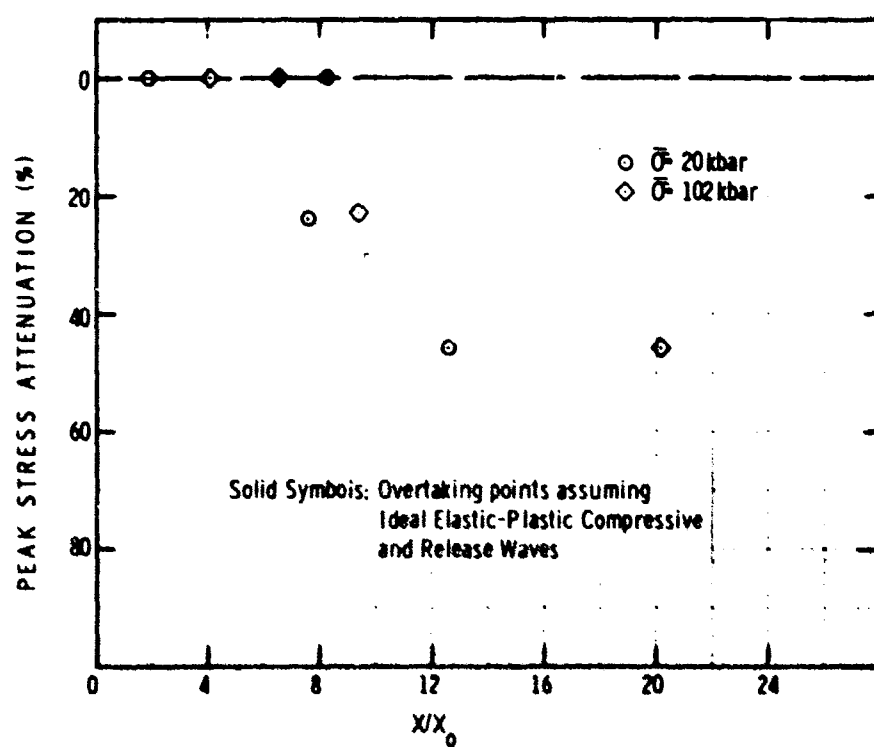
Figure 29   Peak Stress Attenuation, 6061-T6

SECTION VI

SPALL FRACTURE

Spall fracture by plate impact results from reflection of
compressive waves from a relatively low impedance interface
(normally a free surface) and subsequent wave interaction
(see, e.g., Refs. 74-76). Spall studies were carried out
with both passive and active techniques. Passive methods
involve the recovery and examination of shock-loaded speci-
mens. Metallographic examination establishes the type and
degree of damage, which can be correlated with test parameters
such as velocity, impactor thickness and target thickness.
Active methods utilize the laser velocity interferometer and
provide quantitative, time-resolved data on the influence of
internal fractures or spall surfaces on shock wave profiles,
as measured at the rear surface.

RECOVERY TESTS

The spall behavior of 6061-T6 was studied by carrying out a
series of impact and recovery tests, where the target was
sectioned across a diameter, polished, etched, and examined
optically at a magnification of 50X. The specimens were then
graded or classified according to the degree of fracture that
was observed, which ranged from no visible damage to complete
material separation. The onset of significant fracture is
generally referred to as incipient spall and is a critical
point since it can be used to deduce the dynamic fracture
strength, and corresponds to generation of sufficient free

surfaces within the material to reflect a portion of the
interacting release waves as a compressive wave. The incip-
ient spall threshold was defined as the impact velocity (for
a given set of impact parameters) corresponding to cracking
over at least 50% of the width of the section estimated to be
under a condition of plane strain during the time of loading.

Incipient spall results from all tests, including an attenuated
pulse series and elevated temperature tests, are summarized in
Table V. The data for all 20°C tests with unattenuated pulses
$(X/X_0 \simeq 2)$ are given in Figure 30. The symbols are defined as:

- ● Complete Separation

- ◒ Above Incipient

- ◓ Incipient Spall

- ◐ Below Incipient

- ○ No Visible Damage

As is typically the case with metals, the impact velocity for
incipient spall increases for decreasing impactor thickness.
This implies that peak stress (and, therefore, strain) required
to create spall fractures increases with decreasing pulse width
or time of loading. These results are compared to those of
Kreer[77] and Butcher, et al.[74] in Figure 31. These data are
all for gun-launched, plate-impact techniques.* Although
Butcher's tests were for $X/X_0 = 4$, a comparison with data for

---

* Spall in 6061-T6 has been studied by Keller and Tuler[78],
  Jajosky and Ferdman[79] and Cohen and Berkowitz[80], using
  exploding-foil techniques; however, their results are not
  included here since differences in experimental method, con-
  dition of the impactors and metallographic analysis prevent
  a direct comparison. Also, Stefansky and Shea[81] studied
  dynamic fracture in several metals, including 6061-T6, using
  electron beam pulses.

TABLE V

INCIPIENT SPALL DATA FOR 6061-T6 ALUMINUM

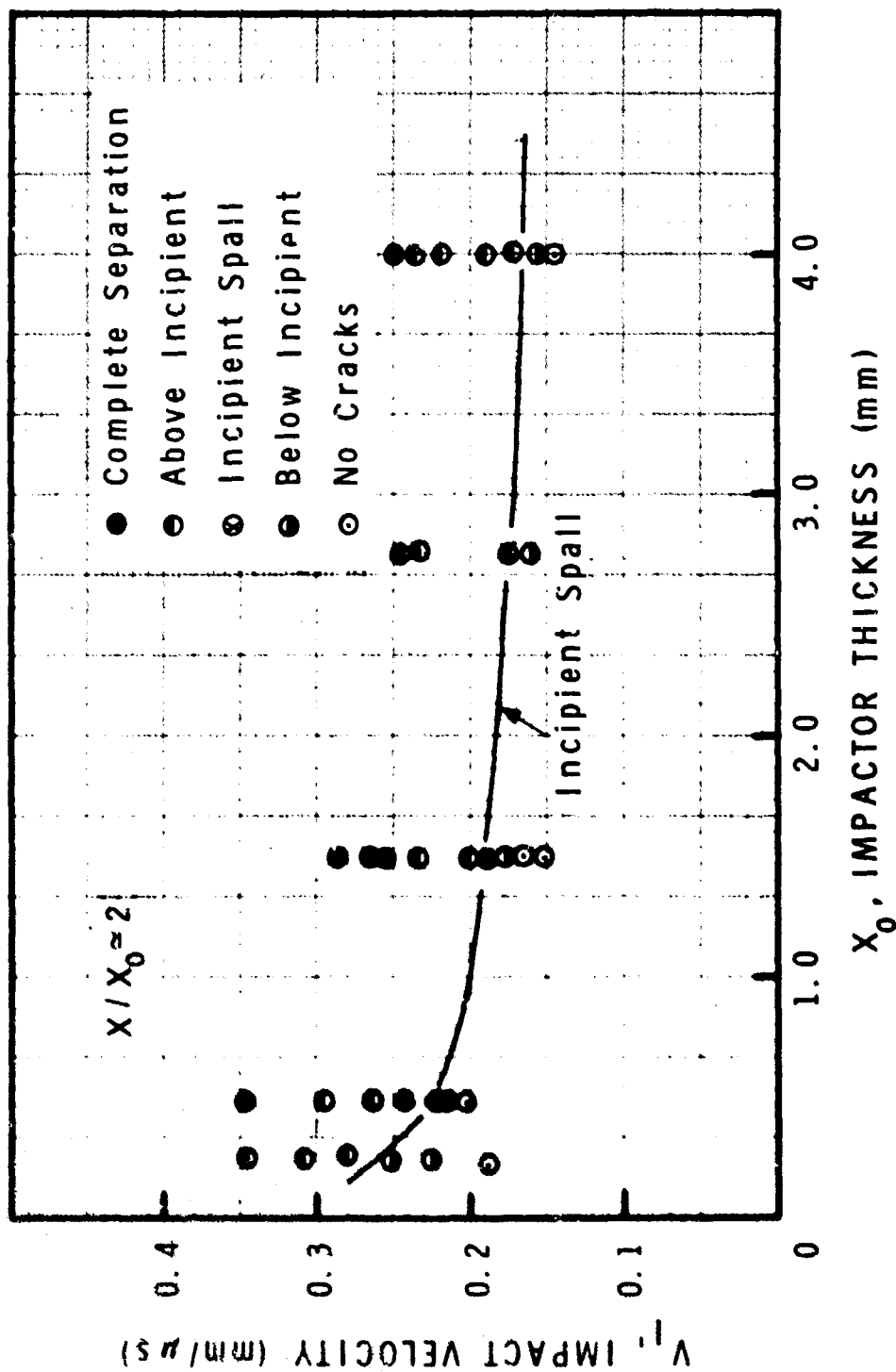| X_0 Impactor Thickness (mm)	X Target Thickness (mm)	X/X_0	T Temperature (°C)	Δt_e Pulse* Width (μs)	V_S Spall Velocity (mm/μs)
0.25	0.48	1.92	20	0.079	0.262
0.47	1.01	2.15	20	0.148	0.220
1.55	3.02	1.95	20	0.49	0.190
1.55	3.02	1.95	288	0.49	0.172
1.55	3.02	1.95	400	0.49	0.130
2.80	5.52	1.97	20	0.88	0.175
4.00	8.08	2.02	20	1.26	0.165
4.00	8.08	2.02	288	1.26	0.150
0.46	4.02	8.74	20	0.144	0.355
1.55	5.84	3.77	20	0.49	0.200

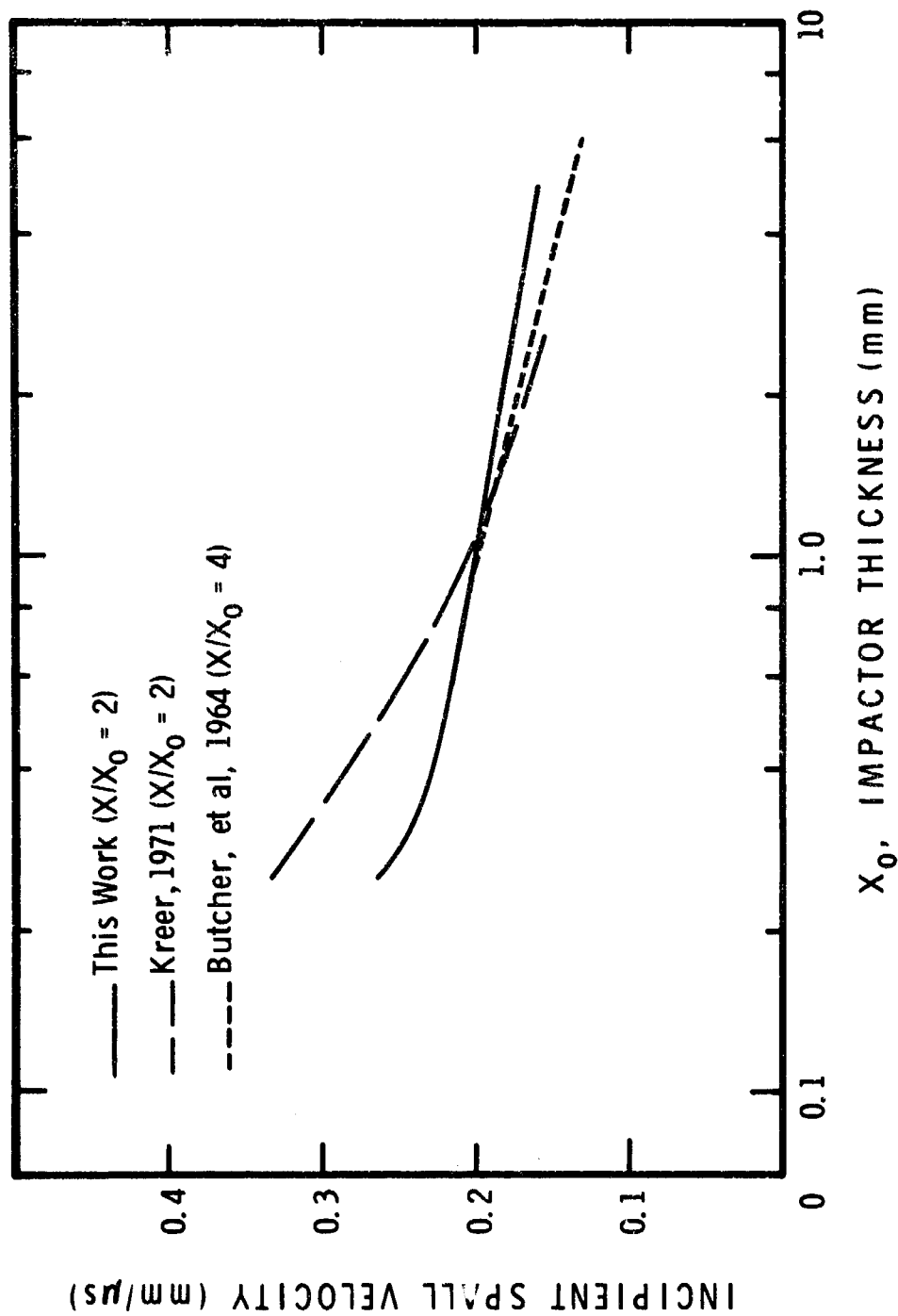$$* \ \Delta t_e = \frac{2X_0}{C_L}$$

Figure 30   Spall Data, 6061-T6

Figure 31   Spall Data Comparison, 6061-T6

$X/X_0 = 2$ is valid since the incipient spall threshold in
6061-T6 increases only $\sim$ 5% for a change in $X/X_0 = 2$ to
$X/X_0 = 4$, as shown in Figure 32. The data given in Figure 31
show reasonable agreement for $X_0 > 0.8$ mm. For thinner impactors,
however, the data from this work and that of Kreer deviate signi-
ficantly. This may be due to differences in experimental tech-
niques (e.g., impactor bowing, tilt, target construction or
metallographic methods); although Kreer indicates that material
property variation may also be a cause.

Optical photomicrographs of recovered specimens are shown in
Figures 33 to 35.[*] The specimens were polished and etched to
provide maximum contrast between cracks and sound material.
The procedure followed was:

1. Wet grind, 320/400/600 grit silicon carbide paper.

2. Rough polish, 5 μm aluminum oxide slurry on
   rayon cloth.

3. Final polish, 0.05 μm gamma alumina slurry on
   rayon cloth.

4. Etch, 10 ml hydrofluoric acid (HF), 15 ml hydro-
   chloric acid (HCl) and 90 ml water, 30-90 sec
   immersion (20°C), wash in warm water.

As noted above, spall cannot be rigorously defined in terms of
a unique impact velocity or stress, but requires consideration
of the degree of fracture. In general, as impact velocity in-
creases, spall progresses from isolated cracks or voids only
a few grains in size to complete material separation across the
entire spall plane.

---

[*] All spall photomicrographs in this report are oriented such
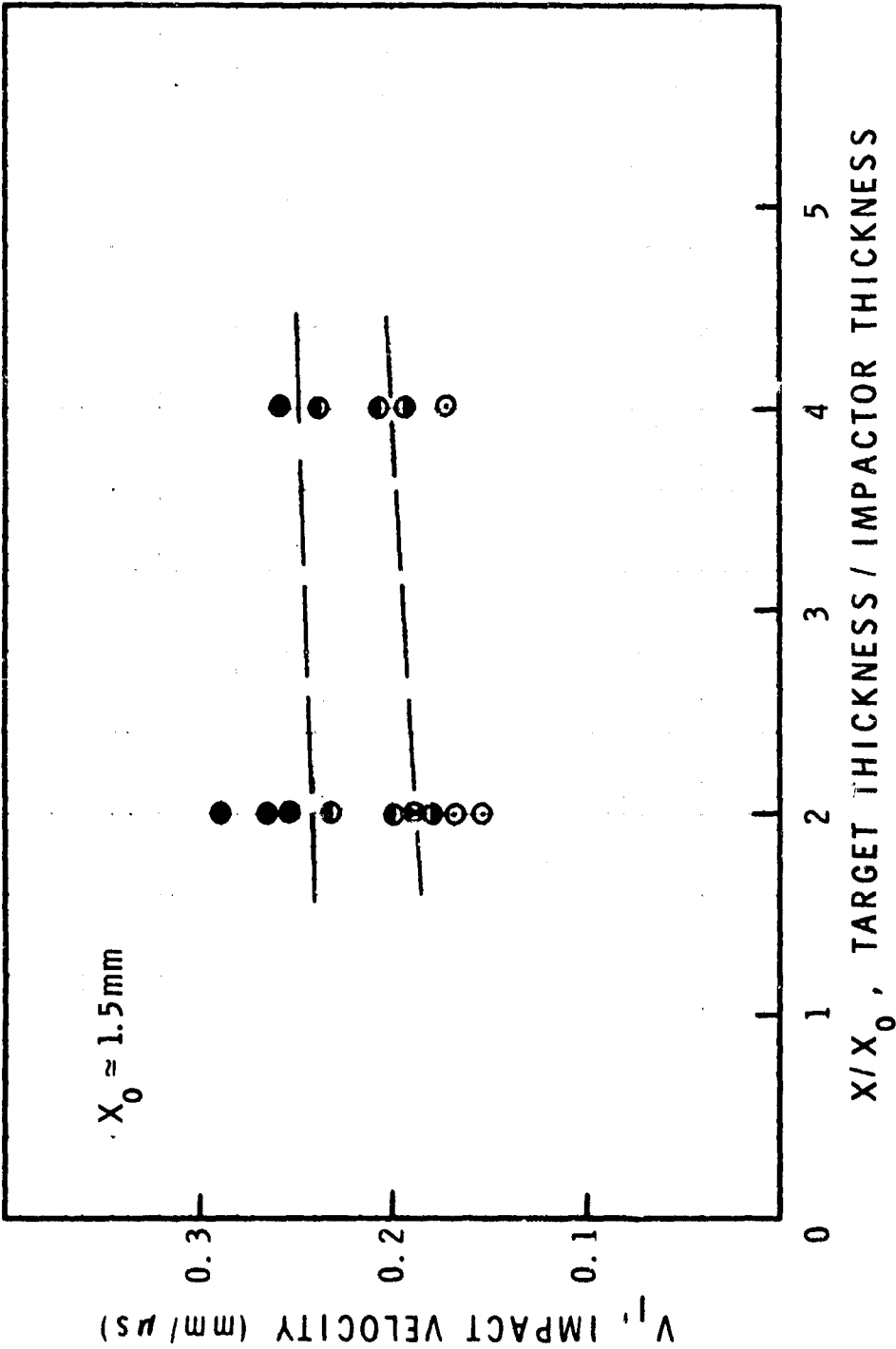that initial shock wave propagation was from bottom to top.

Figure 32   Spall Data, Thickness Ratio
             Dependence, 6061-T6
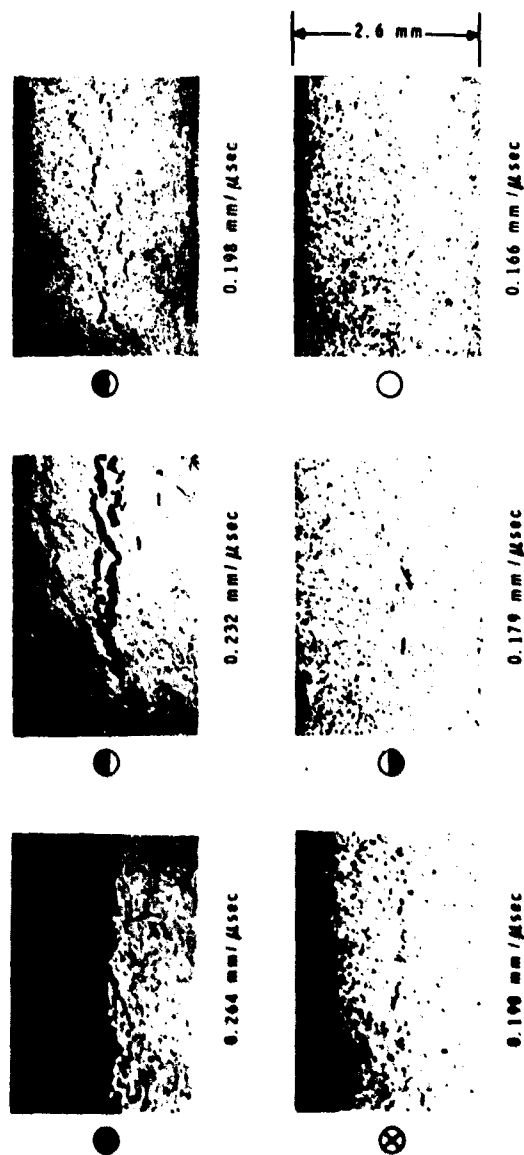
Figure 33   Spall Fractures, 6061-T6
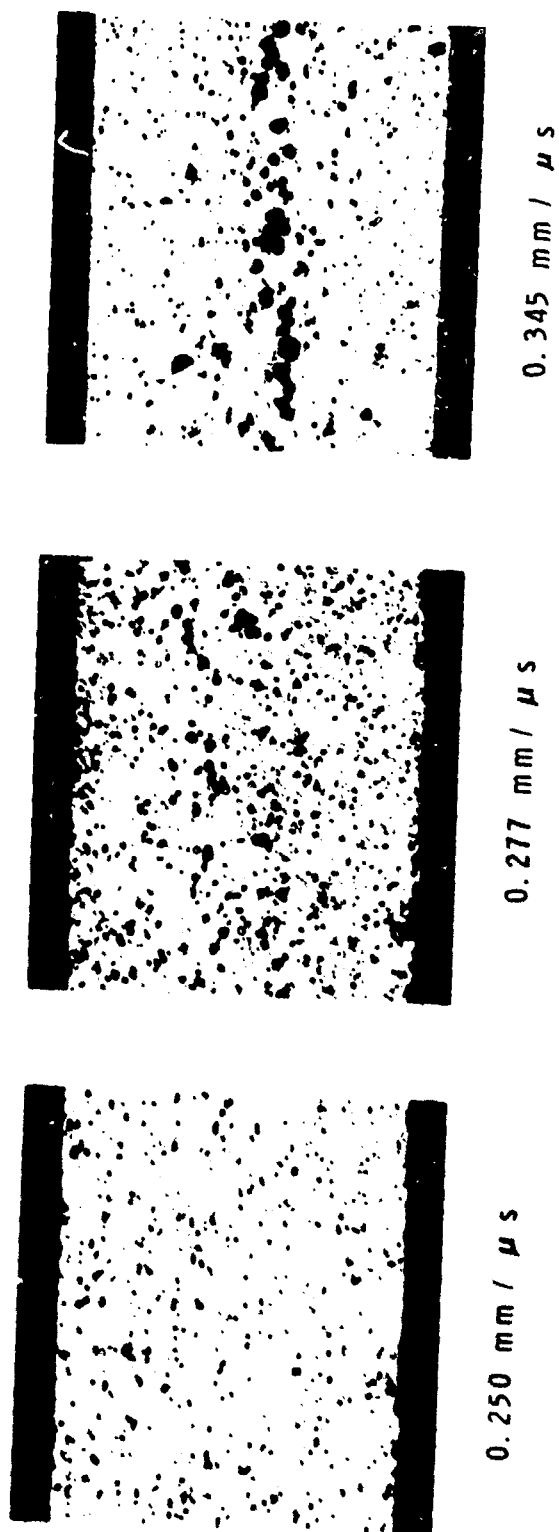
Figure 34   Spall Fractures, 6061-T6 (0.25 mm → 0.48 mm, 20°C)
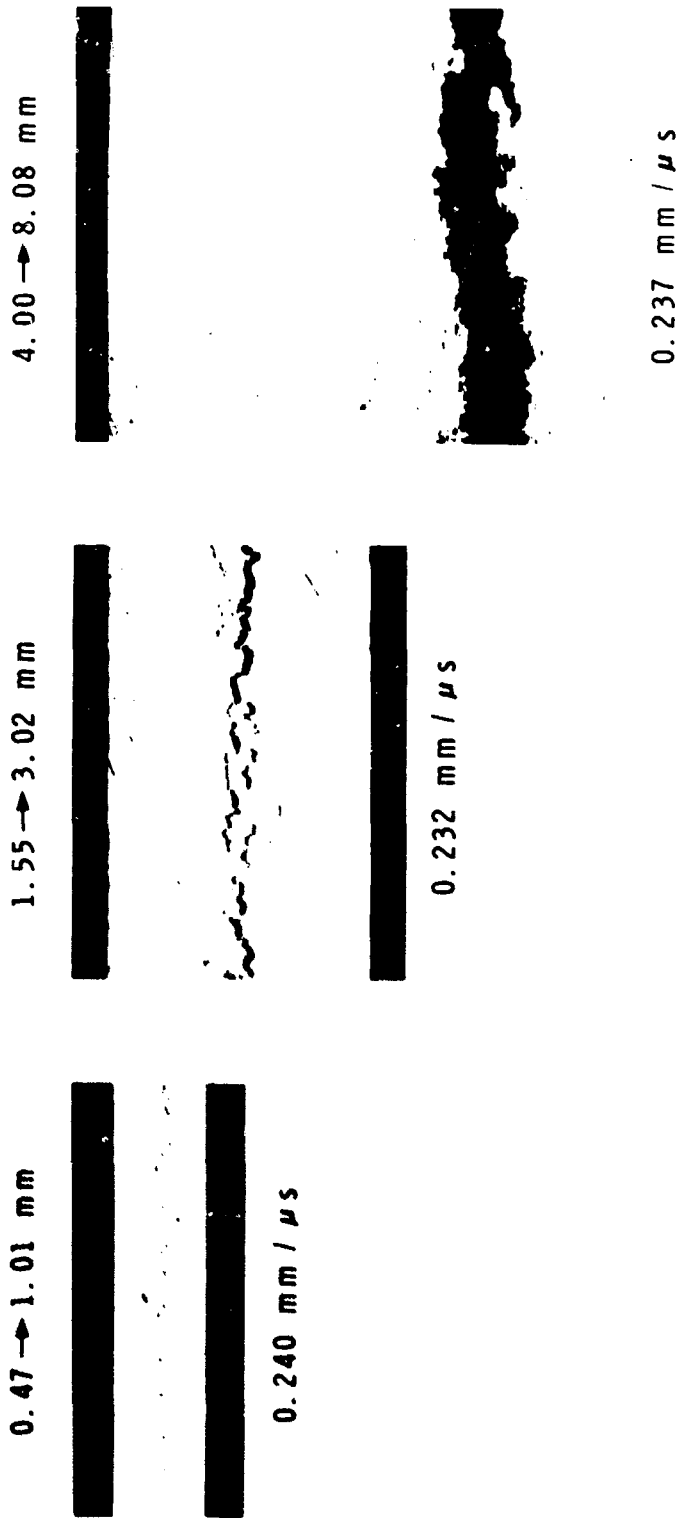
0.345 mm / μ s

0.277 mm / μ s

0.250 mm / μ s

Figure 35   Spall Fractures, 6061-T6 (20°C)

Fracture in 6061-T6 is of a ductile nature with the development
of individual voids. As velocity increases (see, e.g. Fig-
ures 33 and 34) the voids begin to coalesce and a complete
fracture surface is formed. Note that there is some disper-
sion of the voids around a nominal "spall plane". This was
also found for titanium[82] and tantalum[83], which have well-
defined elastic wave structures, while copper[84] has a poorly-
defined, low-amplitude elastic wave and showed very little void
dispersion around the spall plane. Spall fractures in the four
metals are compared in Figure 36.

Scanning microfractographs of the fracture surfaces for completely
separated specimens are shown in Figures 37 and 38. The voids ap-
pear to have initiated at brittle particles (precipitates or
second-phase particles) which are visible in the center of the
voids. Some of the particles themselves appear to be fractured,
an observation previously report by Au[85] for 6061-T6. Complete
fracture has been primarily by normal rupture with evidence of
shearing near the necked or peripheral areas of the voids. There
was essentially no difference in fracture surface for specimens
taken from different stock (see Figure 38). Tuler[86] reported
essentially no change in fracture surface in 6061-T6 for failure
due to slow bending, charpy impact and plate impact.

Several tests were conducted to determine the effect of preshock-
ing on spall behavior. A target was assembled with radial and
rear momentum traps and subjected to a 20 kbar, 0.5 μsec compres-
sive pulse. The recovered specimen was then tested at a velo-
city which caused spall in a specimen that had not been pre-
shocked. Results are compared in Figure 39. Apparently, pre-
shocking has increased the spall fracture strength, since the un-
shocked specimen shows spall fractures while the preshocked spec-
imen does not, for the same test conditions.

74

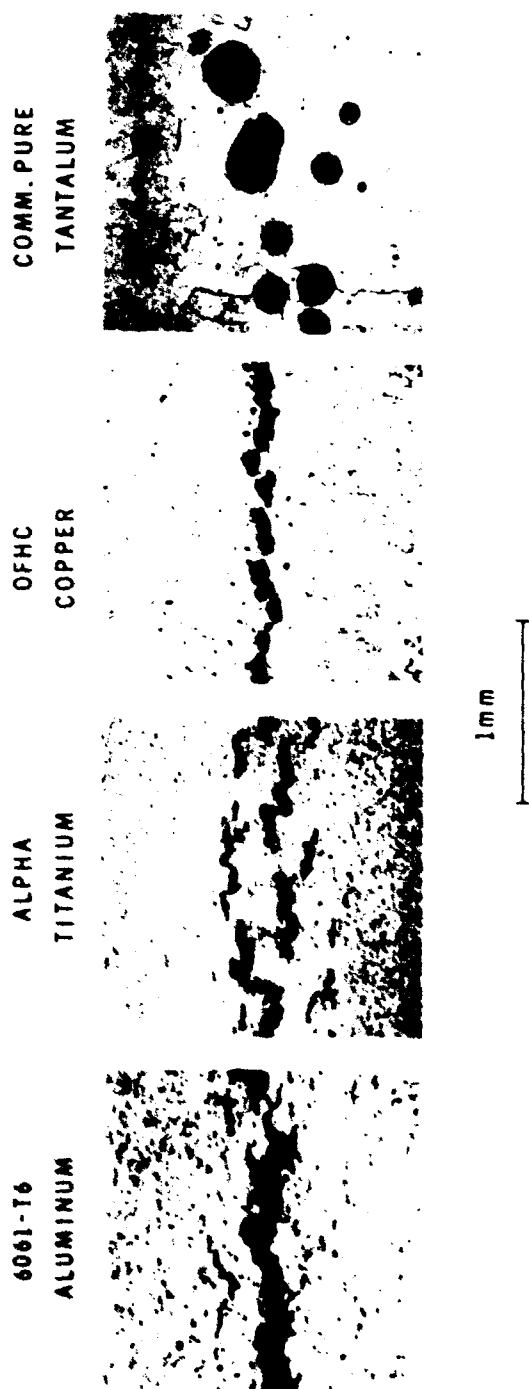Figure 36   Spall Fractures in Metals

100μm   20μm
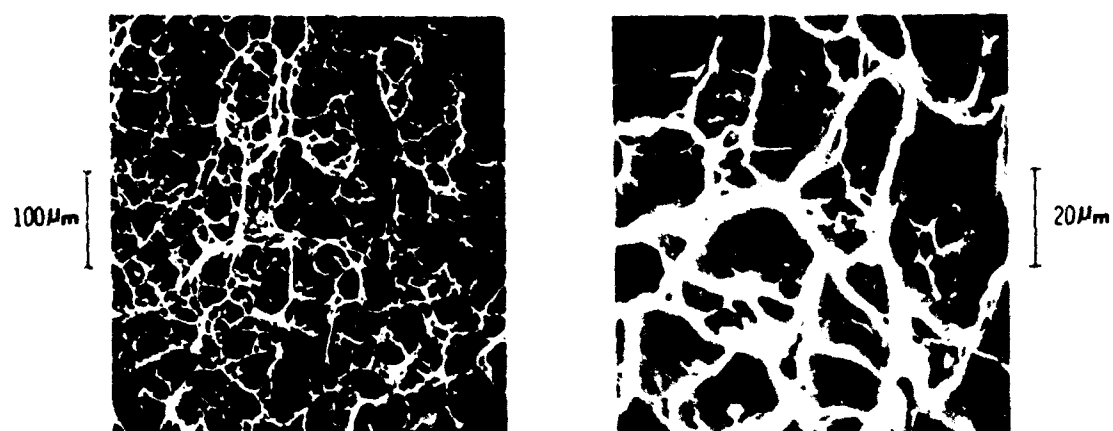
Figure 37   Spall Fracture Surface, 6061-T6 (20°C)

6.4 mm STOCK   12.7 mm STOCK
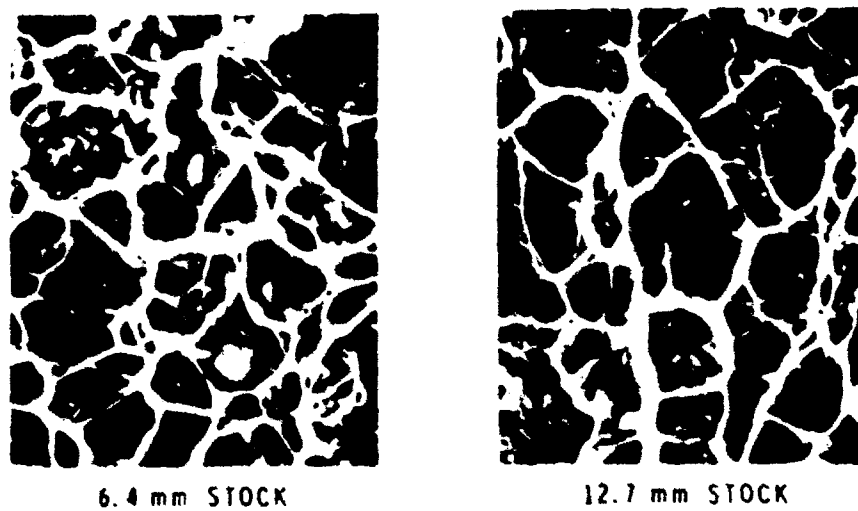
Figure 38   Spall Fracture Surfaces, Material
Effect, 6061-T6 (20°C)

76

NOT PRESHOCKED   PRESHOCKED TO 20 kbars

1 mm
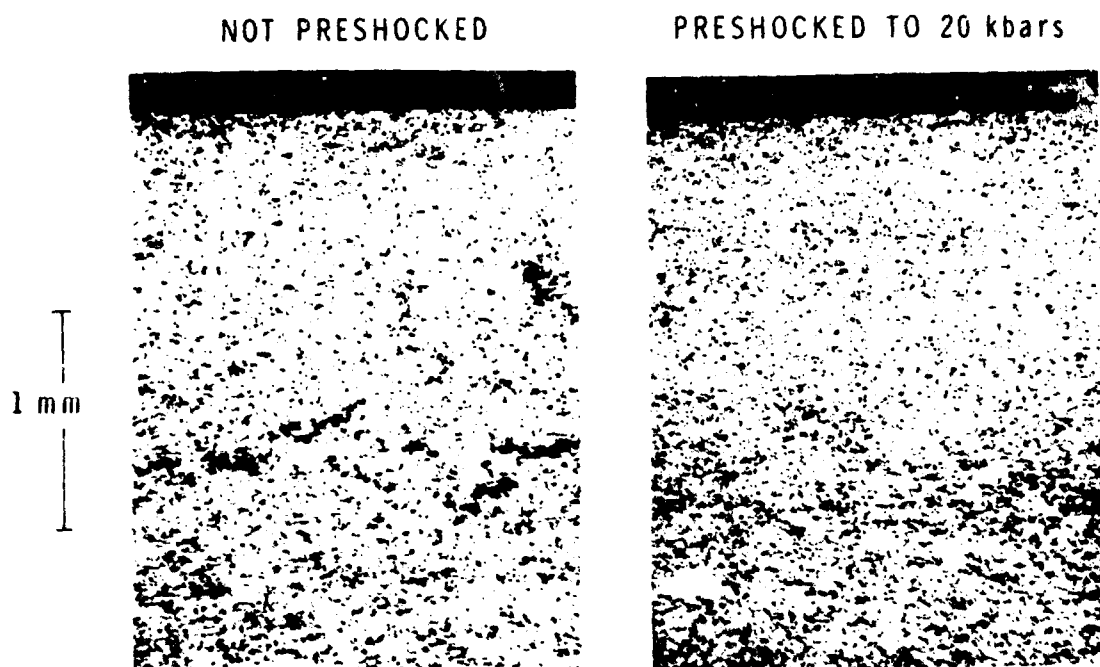
Figure 39   Spall Fractures, Preshocking Effect,
              6061-T6 (20°C)

Stevens and Tuler[87] studied the influence of varying amounts
of precompression on spall fracture by backing the target with
a material of lower impedance (rather than a free rear surface).
They reported that increasing the precompression stress from
12 to 82 kbar did not significantly change the calculated in-
cipient spall tensile stress.

Temperature dependence of spall for 6061 is given in Figure 40.
The impact velocity for incipient spall decreases with increas-
ing temperature. This behavior is probably related to changes
in the dynamic fracture strength of the material. However, as

Figure 40   Spall Data, Temperature Effect, 6061

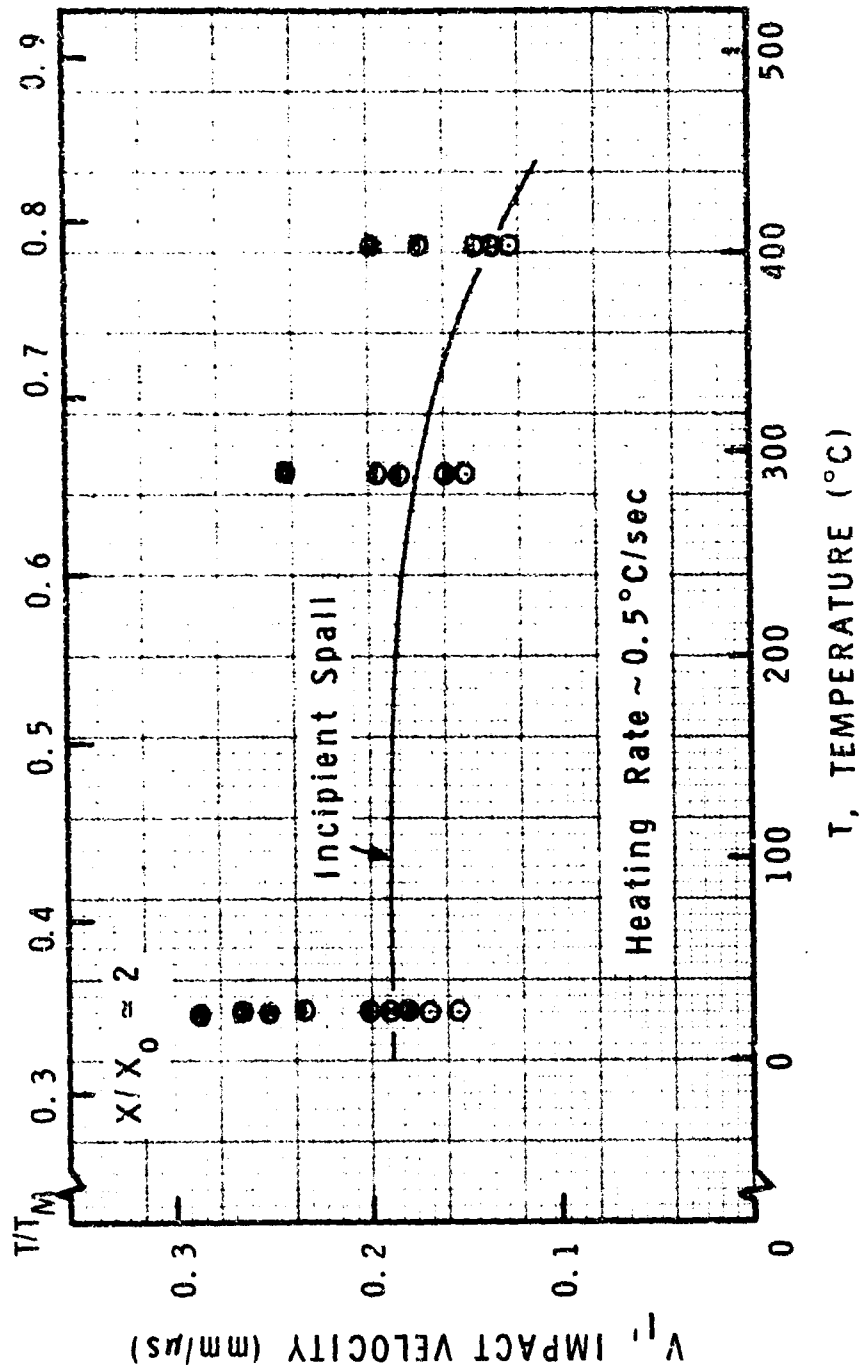Charest has pointed out[88], the use of a room temperature im-
pactor and a hot target (as was done here), gives impedance
differences that influence development of the release wave
structure and therefore stress-time history in the target.
Also, the reduced hugoniot elastic limit in 6061 at elevated
temperature will affect the wave structure in the target.
Optical photomicrographs and scanning microfractographs of 6061
spall specimens tested at several temperatures are shown in
Figures 41 and 42. Although the impact velocity required for
incipient spall and for complete separation has decreased,
there has been no appreciable change in the appearance of voids
or fracture surface.

Several specimens were annealed by heating at 400°C for three
hours and then tested at 20°C. The incipient spall threshold
was ∿ 0.145 mm/μsec or ∿ 25% less than 6061-T6 for the same
thickness. This is comparable to the difference reported by
Butcher[89] for "-T6" and "-0" condition material. Optical
photomicrographs of 6061-0 spall specimens are shown in Fig-
ure 43, and spall fracture surfaces of 6061-0 and 6061-T6 are
compared in Figure 44.

SPALL PROFILES

Spall wave profiles were studied using an aluminum-into-aluminum
configuration, with a free rear surface on the target for com-
plete reflection of the compressive front. A schematic of the
wave interactions resulting from such a test in shown in Fig-
ure 45. Several simplifying assumptions are made. The shock
is shown as a single wave and the release waves originating at
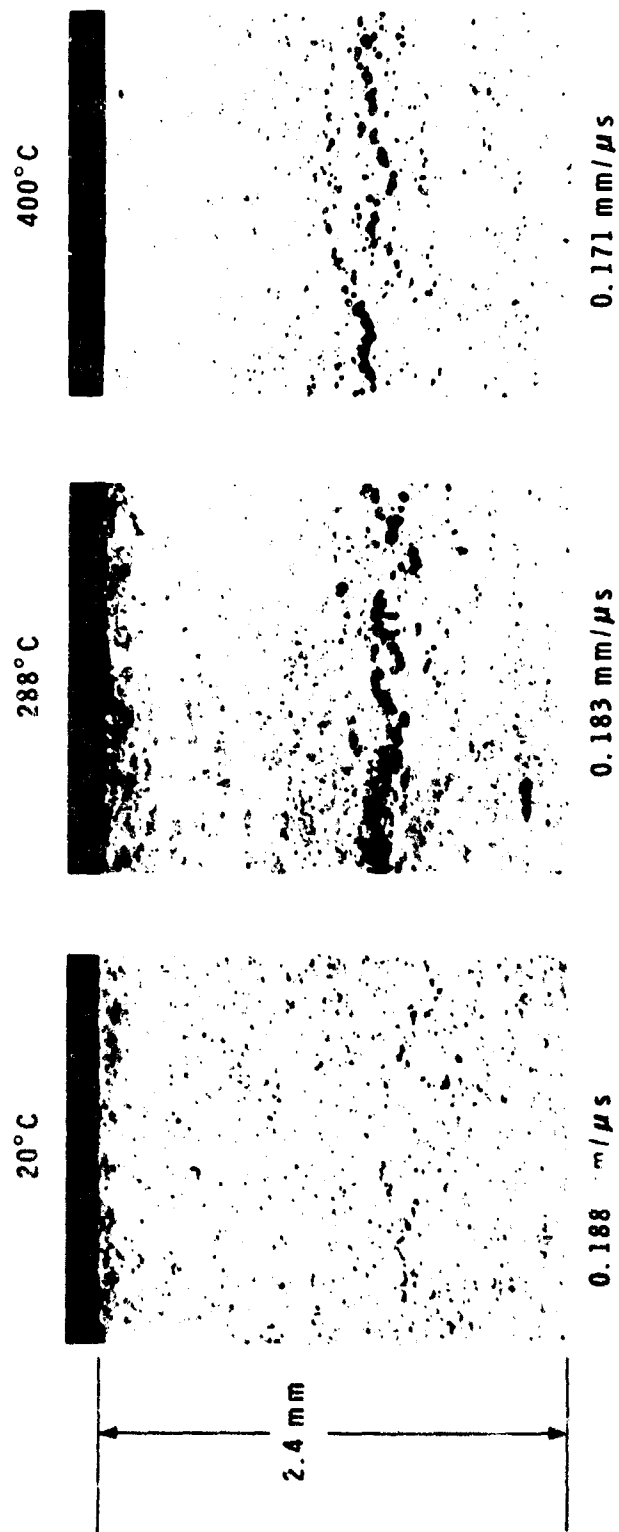boundaries are considered simple, centered rarefaction fans.

Figure 41   Spall Fractures, Temperature Effect, 6061

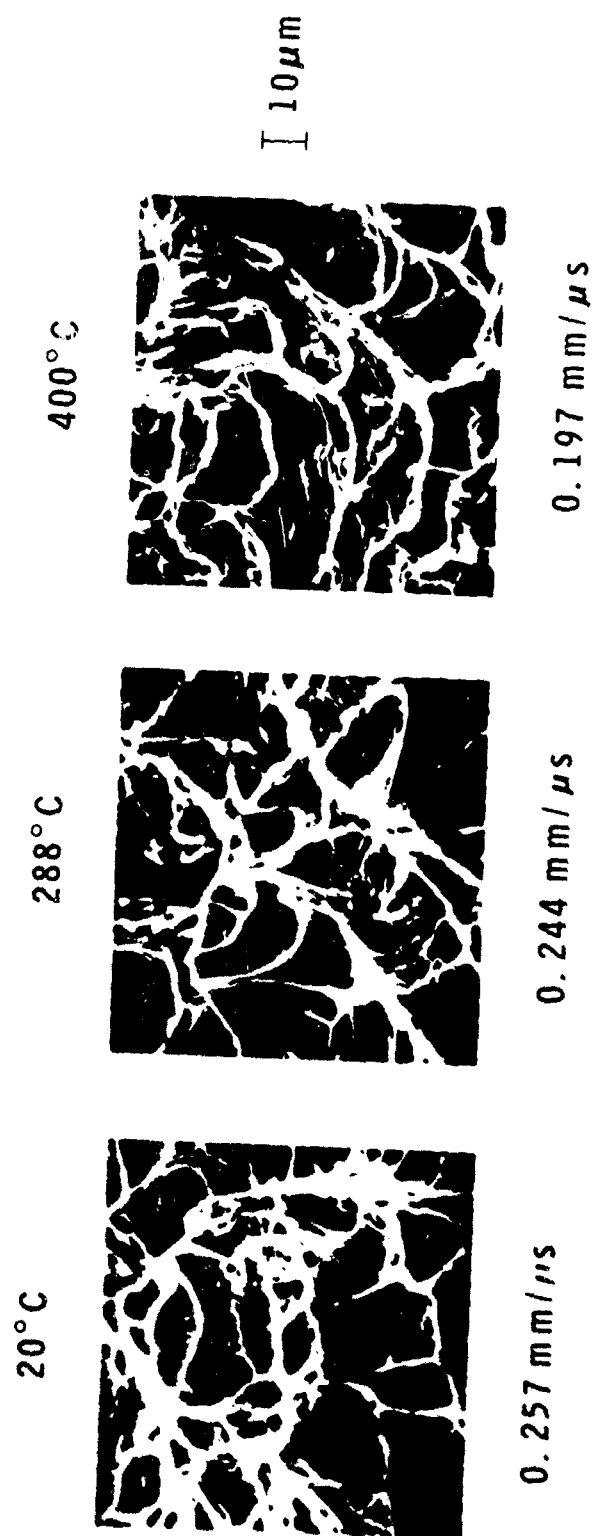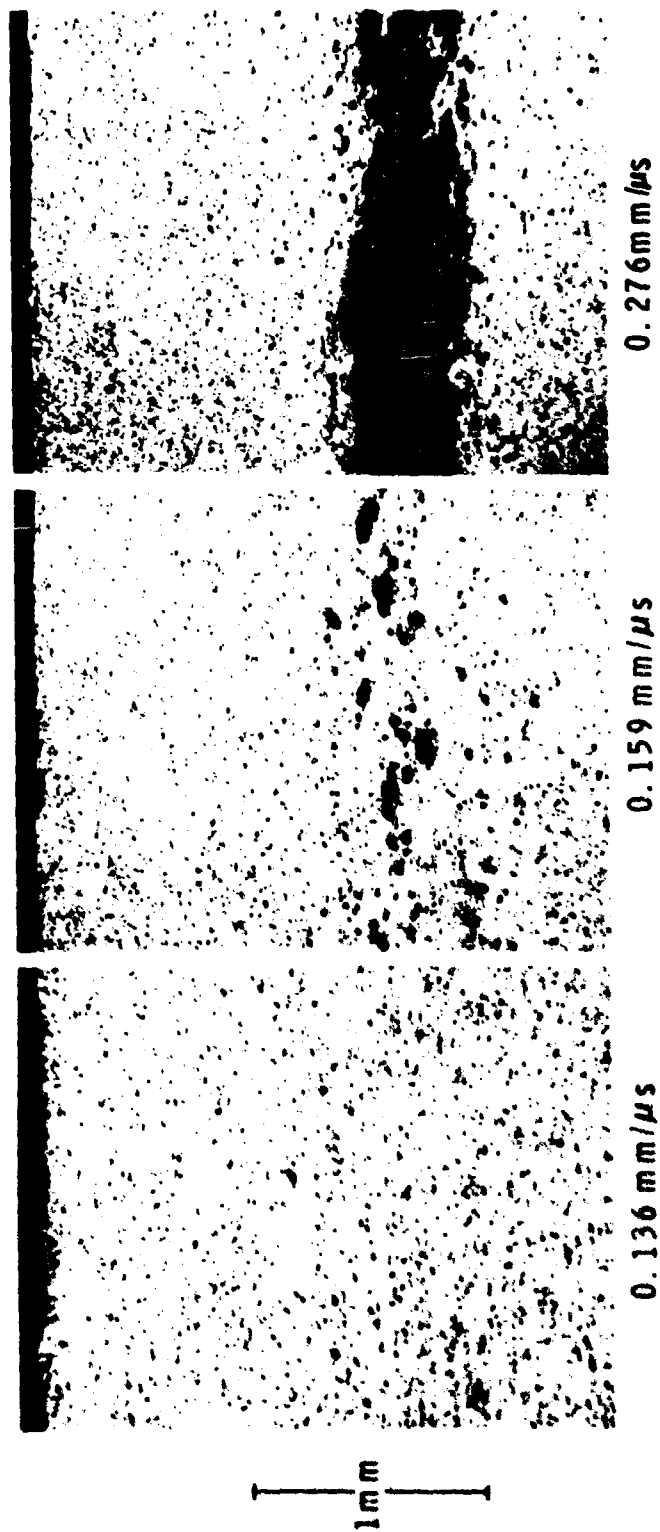Figure 42   Spall Fracture Surfaces, Temperature Effect, 6061

0.276 mm/μs   0.159 mm/μs   0.136 mm/μs

1mm

Figure 43   Spall Fractures, 6061-0 (1.5 mm → 3.0 mm, 20°C)

6061-T6

6061-0

20μm
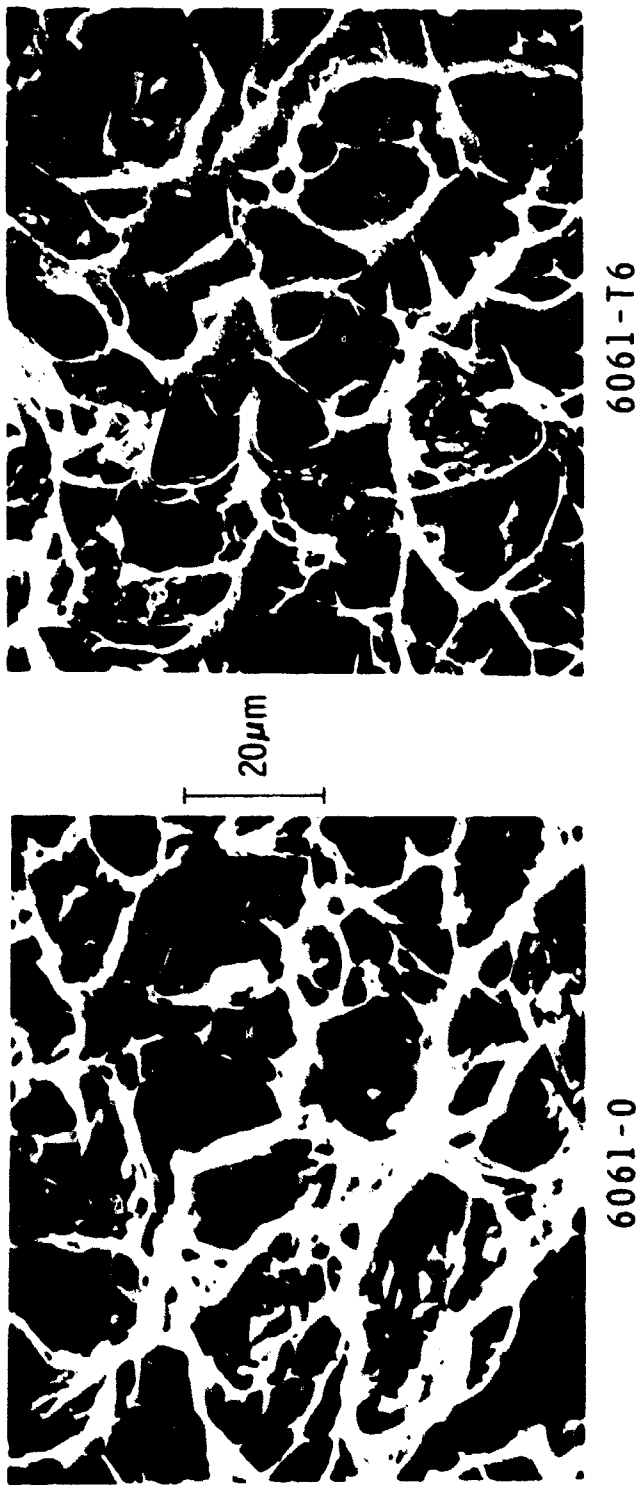
Figure 44   Spall Fracture Surfaces, Annealing Effect
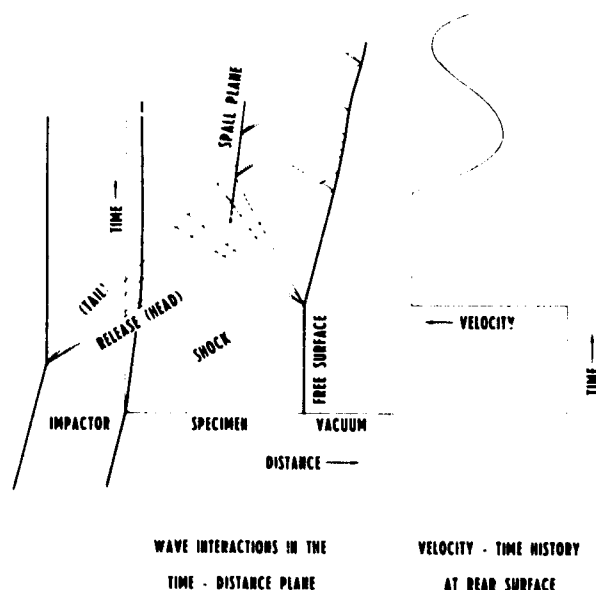
Figure 45   Wave Interaction Schematic, Spall Test

Also, small interactions between shock waves have been omitted.
Fracture of the material is assumed to occur along a single
surface (spall plane) rather than in a volume around this plane
(see Figure 33). Wave interactions at the spall plane are shown
as if the material exhibits a time-dependent fracture, i.e.,
the percentage of fractured area in the spall plane increases
with time until the entire spall surface has separated. During
the early stages of the fracture process, before complete sep-
aration is achieved, waves crossing the spall plane are part-
ially transmitted and partially reflected. After complete
separation has occurred, any waves trapped in the spalled piece
reverberate, giving a sinusoidal motion to the rear surface,
which eventually damps out due to attenuation and dispersion
in the material and to the effects of edge rarefactions.

Measured profiles for unattenuated pulses in 6061-T6 are shown in Figure 46, with photomicrographs of the recovered and sectioned targets. Also shown for reference are the incipient and complete spall levels for this impactor/target combination as determined from the recovery tests. Evidence of fracture in the target is shown as a reversal of the measured release wave. The amount of pullback (decrease in free surface velocity to the point of first reversal) may be related to the tensile strength at the spall plane of the material for a given impact geometry. An empirical relation for this is given by:[90]

$$\sigma_s = \rho C (\Delta u_{fs}/2) \tag{26}$$

where σ_s is tensile strength, ρ and C are local density and longitudinal wave speed, and Δu_{fs} is pullback.

The data in Figure 46 give $\sigma_s \simeq 12$ kbar. This calculated spall strength is not constant for a given material since it is proportional to Δu_{fs} which has been found to change with such factors as pulse width (see Figure 47), target temperature* (see Figure 48), and pulse shape (see Figure 49). These factors are discussed in detail in Reference 92. However, for a given set of impact conditions (thickness, material, temperature), the pullback is relatively insensitive to the maximum compressive stress as well as to the degree of fracture, as shown in Figure 50. This is consistent with the varying-precompression results of Stevens and Tuler[87] referred to earlier.

---

* Brammer[91] reported spall profiles for 2024 Aluminum at 22°C and 371°C which also showed a decrease in pullback at the higher temperature.
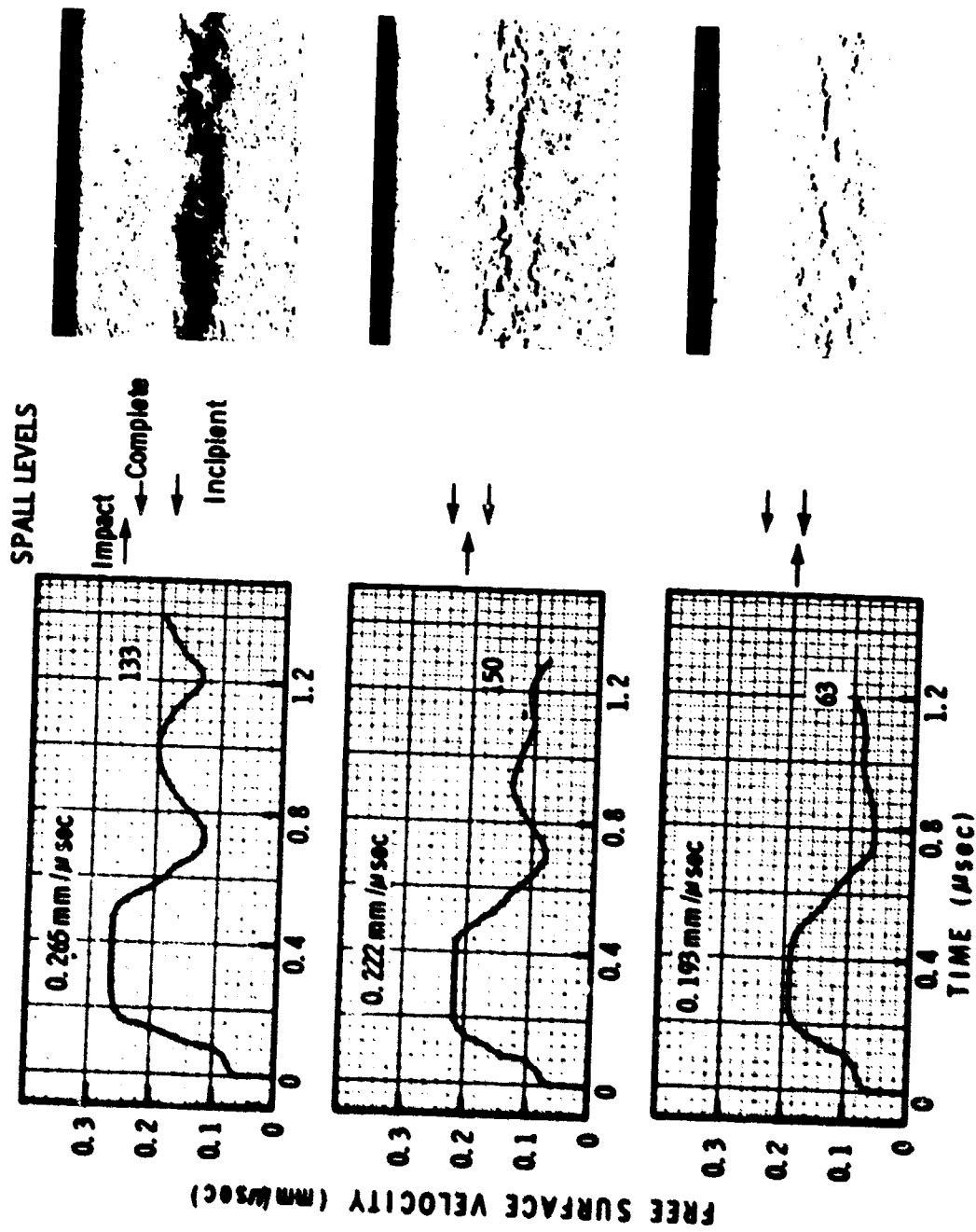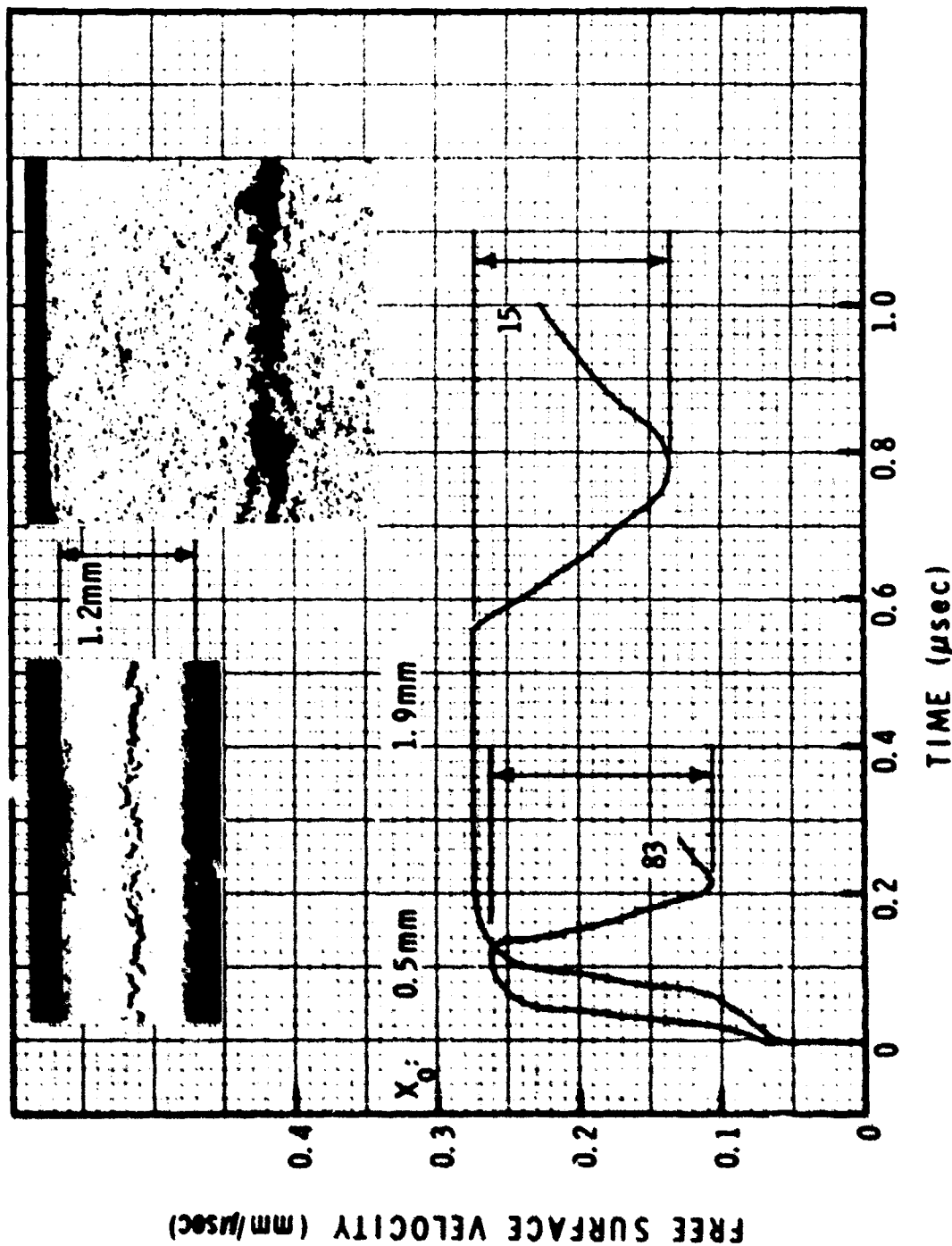
Figure 46   Spall Wave Profiles, 6061-T6

Figure 47   Spall Wave Profiles, Pulse Width Dependence, 6061-T6
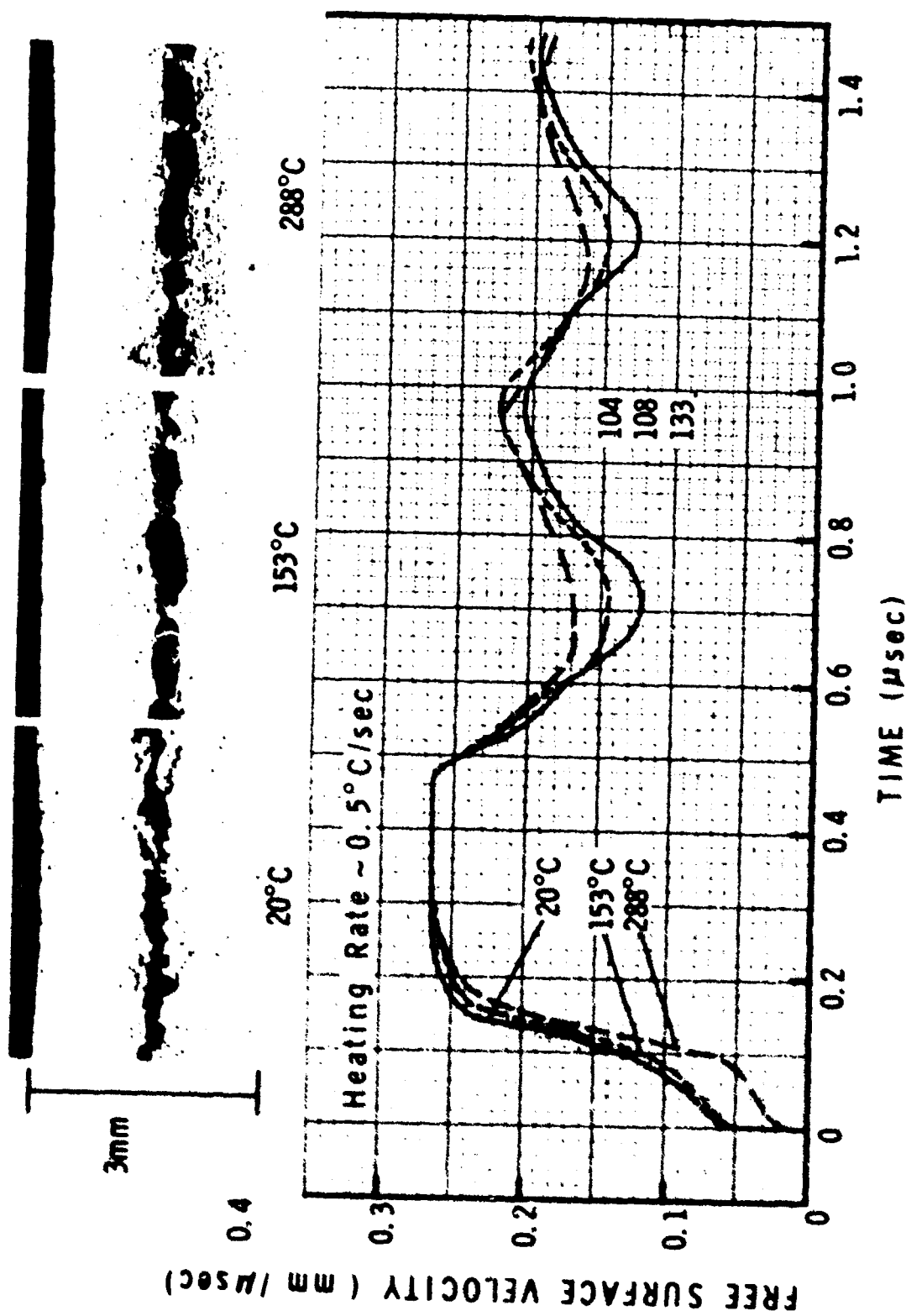
Figure 48   Spall Wave Profiles, Temperature Dependence, 6061
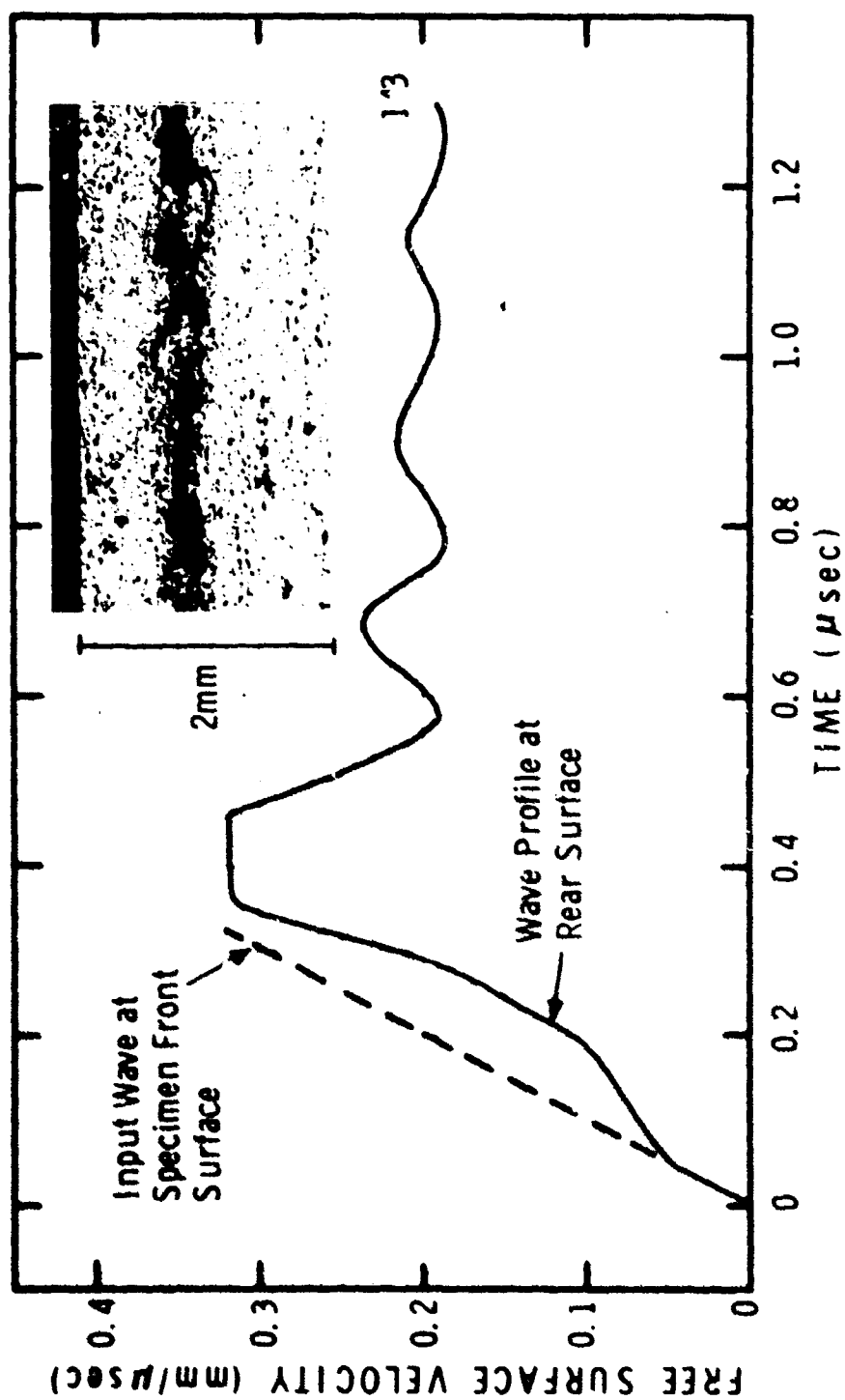
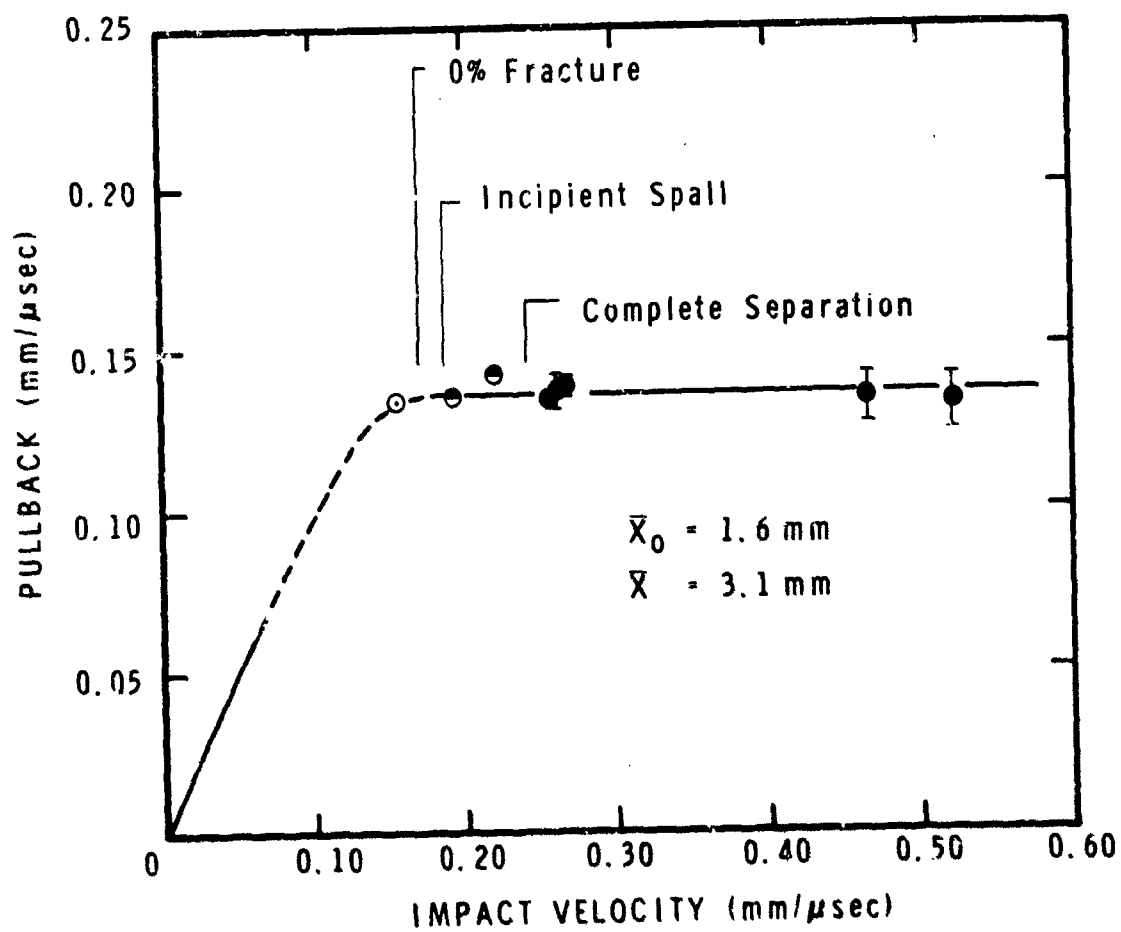Figure 49   Ramped-Wave Spall Profile, 6061-T6

Figure 50   Pullback vs. Impact Velocity, 6061-T6

In the elastic range, pullback equals impact velocity, while
at impact velocities causing fracture, the pullback is approxi-
mately 0.135 mm/µsec (independent of degree of fracture and
maximum stress). Thus, the pullback appears to be associated
with the incipient spall threshold, i.e., the formation and
initial coalescence of voids in the material, rather than with
complete fracture or separation. This conclusion may allow
comparison of the dynamic fracture strength of the material
over a range of wave shapes and times of loading without the
necessity of conducting all tests with exactly the same degree
of final fracture. An additional benefit may result if the
pullback can be related to the results of the recovery-type
measurements of the incipient spall threshold. Then a single
wave profile test could, for a given set of initial conditions,
provide the same incipient threshold data as a series of re-
covery tests. This data could be of use in evaluating various
spall fracture models through comparison of measured shock
wave/spall plane interactions with calculated wave profiles. [93-99]

The influence of spall plane strength was studied with a tar-
get having an "artifical" spall plane of essentially zero
strength. This zero-strength plane was actually the interface
between two target plates bonded together with a thin (< 5 µm)
epoxy layer having a tensile strength of ∿ 0.01 kbars. The
rear target plate was the same thickness as the impactor,
putting the interface at the nominal spall plane. Referring
to Figure 51, for a single wave system the free surface velo-
city would be expected to increase abruptly to the impact velo-
city. The momentum of the impact is simply transferred to the
spall piece. For a two-wave system, the momentum transfer will
again take place. However, the interactions at the interface
are now more complicated and a net tensile stress may develop
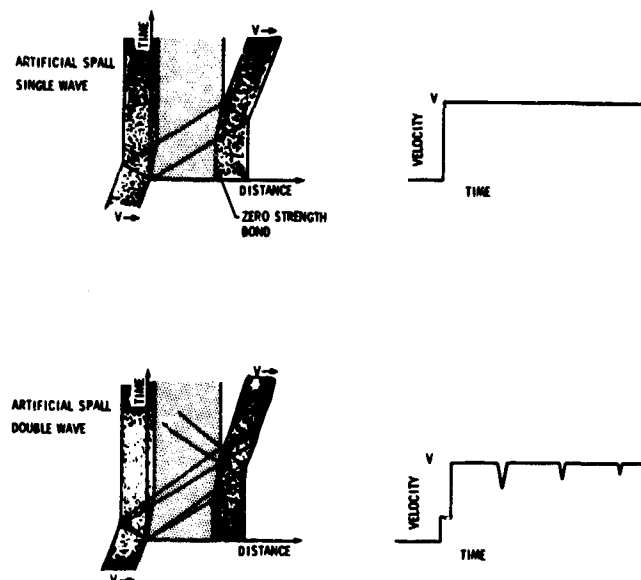
Figure 51   "Zero-Strength" Spall Behavior Schematic

in the spall piece. The pullback at the rear surface shows evidence of this tensile pulse. Figure 52 shows the measured wave profile for such a test. The ringing in the spall piece continues for many microseconds. The damped pullback apparently will decrease to zero amplitude and the piece will continue with approximately impact velocity.

Spall profiles for attenuated pulses, where the time duration of the peak tensile stress is expected to be less than for the unattenuated case, are shown in Figure 53. The pullback for this case is 0.175 mm/μsec, giving a spall strength of ∿ 15 kbar.
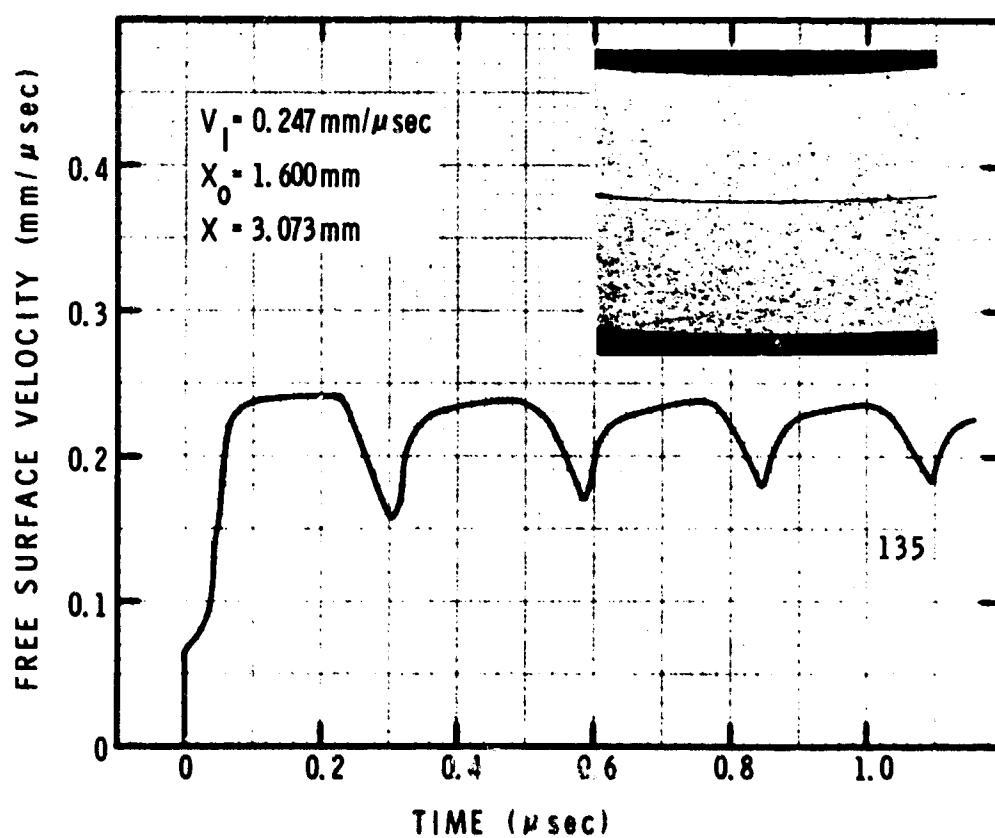
Figure 52   "Zero-Strength" Spall Profile, 6061-T6
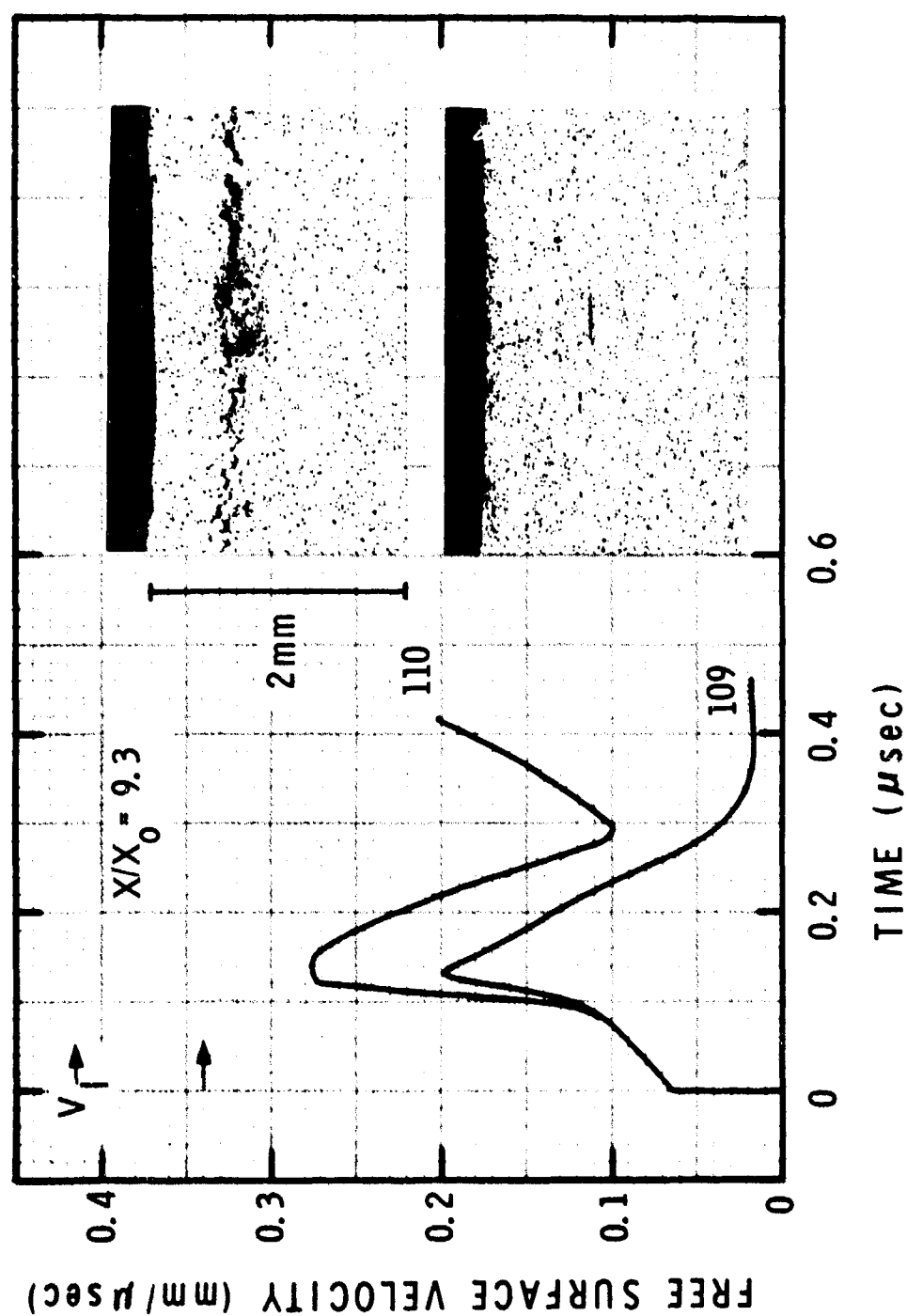
Figure 53   Attenuated Spall Profiles, 6061-T6

SUMMARY

The dynamic properties of 6061-T6 aluminum were measured under
uniaxial stress and uniaxial strain conditions. The material
tested was sheet and plate stock with average hardness of $57R_B$.
Material response to compressive uniaxial stress deformation
showed a well-defined yield with slight strain-hardening.
Strain-rate sensitivity was essentially zero at 20°C (2.9 kbar
yeild) but sensitivty increased and yield decreased at 150,
204 and 288°C, for a range in strain rate of 0.005/sec to
1000/sec.

Longitudinal and shear wave velocities were measured as func-
tions of temperature and pressure, giving the following (in
mm/μsec):

$$C_L = 6.387 - (0.00093T)$$

$$C_L = 3.214 - (0.00084T)$$

(T in °C)

$$C_L = 6.368 + (0.0180P) - (0.0001P^2)$$

$$C_S = 3.197 + (0.0108P) - (0.00005P^2)$$

(P in kbar)

Principal elastic constants were evaluated at T = 20°C and
P = 0, including:

Bulk Modulus = K_0^S = 728 kbar

$$\left(\frac{\partial K^S}{\partial P}\right)_S = 4.60, \quad \left(\frac{\partial K^S}{\partial P}\right)_T = 4.75$$

Shear Modulus = G_0^S = 276 kbar

$$\left(\frac{\partial G^S}{\partial P}\right)_S = 2.12, \qquad \left(\frac{\partial G^S}{\partial P}\right)_T = 2.25$$

Poisson's Ratio = 0.331

Elastic wave velocity data were also used in determining the Gruneisen parameter γ and the Debye temperature θ:

$$\gamma = 1.97 \ @ \ T = 20°C \text{ and } P = 0$$

$$\frac{\partial \gamma}{\partial T} = + \ 0.000051/°C \ @ \ T = 20°C$$

$$\frac{\partial \gamma}{\partial P} = - \ 0.0051/kbar \ @ \ P = 0$$

$$\theta = 420°K$$

The shock wave hugoniot was determined experimentally to be:

$$\sigma_H = 1.0 + 140.4 \ u_p + 37.7 \ u_p^2 \qquad (\sigma_H < 200 \text{ kbar})$$

Assumption of an ideal elastic-plastic wave structure with a 5.7 kbar hugoniot elastic limit and equilibrium initial and final states gave:

$$\sigma_H = 2.3 + 708 \ \mu + 1607\mu^2$$

$$P_H = 708 \ \mu + 1607\mu^2$$

$$U_S = 5.24 + 1.40u_p$$

The hydrostat as determined from elastic constants data was:

$$P_H = 896 \left[(1+\mu)^{1.93} - 1 \right] - 1004 \ln (1+\mu) + 676 \left(\frac{\mu}{1+\mu} \right)^3$$

(Keane equation of state)

Measurements of compressive wave development showed the wave front to be characterized by a well-defined elastic portion and a transition to a spreading plastic wave. Elastic precursor decay was ∿ 75% to 6 kbar after 6 mm of travel. Peak pressure attenuation was ∿ 44% at $X/X_0 = 12.6$ for a 20 kbar, 0.5 μsec pulse, and ∿ 46% at $X/X_0 = 20$ for a 102 kbar, 0.08 μsec pulse.

Spall fracture behavior was determined for several elastic pulse widths ranging from 0.08 to 1.26 μsec. The incipient spall threshold, expressed as impact velocity, increased with decreasing pulse width, and decreased with increasing temperature for 20, 288 and 400°C. The spall plane was reasonably well-defined, and was located approximately one impactor thickness from the target rear surface, for unattenuated pulses. Failure was of a ductile nature with voids initiated at relatively brittle particles.

ACKNOWLEDGMENTS

The authors wish to thank Mr. N. H. Froula and
Mr. A. R. McMillan for contributions to the equation of
state and wave propagation studies, Mr. F. L. Schierloh for
assistance in the strain rate work and Dr. H. Chin for develop-
ment of the data analysis programs. Also the assistance of
the following Materials and Structures Laboratory personnel
in the experimental work is gratefully recognized:
Mr. F. Stemczynski and Mr. E. Stretanski for EOS and wave
profile tests; Mr. J. Havens for ultrasonics measurements;
Mr. C. Woodcock for spall tests; Mr. J. Bonner and
Mr. H. Simmons for strain rate tests; Mr. C. Whitchurch and
Mr. L. Seltz for metallographic work; and Mr. W. Trippen
and Mr. C. Strong for data analysis.

REFERENCES

1. "A Selected Bibliography on Dynamic Properties of Materials", compiled by Christman, D. R., General Motors Corporation, Manufacturing Development, DASA 2511, June 1970 (AD 710823).

2. Alcoa Aluminum Handbook, Aluminum Company of America, Pittsburgh, Pa., 1962.

3. Materials Data Handbook, Aluminum Alloy 6061, Technology Utilization Office, NASA, TSP-10065, 1969 (PB 183426).

4. Metals Handbook, 8th. Ed., Vol. 1: Properties and Selection of Metals, Lyman, T., Ed., American Society for Metals, Metals Park, Ohio, 1961.

5. Handbook of Chemistry and Physics, 45th. Ed., Weast, R. C., Ed., The Chemical Rubber Co., Cleveland, Ohio, 1964.

6. Thermophysical Properties of High Temperature Solid Materials, Vol. 1: Elements, Touloukian, Y. S., Ed., The McMillan Co., New York, N. Y., 1967.

7. Aerospace Structural Metals Handbook, Chapter Code 3206 (ALWT, 6061 Aluminum), Mechanical Properties Data Center, Belfour Stulen Inc., Traverse City, Michigan, 1966.

8. Babcock, S. G., Langan, J. J., Norvey, D. B., Michaels, T. E., Schierloh, F. L. and Green, S. J., "Characterization of Three Aluminum Alloys", General Motors Corporation, Manufacturing Development, AMRC-CR-71-3, January 1971 (AD724195).

9. Milligan, R. V., Koo, W. H. and Davidson, T. E., "The Bauschinger Effect in a High-Strength Steel", ASME Trans. - J. Basic Eng., Ser. D., Vol. 88, p. 480-488, 1966.

10. Milligan, R. V., Private Communication, Watervleit Arsenal, Watervleit, New York, 1970.

11. Buckley, S. N. and Entwistle, K. M., "The Bauschinger Effect in Super-Pure Aluminum Single Crystals and Polycrystals", Acta Met., Vol. 4, p. 352-361, 1956.

12. Babcock, S. G., Kumar, * and Green, S. J., "Response of Materials to Suddenly Applied Stress Loads, Part I: High Strain-Rate Properties of Eleven Reentry-Vehicle Materials at Elevated Temperatures", General Motors Corporation, Manufacturing Development, AFFDL-TR-67-35, Part I, April 1967 (AD 813880).

13. Maiden, C. J. and Green, S. J., "Compressive Strain-Rate Tests on Six Selected Materials at Strain Rates From 10^{-3} to 10^4 In/In/Sec", ASME Trans. - J. Appl. Mech., Ser. E., Vol. 33, p. 496-504, 1966.

14. Holt, D. L., Babcock, S. G., Green, S. J. and Maiden, C. J., "The Strain-Rate Dependence of the Flow Stress in Some Aluminum Alloys", ASM Trans. Quart., Vol. 60, p. 152-159, 1967.

15. Green, S. J., Leasia, J. D., Perkins, R. D. and Maiden, C. J., "Development of Multiaxial Stress High Strain-Rate Techniques", General Motors Corporation, Manufacturing Development, SAMSO-TR-68-71, Vol. III, Jan. 1968 (AD 847163L).

16. Perkins, R. D., Jones, A. H., Green, S. J., Leasia, J. D. and Heimbuch, R. A., "Multiaxial Loading Behavior of Four Materials Including ATJ-S Graphite and RAD-6300 Carbon Phenolic", General Motors Corporation, Manufacturing Development, SAMSO-TR-69-393, Vol. I, Aug. 1970 (AD 874866L).

17. Babcock, S. G. and Hochstein, P. A., "High Strain-Rate Testing of Rapidly Heated Conductive Materials to 7000°F", Exp. Mech., Vol. 10, p. 78-83, 1970.

18. Babcock, S. G., Langan, J. J., Norvey, D. B. and Schierloh, F. L., "Subsequent Yield and High Heating Rate Properties of Two Aluminum Alloys", General Motors Corporation, Manufacturing Development, Materials and Structures Laboratory, MSL-70-24, Sept. 1970.

19. Green, S. J., et al., "Fundamental Material Behavior Study", General Motors Corporation, GM Defense Research Laboratories, BSD-TR-66-398, Oct. 1966 (AD 804889L).

20. Barker, L. M., Lundergan, C. D. and Herrmann, W., "Dynamic Response of Aluminum", J. Appl. Phys., Vol. 35, p. 1203-1212, 1964.

21. Asay, J. R., Urzendowski, S. R. and Guenther, A. J., "Ultrasonic and Thermal Studies of Selected Metals, Laminated Materials and Plastics", Air Force Weapons Laboratory, AFWL-TR-67-91, Jan. 1968 (AD 827596); also, Asay, J. R. and Guenther, A. H., "Ultrasonic Studies of 1060 and 6061-T6 Aluminum", J. Appl. Phys., Vol. 38, p. 4086-4088, 1967.

22. Seaman, L., Williams, R. F., Rosenberg, J. T., Erlich, D. C. and Linde, R. K., "Classification of Materials by Shock Properties", Stanford Research Institute, AFWL-TR-69-96, Nov. 1969 (AD 865505).

23. Johnson, J. N. and Barker, L. M., "Dislocation Dynamics and Steady Plastic Wave Profiles in 6061-T6 Aluminum", J. Appl. Phys., Vol. 40, p. 4321-4334, 1969.

24. Toupin, R. A. and Bernstein, B., "Sound Waves in Deformed Perfectly Elastic Materials, Acoustoelastic Effect", Ac. Soc. Am. J., Vol. 33, p. 216-225, 1961.

25. Gerlich, D. and Fisher, E. S., "The High Temperature Elastic Moduli of Aluminum", J. Phys. Chem. Solids, Vol. 30, p. 1197-1205, 1969.

26. Thomas, J. F., "Third-Order Elastic Constants of Aluminum", Phys. Rev., Vol. 175. p. 955-962, 1968.

27. Ho, P. S. and Ruoff, A. L., "Pressure Dependence of the Elastic Constants for Aluminum from 77° to 300°K", J. Appl. Phys., Vol. 40, p. 3151-3156, 1969.

28. Kolsky, H., Stress Waves in Solids, S1098, Dover Publications, Inc., New York, N. Y. 1963.

29. Mason, W. P., "Acoustic Properties of Solids", American Institute of Physics Handbook, 2nd. Ed., p. 3-28. 3-97, 1963.

30. Barsch, G. R. and Chang, Z. P., "Adiabatic, Isothermal, and Intermediate Pressure Derivatives of the Elastic Constants for Cubic Symmetry", Phy. Stat. Sol., Vol. 19, p. 129-151, 1967.

31. Anderson, O. L., "Elastic Constants Under Pressure", Lamont Geological Observatory, 1968 (PB 182479).

32. Walsh, J. M., Rice, M. H., McQueen, R. G. and Yarger, F. L., "Shock-Wave Compressions of Twenty-Seven Metals, Equation of State of Metals", Phys. Rev., Vol. 108, p. 196-216, 1957.

33. Gschneidner, K. A., "Physical Properties and Interrelationships of Metallic and Semimetallic Elements", Solid State Physics, Vol. 16, p. 275-426, 1964.

34. Huang, Y. K., "Direct Method of Calculating the Gruneisen Parameter γ Based on Shock-Wave Measurements of Metals", J. Chem. Phys., Vol. 51, p. 2573-2577, 1969.

35. Slater, J. C., Introduction to Chemical Physics, McGraw-Hill Book Co., New York, N. Y., 1939.

36. Dugdale, J. S. and MacDonald, D. K. C., "The Thermal Expansion of Solids", Phys. Rev., Vol. 89, p. 832-834, 1953.

37. Schreiber, E. and Anderson, O. L., "Pressure Derivatives of the Sound Velocities of Polycrystalline Alumina", Am. Ceram. Soc. J., Vol. 49, p. 184-190, 1966.

38. Anderson, O. L. and Dienes, G. J., Non-Crystalline Solids (Chapter 18), Ed. by Frechette, V. D., John Wiley and Sons, New York, 1960.

39. Schuele, D. E. and Smith, C. S., "Low Temperature Thermal Expansion of RbI", J. Phys. Chem. Solids, Vol. 25, p. 801-814, 1964.

40. Herbstein, F. H., "Methods of Measuring Debye Temperature and Comparisons of Results for Some Cubic Crystals", Adv. Phys., Vol. 10, p 313-355, 1961.

41. Anderson, O. L., "A Simplified Method for Calculating the Debye Temperature from Elastic Constants", J. Phys. Chem. Solids, Vol. 24, p. 909-917, 1963.

42. Alers, G. A., "Use of Sound Velocity Measurements in Determining the Debye Temperature of Solids", Physical Acoustics, Vol. III, Part B (Lattice Dynamics), Academic Press, New York, N. Y., p. 1-42, 1965.

43. Sutton, P. M., "The Variation of the Elastic Constants of Crystalline Aluminum with Temperature between 63°K and 773°K", Phys. Rev., Vol. 91, p. 816-821, 1953 and Phys. Rev., Vol. 112, p. 2139, 1958.

44. Rice, M. H., McQueen, R. G. and Walsh, J. M., "Compression of Solids by Strong Shock Waves", Solid State Physics, Vol. 6, p. 1-63, 1958.

45. Al'tshuler, L. V., "Use of Shock Waves in High-Pressure Physics", Sov. Phys. Uspekhi, Vol. 8, p. 52-91, 1965.

46. Goodwin, L. K., Johnson, L. A. and Wright, R. S., "An Equation of State for Metals", Philco-Ford Corporation, Aeronutronic Division, DASA-2286, April 1969 (AD 858302).

47. Munson, D. E. and Barker, L. M., "Dynamically Determined Pressure-Volume, Relationships for Aluminum, Copper and Lead", J. Appl. Phys., Vol. 37, p. 1652-1660, 1966.

48. McQueen, R. G., Marsh, S. P., Taylor, J. W., Fritz, J. N. and Carter, W. J., "The Equation of State of Solids from Shock Wave Studies", High-Velocity Impact Phenomena, p. 293-417, Academic Press, New York, N. Y., 1970.

49. Jones, A. H., Maiden, C. J. and Isbell, W. M., "The Effect of High-Pressure Shock Waves on Metals: Mechanical and Metallurgical Behavior", Mechanical Behavior of Materials Under Pressure, Pugh, H. Ll. D., Ed., p. 680-747, Elsevier Publishing Co., New York, 1970.

50. Chin, H. C., "A Computer Program to Analyze X-Cut Quartz Data Obtained from Shock Loading", General Motors Corporation, Manufacturing Development, Materials and Structures Laboratory, MSL-70-15, June, 1970.

51. Lundergan, C. D. and Herrmann, W., "Equation of State of 6061-T6 Aluminum at Low Pressures", J. Appl. Phys., Vol. 34, p. 2046-2052, 1963.

52. Froula, N. H., Unpublished Data, General Motors Corporation, Manufacturing Development, 1969.

53. Overton, W. C., "Relation Between Ultrasonically Measured Properties and the Coefficients in the Solid Equation of State", J. Chem. Phys., Vol. 37, p. 116-119, 1962.

54. Swenson, C. A., "Equation of State of Cubic Solids; Some Generalizations", J. Phys. Chem. Solids, Vol. 29, p. 1337-1348, 1968.

55. Anderson, O. L., "The Use of Ultrasonic Measurements Under Modest Pressures to Estimate Compression at High Pressures", J. Phys. Chem. Solids, Vol. 27, p. 547-565, 1966.

56. Lamberson, D. L., "The High Pressure Equation of State of Tantalum, Polystyrene and Carbon Phenolic Determined from Ultrasonic Velocities", Doctoral Dissertation, Air Force Institute of Technology (AFIT-SE), Wright-Patterson AFB, Ohio, March, 1969.

57. MacDonald, J. R., "Review of Some Experimental and Analytical Equations of State", Rev. Mod. Phys., Vol. 41, p. 316-349, 1969.

58. Birch, F., "The Effect of Pressure Upon the Elastic Parameters of Isotropic Solids, According to Murnaghan's Theory of Finite Strain", J. Appl. Phys., Vol. 9, p. 279-288, 1938.

59. Birch, F., "Elasticity and Constitution of the Earth's Interior", J. Geophys. Res., Vol. 57, p. 227-286, 1952.

60. Murnaghan, F. D., "The Compressibility of Media Under Extreme Pressures", Proc. Nat. Ac. Sci., Vol. 30, p. 244-247, 1944.

61. Keane, A., "An Investigation of Finite Strain in an Isotropic Material Subjected to Hydrostatic Pressure and Its Seismological Applications", Australian J. Phys., Vol. 7, p. 323-333, 1954.

62. Anderson, O. L., "On the Use of Ultrasonic and Shock-Wave Data to Estimate Compressions at Extremely High Pressures", Phys. Earth Planet. Interiors, Vol. 1, p. 169-176, 1968.

63. Duvall, G. E. and Zwolinski, B. J., "Entropic Equations of State and Their Applications to Shock Wave Phenomena in Solids", Acoust. Soc. Am. J., Vol. 27, p. 1054-1058, 1955.

64. Zel'dovich, Y. B. and Raizer, Y. P., Physics of Shock Waves and High-Temperature Hydrodynamic Phenomena, Vol. II, Academic Press, New York, N. Y., p. 688-709, 1967.

65. Ruoff, A. L., "Linear Shock-Velocity-Particle-Velocity Relationship", J. Appl. Phys., Vol. 38, p. 4976-4980, 1967.

66. Vaidya, S. N. and Kennedy, G. C., "Compressibility of 18 Metals to 45 kbar", J. Phys. Chem. Solids, Vol. 31, p. 2329-2345, 1970.

67. Herrmann, W., "Nonlinear Stress Waves in Metals", Wave Propagation in Solids, Miklowitz, J., Ed., p. 129-183, American Society of Mechanical Engineers, 1969.

68. Chang, H. L. and Horie, Y., "An Analysis of Plane Shock-Structures in 6061-T6 Aluminum", North Carolina State University, TR-71-1, Feb. 1971 (AD 720716).

69. Johnson, J. N., "Constitutive Relation for Rate-Dependent Plastic Flow in Polycrystalline Metals", J. Appl. Phys., Vol. 40, p. 2287-2293, 1969.

70. Read, H. E., Triplett, J. R. and Cecil, R. A., "Dislocation Dynamics and the Formulation of Constitutive Equations for Rate Dependent Plastic Flow in Metals", Systems, Science, and Software, DASA 2638, Dec. 1970 (AD 722314).

71. Taylor, J. W., "Dislocation Dynamics and Dynamic Yielding", J. Appl. Phys., Vol. 36, p. 3146-3150, 1965.

72. Gilman, J. J., "Dislocation Dynamics and the Response of Materials to Impact", Appl. Mech. Rev., Vol. 21, p. 767-783, 1968.

73. McMillan, A. R., Isbell, W. M. and Jones, A. H., "High Pressure Shock Wave Attenuation", General Motors Corporation, Manufacturing Development, DASA 2425, June 1971.

74. Butcher, B. M., Barker, L. M., Munson, D. E. and Lundergan, C. D., "Influence of Stress History on Time-Dependent Spall in Metals", AIAA J., Vol. 2, p. 977-990, 1964.

75. Oscarson, J. H. and Graff, K. F., "Spall Fracture and Dynamic Response of Materials", Battelle Memorial Institute, BAT-197A-4-3, 21 March 1968 (AD 669440).

76. Charest, J. A., Horne, D. E. and Jenrette, B. D., "Phenomenological Considerations for Spall Measurements", E,G&G, Santa Barbara Division, S-56-TP, Jan. 1970.

77. Kreer, J. R., "Dynamic Fracture in 6061-T6 Aluminum", Air Force Weapons Laboratory, AFWL-TR-70-180, Jan. 1971 (AD 881534L).

78. Keller, D. V. and Tuler, F. R., "Predix Metals Report", (Preliminary Draft), Effects Technology, Inc., CR-70-06, 1970.

79. Jajosky, C. and Ferdman, M. A., "Spall Studies on 6061-T6 Aluminum, Air Force Weapons Laboratory, AFWL-TR-69-101, Sept. 1969 (AD 860078).

80. Cohen, L. J. and Berkowitz, H. M., "Time-Dependent Fracture Criteria for 6061-T6 Aluminum Under Stress-Wave Loading in Uniaxial Strain", McDonnell Douglas Astronautics Company, Western Division, Douglas Paper 10191, Nov. 1969.

81. Stefansky, T. and Shea, J. H., "Dynamic Fracture Experiments Using High-Energy Pulsed Electron Beams", Physics International Co., DASA 2699, July 1971 (AD727983).

82. Christman, D. R., Michaels, T. E., Isbell, W. M. and Babcock, S. G., "Measurements of Dynamic Properties of Materials, Vol. IV: Alpha Titanium", General Motors Corporation, Manufacturing Development, DASA 2501-4, 1971.

83. Isbell, W. M., Christman, D. R. and Babcock, S. G., "Measurements of Dynamic Properties of Materials, Vol. VI: Tantalum", General Motors Corporation, Manufacturing Development, DASA 2501-6, 1971.

84. Christman, D. R., Isbell, W. M. and Babcock, S. G., "Measurements of Dynamic Properties of Materials, Vol. V: OFHC Copper", General Motors Corporation, Manufacturing Development, DASA 2501-5, 1971.

85. Au, R. H. C., "Nucleating Mechanisms for Spall in Aluminum", _AIAA J._, Vol. 8, p. 1171-1173, 1970.

86. Tuler, F. R., "Fracture Surface Observations in 6061-T6 Aluminum at Different Strain Rates", Sandia Laboratories, SC-DR-68-497, Oct. 1968.

87. Stevens, A. L. and Tuler, F. R., "The Effect of Precompression on the Dynamic Fracture Strength of 1020 Steel and 6061-T6 Aluminum", Sandia Laboratories, to be published.

88. Charest, J. A., "Spall Compendium", E,G&G, Santa Barbara Division, 1971.

89. Butcher, B. M., "Spallation in 6061-T6 Aluminum", _Behavior of Dense Media Under High Dynamic Pressures_, Gordon and Breach, New York, N. Y., p. 245-250, 1968.

90. Taylor, J. W., "Stress Wave Profiles in Several Metals", _Dislocation Dynamics_, p. 573-589, McGraw-Hill Book Co., New York, N. Y., 1968.

91. Brammer, J. A., "Temperature Influence on the Shock Response of 2024 Aluminum", Sandia Laboratories, SC-RR-70-124, March 1970.

92. Isbell, W. M. and Christman, D. R., "Shock Propagation and Fracture in 6061-T6 Aluminum from Wave Profile Measurements", General Motors Corporation, Manufacturing Development, DASA 2419, April 1970 (AD 705536).

93. Al'tshuler, L. V., Novikov, S. A. and Divnov, I. I.,
"The Relationship Between the Critical Breaking Stress
and the Time of Failure as a Result of the Explosive
Stressing of Metals", Sov. Phys.-Doklady, Vol. 11,
p. 79-82, 1966.

94. Thurston, R. S. and Mudd, W. L., "Spallation Criteria
for Numerical Calculation", Los Alamos Scientific Labora-
tory, LA-4013, Sept., 1968.

95. Tuler, F. R. and Butcher, B. M., "A Criterion for the
Time Dependence of Dynamic Fracture", Int. J. Fract. Mech.,
Vol. 4, p. 431-437, 1968.

96. Field, F. A., "A Simple Crack Extension Criterion for Time
Dependent Spallation", Aerospace Corporation, SAMSO-TR-69-
405, 20 Oct., 1969 (AD 863205).

97. Barbee, T., Seaman, L. and Crewdson, R. C., "Dynamic Frac-
ture Criteria of Homogeneous Materials", Stanford Research
Institute, AFWL-TR-70-99, Nov., 1970.

98. Butcher, B. M. and Young, E. G., "A Critical Evaluation
of 6061-T6 Spall Data", Sandia Laboratories, SC-DR-710173,
May, 1971.

APPENDIX A

ELASTIC CONSTANTS EQUATIONS

Following are the equations used in calculating various elastic constants and the adiabatic and isothermal pressure and temperature derivatives of the bulk and shear modulii (K and G)[*]:

$$C_B = \sqrt{C_L{}^2 - 4/3\ C_S{}^2}$$

(Bulk Wave Velocity)

$$C_E = \sqrt{2(1+\nu)\ C_S{}^2}$$

(Sound wave velocity, longitudinal
wave of infinite wave length in
bar, lateral displacement allowed)

$$C_R: \quad k_1^6 - 8k_1^4 + (24-16\alpha_1{}^2)k_1{}^2 + (16\alpha_1{}^2 - 16) = 0$$

where $k_1^2 = (C_R/C_S)^2$, $\alpha_1{}^2 = (C_S/C_L)^2$

(Rayleigh or Surface Wave Velocity)

---

[*] The expressions for the pressure derivatives are simplified in these equations, e.g.,

$$K_{0S}^{S'} = \left(\frac{\partial K^S}{\partial P}\right)_S \bigg|_{P=0}.$$

$$\nu = [0.5 - (C_S/C_L)^2]/[1.0 - (C_S/C_L)^2]$$

(Poisson's Ratio)

$$K = \rho C_B^2 = \rho (C_L^2 - 4/3 C_S^2)$$

(Bulk Modulus)

$$G = \rho C_S^2$$

(Shear or Rigidity Modulus)

$$E = 2\rho (1+\nu) C_S^2$$

(Young's or Elastic Modulus)

$$\lambda = 2\rho\nu C_S^2/(1-2\nu)$$

(Lamé's Parameter)

$$K_0^T = \frac{K_0^S}{1 + \beta\gamma_0 T}$$

where $\gamma_0 = \dfrac{\beta K_0^S}{\rho_0 c_p}$

$$K_{0S}^{S'} = K_{0T}^{S'} + \left(\frac{\partial K^S}{\partial T}\right)_0 \left(\frac{\gamma_0 T}{K_0^S}\right)$$

$$K_{0T}^{T'} = K_{0T}^{S'} + \beta\gamma_0 T \left(\frac{K_0^T}{K_0^S}\right) \left[1 - \frac{2}{\beta K_0^T}\left(\frac{\partial K^T}{\partial T}\right)_0 - 2K_{0T}^{S'}\right]$$

$$+ \left[\beta\gamma_0 T\left(\frac{K_0^T}{K_0^S}\right)\right]^2 \left[K_{0T}^{S'} - 1 - \frac{1}{\beta^2}\left(\frac{\partial\beta}{\partial T}\right)_0\right]$$

$$K_{0S}^{T'} = K_{0T}^{T'} + \left(\frac{\partial K^T}{\partial T}\right)_0 \left(\frac{\gamma_0 T}{K_0^S}\right)$$

$$\left(\frac{\partial K^S}{\partial T}\right)_S = \left(\frac{\partial K^S}{\partial T}\right)_0 + K_{0T}^{S'}\left(\frac{K_0^S}{\gamma_0 T}\right)$$

$$\left(\frac{\partial K^T}{\partial T}\right)_0 = \frac{\left(\frac{\partial K^S}{\partial T}\right)_0 - \beta\gamma_0 K_0^T - \beta T K_0^T\left(\frac{\partial\gamma}{\partial T}\right)_0 - \gamma_0 T K_0^T\left(\frac{\partial\beta}{\partial T}\right)_0}{(1+\beta\gamma_0 T)}$$

$$\left(\frac{\partial K^T}{\partial T}\right)_S = \left(\frac{\partial K^T}{\partial T}\right)_0 + K_{0T}^{T'}\left(\frac{K_0^S}{\gamma_0 T}\right)$$

$$G_0^T = G_0^S = G_0$$

$$G_{0T}^{T'} = G_{0T}^{S'} = G_{0T}'$$

$$G'_{0S} = G'_{0T} + \left(\frac{\partial G}{\partial T} \right)_0 \left(\frac{\gamma_0 T}{K_0^S} \right)$$

$$\left(\frac{\partial G}{\partial T} \right)_S = \left(\frac{\partial G}{\partial T} \right)_0 + G'_{0T} \left(\frac{K_0^S}{\gamma_0 T} \right)$$

APPENDIX B

GRUNEISEN PARAMETER ESTIMATES

1. The Gruneisen parameter is defined thermodynamically as

$$\gamma = \frac{1}{\rho c_p} \left(\frac{\partial V}{\partial T} \right)_P \left(\frac{\partial P}{\partial V} \right)_S = \frac{\beta K^S}{\rho c_p}$$

For an isotropic elastic solid, this becomes

$$\gamma = \frac{\beta}{c_p} \left(C_L{}^2 - \frac{4}{3} C_S{}^2 \right)$$

Substituting appropriate values for aluminum gives

$$\gamma_0 = 1.97$$

2. Slater developed a relation that was an extension of the Debye Theory for a three-dimensional continuum, and assumed Poisson's ratio was independent of volume and γ is the same for all vibrational frequencies:

$$\gamma = - \frac{V}{2} \left(\frac{\partial^2 P / \partial V^2}{\partial P / \partial V} \right) - \frac{2}{3}$$

which simplifies at zero pressure to

$$\gamma_0 = \frac{1}{2} \left(K_{0S}^{S'} - \frac{1}{3} \right) = 2S - \frac{2}{3}$$

where S is from $U_S = C_B + Su_p$.

Ultrasonic data gives S = 1.40 and γ = 2.13.

Shock wave data gives S = 1.4 and γ = 2.13.

3. Dugdale and MacDonald give an expression for plane wave velocity vs. volume in a three-dimensional continuum that leads to an expression for γ differing from Slater's by a constant (1/3):

$$\gamma = -\frac{V}{2} \left(\frac{\partial^2 P/\partial V^2}{\partial P/\partial V} \right) - 1$$

which simplifies at zero pressure to

$$\gamma_0 = \frac{1}{2} \left(K_{0S}^{S'} - 1 \right) = 2S - 1$$

Both ultrasonic and shock wave data give γ = 1.80.

4. Anderson and Dienes give expressions for γ in terms of the longitudinal and shear modes of wave propagation:

$$\gamma_L = \frac{1}{3} + \frac{K_0^{T}}{C_L} \left(\frac{dC_L}{dP} \right)_0$$

$$\gamma_S = \frac{1}{3} + \frac{K_0^{T}}{C_S} \left(\frac{dC_S}{dP} \right)_0$$

Ultrasonic data gives γ_L = 2.31 and γ_S = 2.70.

5. Schuele and Smith give expressions for the "low-temperature" and "high-temperature" Gruneisen ratio, where low-temperature is the range in which it is assumed the solid behaves as a continuum and high-temperature is the range where all vibrational modes are excited and γ is constant:

$$\gamma_{LT} = \frac{1}{2+\varepsilon^3} \left(\varepsilon^3 \gamma_L + 2\gamma_S \right)$$

$$(\varepsilon = C_S/C_L)$$

$$\gamma_{HT} = \frac{1}{3} \left(\gamma_L = 2\gamma_S \right)$$

Using ultrasonic data and γ_L and γ_S from above gives $\gamma_{LT} = 2.68$ and $\gamma_{HT} = 2.57$.

6. Perry calculated the Grueisen parameter from laser inter-ferometer data obtained for electron beam energy deposi-tion.[*] For polycrystalline aluminum, he obtained $\gamma = 2.02$ assuming instantaneous deposition and $\gamma = 2.11$ assuming 50 nsec deposition time.

(All of the ultrasonics data used in this appendix are for zero pressure and 20°C).

---

[*] Perry, F. C. "Thermoelastic Response of Polycrystalline Metals to Relativistic Electron Beam Absorption", J. Appl. Phys., Vol. 41, p. 5017-5022, 1970.

APPENDIX C

GRUNEISEN PARAMETER, PRESSURE DERIVATIVE

1. Thermodynamic Relation -

$$\gamma = \frac{\beta K^S}{\rho c_p}$$

$$\left(\frac{\partial \gamma}{\partial P} \right)_T = \gamma_0 \left[\frac{1}{\beta} \left(\frac{\partial \beta}{\partial P} \right)_T + \frac{1}{K^S} \left(\frac{\partial K^S}{\partial P} \right)_T - \frac{1}{\rho} \left(\frac{\partial \rho}{\partial P} \right)_T - \frac{1}{c_p} \left(\frac{\partial c_p}{\partial P} \right)_T \right]$$

This can be simplified by using:[*]

$$\left(\frac{\partial \beta}{\partial P} \right)_T = \left(\frac{1}{K^T} \right)^2 \left(\frac{\partial K^T}{\partial T} \right)_P$$

$$\left(\frac{\partial \rho}{\partial P} \right)_T = \frac{\rho}{K^T}$$

$$\left(\frac{\partial c_p}{\partial P} \right)_T = - \frac{T}{\rho} \left[\left(\frac{\partial \beta}{\partial T} \right)_P + \beta^2 \right]$$

---

[*] See, e.g. Thurston, R. N., "Ultrasonic Data and the Thermodynamics of Solids", _IEEE Proc._, Vol. 53, p. 1320-1336, 1965.

to give:

$$\left(\frac{\partial \gamma}{\partial P}\right)_T = \gamma_0 \left[\frac{1}{\beta K^{T^2}} \left(\frac{\partial K^T}{\partial T}\right)_P + \frac{1}{K^S} \left(\frac{\partial K^S}{\partial P}\right)_T - \frac{1}{K^T} + \right.$$

$$\left. \frac{T}{c_p \rho} \left\{ \left(\frac{\partial \beta}{\partial T}\right)_P + \beta^2 \right\} \ \times \ 23.9 \right]$$

This can be modified to:

$$\left(\frac{\partial \gamma}{\partial P}\right)_T = \frac{\gamma_0}{K^S} \left[\left(\frac{\partial K^S}{\partial P}\right)_T + \frac{1}{\beta K^T} \left(\frac{\partial K^S}{\partial T}\right)_P - 1 \right.$$

$$\left. - \gamma - T \left(\frac{\partial \gamma}{\partial T}\right)_P \right]$$

2. Constant γ/V:

$$\frac{\gamma}{V} = \frac{\gamma_0}{V_0} \quad \text{or} \quad \gamma = \rho_0 \gamma_0 V$$

$$\left(\frac{\partial \gamma}{\partial P}\right)_T = \rho_0 \gamma_0 \left(\frac{\partial V}{\partial P}\right)_T$$

but $\quad \left(\frac{\partial V}{\partial P}\right)_T = -\frac{1}{\rho^2} \left(\frac{\partial \rho}{\partial P}\right)_T = -\frac{1}{\rho K^T}$

so $\quad \left(\frac{\partial \gamma}{\partial P}\right)_T = -\frac{\rho_0 \gamma_0}{\rho K^T}$

Letting $\quad \rho = \rho_0 \left(\dfrac{K_0^T + K_{0T}^{T'} \, P}{K_0^T} \right)^{1/K_{0T}^{T'}}$

and $\quad K^T = K_0^T + K_{0T}^{T'} \, P$

gives:

$$\left(\frac{\partial \gamma}{\partial P} \right)_T = \frac{-\gamma_0}{\left(\dfrac{1}{K_0^T} \right)^{\left(1/K_{0T}^{T'} \right)} \left(K_0^T + K_{0T}^{T'} P \right)^{\left(1 + K_{0T}^{T'} \right)/K_{0T}^{T'}}}$$

At $P = 0$, this reduces to

$$\left(\frac{\partial \gamma}{\partial P} \right)_T = - \frac{\gamma_0}{K_0^T}$$

APPENDIX D

DEVIATORIC STRESS ESTIMATES

The shock wave equation of state for aluminum is given by:

$$\sigma_H = 1.0 + 140.4\ u_p + 37.7\ u_p^2$$

$$\sigma_H = 2.3 + 708\mu + 1607\mu^2 \qquad \qquad \text{(D-1)}$$

$$P_H = 708\mu + 1607\mu^2 \ \text{(Hydrostat)}$$

where $\mu = (v_o/v) - 1$.

The deviatoric stress (σ_D) can be defined as the difference between the dynamic stress-compression path ($\sigma_H - \mu$) and the hydrostat, and is a measure of the material's ability to support shear. If the material strain hardens, the deviatoric stress will be a function of μ. In Equation D-1, σ_D was assumed constant at 2.3 kbar which gives $P_H = \sigma_H - 2.3$.

The deviatoric stress can also be estimated from uniaxial stress data, shock wave data or ultrasonics data as follows:

$$\sigma_D = \sigma_H - P_H = \frac{2}{3}\ Y \qquad \qquad \text{(D-2)}$$

where Y is flow stress under uniaxial stress conditions.

A. The flow stress at low strain rate from the uniaxial stress tests (see Figure 3) is $\sim$ 3.4 kbar, which gives σ_D = 2.3 kbar.

B. For a hugoniot elastic limit (σ_e) of 5.7 kbar, the relation $Y = \sigma_e (1-2\nu/1-\nu)$ gives Y = 2.9 kbar. From Equation D-2, σ_D = 1.9 kbar.

C. Since σ_D can also be taken as the difference between σ_H and P_H at a compression corresponding to the hugoniot elastic limit, one has

$$\sigma_D = \sigma_H - P_H = \sigma_e - P_e$$

where

$$\sigma_e = \rho_0 C_L^2 \left(\frac{\mu_e}{1+\mu_e} \right) = 1096 \left(\frac{\mu_e}{1+\mu_e} \right)$$

$$P_e = \rho_0 C_B^2 \left(\frac{\mu_e}{1+\mu_e} \right) = 728 \left(\frac{\mu_e}{1+\mu_e} \right)$$

For σ_e = 5.7 kbar: μ_e = 0.0052 and P_e = 3.8 kbar. This gives σ_D = 1.9 kbar.

The agreement of these estimates with the value of 2.3 kbar from Equation D-1 is considered good, taking into account the assumptions underlying each method and the experimental inaccuracies.

Also, it should be noted that the stress-axis intercept is larger in the $\sigma_H - u$ plane than the $\sigma_H - u_p$ plane. Assuming linear elastic and hydrostatic behavior up to the elastic limit, then:

$\sigma_H - u_p$ plane -

$$\sigma_{D_u} = \rho_0 u_e (C_L - C_B)$$

$\sigma_H - \mu$ plane -

$$\sigma_{D_\mu} = \frac{\mu_e}{1+\mu_e} \left(\rho_0 C_L^2 - \rho_0 C_B^2 \right)$$

Using the approximations $u_e \simeq \mu_e/C_L$ and $\mu_e \simeq \mu_e/(1+\mu_e)$, and subtracting:

$$\Delta\sigma_D = \sigma_{D_u} - \sigma_{D_\mu} = \rho_0 C_B \mu_e (C_L - C_B)$$

For $\sigma_e = 5.7$ kbar, $\mu_e = 0.0052$ and $\Delta\sigma_D = 0.9$ kbar, compared to $\Delta\sigma_D = 1.3$ kbar from $\sigma_H - u_p$ and $\sigma_H - \mu$ given in Equation D-1.

APPENDIX E

EQUATION OF STATE, ULTRASONICS

Numerous analytical and empirical relations have been developed for determining equations of state from ultrasonics data. Some of these are presented here.

1. The Birch equation of state for the isotherm can be expressed as:[*]

$$P_T = \frac{3}{2} K_0^T \left[(1+\mu)^{7/3} - (1+\mu)^{5/3} \right] \left[1-\xi \left\{ (1+\mu)^{2/3} - 1 \right\} \right]$$

where $\xi = \dfrac{12-3\,K_{0T}^{T'}}{4}$

$$P_T = 1050 \left[(1+\mu)^{7/3} - (1+\mu)^{5/3} \right] \left[1+0.653 \left\{ (1+\mu)^{2/3} - 1 \right\} \right]$$

---

[*] Another parameter sometimes used with this equation of state is

$$\left[(1+\mu)^{2/3} - 1 \right]^2$$

where $\quad = \dfrac{3}{8} \left[K_0^T K_{0t}^{T''} - 7K_{0T}^{T'} + \left(K_{0T}^{T'} \right)^2 + \dfrac{143}{9} \right]$

However, this term can usually be neglected, contributing ~0.6% at 100 kbar for aluminum.

2. The Murnaghan equation of state is derived by assuming the bulk modulus is linear with pressure which gives:

$$\text{Isotherm} - P_T = \frac{K_0^T}{K_{0T}^{T'}} \left[(1+\mu)^{K_{0T}^{T'}} - 1 \right]$$

$$P_T = 143.7 \left[(1+\mu)^{4.87} - 1 \right]$$

$$\text{Adiabat} - P_S = \frac{K_0^S}{K_{0S}^{S'}} \left[(1+\mu)^{K_{0S}^{S'}} - 1 \right]$$

$$P_S = 158.3 \left[(1+\mu)^{4.60} - 1 \right]$$

3. Instead of a linear bulk modulus-pressure relation, Keane assumed:

$$dK^S = \left[\frac{\left(K_0^{S'} - K_\infty^{S'} \right) K_0^S}{K^S} + K_\infty^{S'} \right] dP$$

where $K_\infty^{S'}$ is the limiting value of $K^{S'}$ at very high pressure.

This leads to:

$$P_S = \frac{K_0^S K_{0S}^{S'}}{\left(K_\infty^{S'} \right)^2} \left[(1+\mu)^{K_\infty^{S'}} - 1 \right] - \frac{\left(K_{0S}^{S'} - K_\infty^{S'} \right) K_0^S}{K_\infty^{S'}} \ln (1+\mu)$$

MSL-70-23, Vol.III

Huang[*] gives the upper bound for $K^{S'}$ as:

$$K_\infty^{S'} = 4S - \frac{11}{3} = K_{0S}^{S'} - \frac{8}{3} = 1.93$$

This gives:

$$P_S = 896 \left[(1+\mu)^{1.93} - 1 \right] - 1004 \ln (1+\mu)$$

---

[*] Huang, Y. K., "Analytical Approach to the Shock Compressibility of the 18 Cubic-Lattice Metals", J. Chem. Phys., Vol. 53, p. 571-575, 1970.
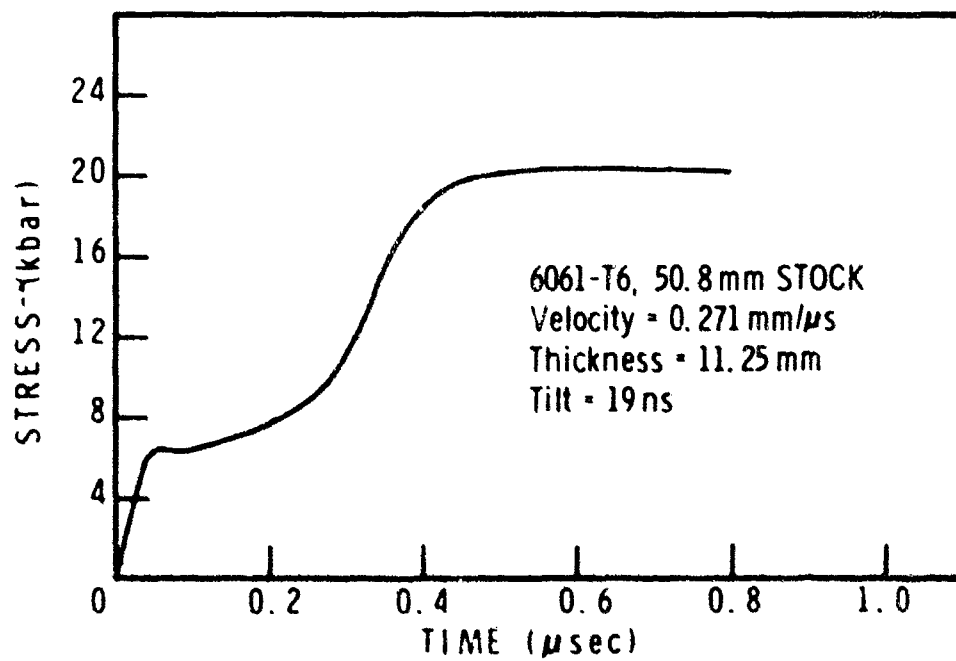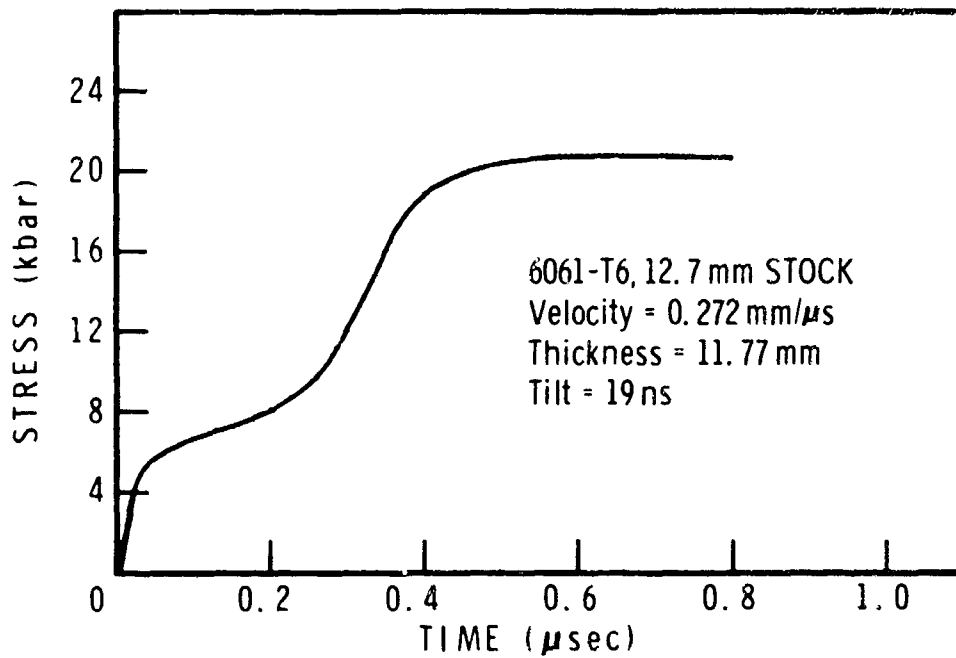
APPENDIX F

WAVE PROFILES
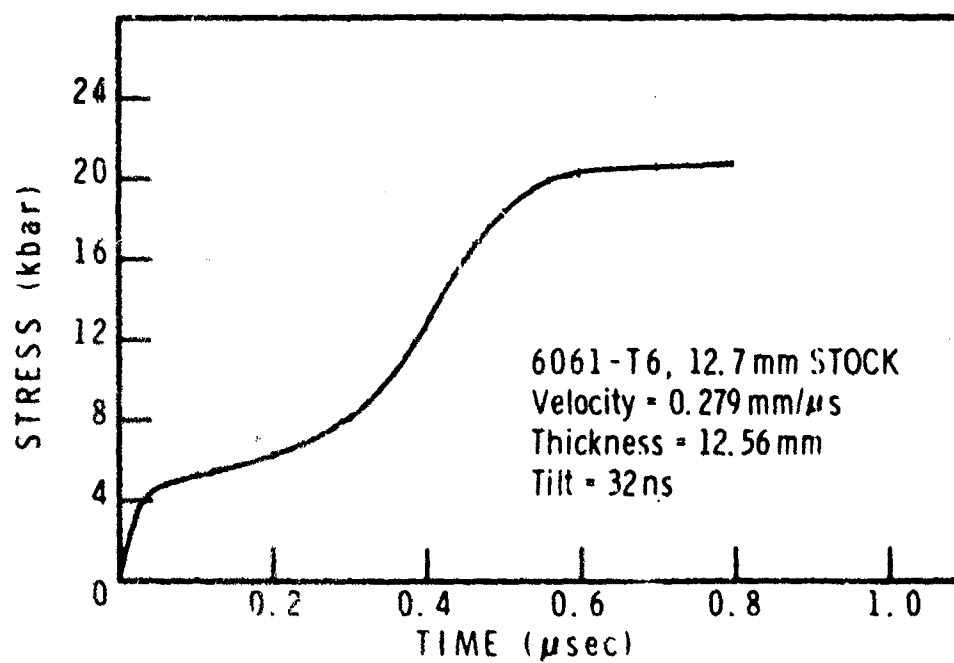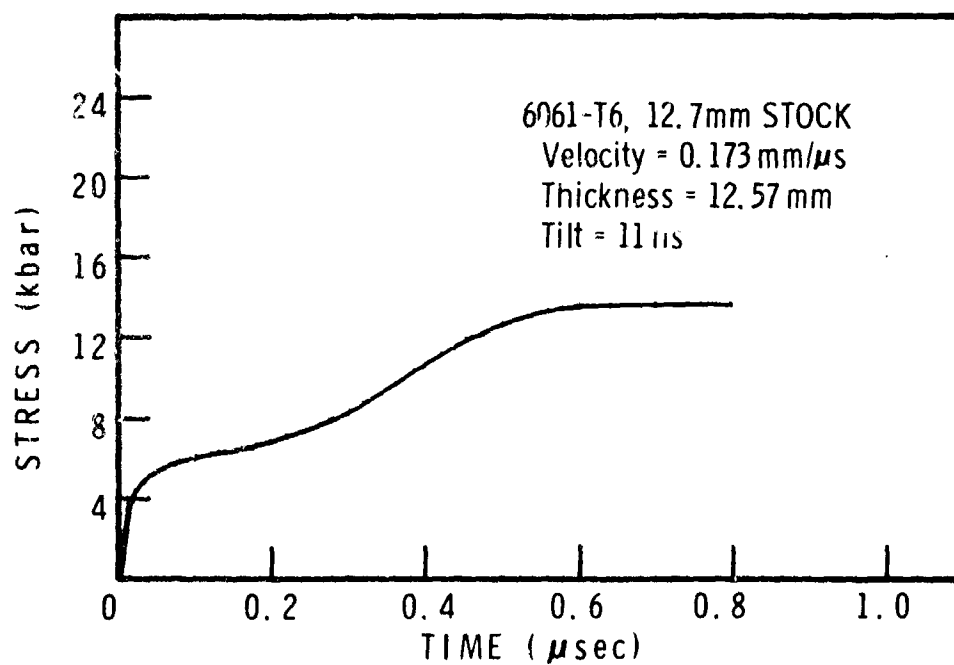

(Quartz Gage and Velocity Interferometer)

6061-T6, 6.4 mm Stock

Velocity = 0.266 mm/μsec

Thickness = 1.95 mm

Tilt = 21 ns

6061-T6, 3.2 mm Stock

Velocity = 0.284 mm/μsec

Thickness = 3.07 mm

Tilt = 18 ns

6061-T6, 6.4mm Stock

Velocity = 0.096 mm/μs

Thickness = 6.21 mm

Tilt = 28 ns

6061-T6, 50.8 mm Stock

Velocity = 0.277 mm/μs

Thickness = 6.07 mm

Tilt = 5 ns

6061-T6, 12.7 mm STOCK
Velocity = 0.272 mm/μs
Thickness = 11.77 mm
Tilt = 19 ns

6061-T6, 50.8 mm STOCK
Velocity = 0.271 mm/μs
Thickness = 11.25 mm
Tilt = 19 ns

6061-T6, 12.7mm STOCK
Velocity = 0.173 mm/μs
Thickness = 12.57 mm
Tilt = 11 ns

6061-T6, 12.7mm STOCK
Velocity = 0.279 mm/μs
Thickness = 12.56 mm
Tilt = 32 ns

6061-T6, 3.2 mm STOCK
Velocity = 0.255 mm/μs
Thickness = 3.15 mm
Tilt = 18 ns

6061-0, 3.2 mm STOCK
Velocity = 0.268 mm/μs
Thickness = 3.10 mm
Tilt = 12 ns

VI - 84

X_0 = 12.79 mm 6061-T6

X = 12.22 mm 6061-T6

V_1 = 0.268 mm/μsec

FUSED QUARTZ WINDOW

VI - 146

X_0 = 1.273 mm 6061-T6

X = 1.125 mm 6061-T6, BACKED

BY 12.71 mm FUSED QUARTZ

V_1 = 0.260 mm/μsec

FUSED QUARTZ WINDOW

VI - 183
X_0 = 12.65 mm 6061-T6
X = 20.26 mm 6061-T6
V_1 = 0.329 mm/μsec
FUSED QUARTZ WINDOW

VI - 233
X_0 = 12.75 mm 6061-T6
X = 3.780 mm 6061-T6
V_1 = 0.257 mm/μsec
X-CUT QUARTZ WINDOW

VI - 148

X_0 = 1.618 mm 6061-T6, BACKED
BY 12.7 mm OFHC COPPER

X = 3.071 mm 6061-T6

V_1 = 0.265 mm/μsec
FUSED QUARTZ WINDOW

VI - 162

X_0 = 1.626 mm 6061-T6, BACKED
BY 6.3 mm OFHC COPPER

X = 7.584 mm 6061-T6

V_1 = 0.267 mm/μsec
FUSED QUARTZ WINDOW

VI - 61

X_0 = 1.580 mm 6061-T6, BACKED BY 5.6 mm PLEXIGLAS

X = 3.106 mm 6061-T6

V_1 = 0.510 mm/sec

FUSED QUARTZ WINDOW

VI - 137

X_0 = 3.157 mm FUSED QUARTZ

X = 2.977 mm 6061-T6

V_1 = 0.489 mm/-sec

FUSED QUARTZ WINDOW

VI - 52

X_0 = 1.587 mm 6061-T6

X = 12.22 mm 6061-T6

V_I = 0.252 mm/μsec

FREE REAR SURFACE

VI - 53

X_0 = 1.440 mm 6061-T6

X = 18.19 mm 6061-T6

V_I = 0.284 mm/μsec

FREE REAR SURFACE

VI - 73

X_0 = 0.269 mm 6061-T6, BACKED
BY 6.3 mm PLEXIGLAS

X = 2.520 mm 6061-T6

V_1 = 1.242 mm/sec

FUSED QUARTZ WINDOW

VI - 74

X_0 = 0.251 mm 6061-T6, BACKED
BY 6.3 mm PLEXIGLAS

X = 5.067 mm 6061-T6

V_1 = 1.238 mm/sec

FUSED QUARTZ WINDOW

VI - 177
X_0 = 3.249 mm FUSED QUARTZ
X = 2.982 mm 6061-T6
V_1 = 0.275 mm/sec
FUSED QUARTZ WINDOW

VI - 178
X_0 = 3.058 mm FUSED QUARTZ
X = 2.97 mm 6061-T6
V_1 = 0.373 mm/sec
FUSED QUARTZ WINDOW

VI - 181
X_0 = 3.018 mm FUSED QUARTZ
X = 6.033 mm 6061-T6
V_1 = 0.361 mm/μsec
FUSED QUARTZ WINDOW

VI - 182
X_0 = 3.061 mm FUSED QUARTZ
X = 12.14 mm 6061-T6
V_1 = 0.354 mm/μsec
FUSED QUARTZ WINDOW

MSL-70-23, Vol. III

VI - 79

X_o = 0.251 mm 6061-T6, BACKED
BY 6.3 mm PLEXIGLAS

X = 1.029 mm 6061-T6

V_i = 1.235 mm/μsec

FUSED QUARTZ WINDOW

INTERFACE VELOCITY IN MM / MICROSECOND

TIME IN MICROSECONDS

VI - 83

X_o = 0.475 mm 6061-T6

X = 1.181 mm 6061-T6

V_i = 0.261 mm/μsec

FREE REAR SURFACE

FREE SURFACE VELOCITY IN MM / MICROSECOND

TIME IN MICROSECONDS

140

VI - 133

X_0 = 1.600 mm 6061-T6

X = 3.073 mm 6061-T6

V_1 = 0.265 mm/sec

FREE REAR SURFACE

VI - 135

X_0 = 1.598 mm 6061-T6

X = 1.59 mm 6061-T6, BACKED

BY 1.59 mm 6061-T6

V_1 = 0.247 mm/sec

FREE REAR SURFACE

141

MSL-70-23, Vol. III

VI - 50

$X_0 = 1.552$ mm 6061-T6

$X = 3.081$ mm 6061-T6

$V_1 = 0.222$ mm/μsec

FREE REAR SURFACE

VI - 51

$X_0 = 1.483$ mm 6061-T6

$X = 3.073$ mm 6061-T6

$V_1 = 0.155$ mm/μsec

FREE REAR SURFACE

VI - 15
X_0 = 1.879 mm 6061-T6
X = 3.124 mm 6061-T6
V_1 = 0.27 mm/μsec
FREE REAR SURFACE

VI - 63
X_0 = 1.570 mm 6061-T6
X = 3.058 mm 6061-T6
V_1 = 0.193 mm/μsec
FREE REAR SURFACE

MSL-70-23, Vol. III

VI - 104
X_o = 1.590 mm 6061-T6
X = 3.080 mm 6061 (288°C)
V_1 = 0.255 mm/sec
FREE REAR SURFACE

VI - 108
X_o = 1.562 mm 6061-T6
X = 2.776 mm 6061 (153°C)
V_1 = 0.263 mm/sec
FREE REAR SURFACE

VI - 134

X_0 = 1.575 mm 6061-T6, BACKED
BY 6.3 mm PLEXIGLAS

X = 3.081 mm 6061-T6

V_I = 0.246 mm/sec

FREE REAR SURFACE

VI - 144

X_0 = 1.603 mm 6061-T6

X = 3.028 mm 6061-T6

V_I = 0.472 mm/sec

PLEXIGLAS WINDOW

VI - 109
X_0 = 0.431 mm 6061-T6
X = 3.985 mm 6061-T6
V_I = 0.340 mm/μsec
FREE REAR SURFACE

VI - 110
X_0 = 0.419 mm 6061-T6
X = 3.970 mm 6061-T6
V_I = 0.418 mm/μsec
FREE REAR SURFACE

146

VI - 128

X_0 = 1.085 mm 6061-T6

X = 12.75 mm FUSED QUARTZ, BACKED
      BY 3.068 6061-T6

V_1 = 0.439 mm/μsec

FREE REAR SURFACE

VI - 143

X_0 = 0.904 mm 6061-T6

X = 12.74 mm FUSED QUARTZ, BACKED
      BY 3.051 mm 6061-T6

V_1 = 0.306 mm/μsec

FREE REAR SURFACE

147